Variational Hamiltonian Approach to the Quark Sector of QCD in Coulomb Gauge

Dissertation

der Mathematisch-Naturwissenschaftlichen Fakultät
der Eberhard Karls Universität Tübingen
zur Erlangung des Grades eines
Doktors der Naturwissenschaften
(Dr. rer. nat.)

vorgelegt von
Ehsan Ebadati
aus Tabriz/Iran

Tübingen
2018

Gedruckt mit Genehmigung der Mathematisch-Naturwissenschaftlichen Fakultät der Eberhard Karls Universität Tübingen.

Tag der mündlichen Qualifikation:	25.06.2018
Dekan:	Prof. Dr. Wolfgang Rosenstiel
1. Berichterstatter:	Prof. Dr. Hugo Reinhardt
2. Berichterstatter:	Prof. Dr. Dr. h.c. mult. Amand Fäßler

All the comfort and coquetries that autumn was bidding, lastly ended with the footsteps of spring.

HAFIZ

Zusamenfassung

Obwohl die Quantenchromodynamik („QCD“) als die korrekte Theorie zur Beschreibung der Wechselwirkungen zwischen Gluonen und Quarks angesehen wird, weist sie einige rätselhafte Eigenschaften auf, die untersucht werden sollten. Im Hochenergiebereich der Wechselwirkung kann zwar Störungstheorie angewandt werden, für die niedrigen Energien bedarf es aber nichtpertubativer Methoden, um Phänomene wie Farbeinschluss (Confinement) und chirale Symmetriebrechung zu erklären. Eine dieser Methoden, die auch in der vorliegenden Arbeit angewendet wird, ist der Hamilton-Variationszugang. Hierbei wird, nachdem ein Ansatz für das Vakuumwellenfunktional gemacht und die Vakuumenergie durch den Vakuumerwartungswert des Hamiltonians bestimmt wurde, die Variationsmethode angewendet, die auf die sog. Gapgleichung führt. Eine nichttriviale Lösung dieser Gleichung kann u. a. zur chiralen Symmetriebrechung führen.

In der vorliegenden Arbeit führe ich nach einem Überblick über die Yang-Mills-Theorie und die QCD den Hamiltonzugang zur QCD in Coulombeichung ein. Der Ansatz für das Vakuumwellenfunktional wird vorgestellt und die Vakuumenergie für den Quarksektor der QCD berechnet. Die Gapgleichung wird sowohl in Anwesenheit als auch in Abwesenheit der Kopplung an transversale Gluonen gelöst. Anschließend wird die Gapgleichung numerisch gelöst und das Quarkkondensat als Ordnungsparameter für die spontane Brechung der chiralen Symmetrie berechnet. Weiterhin werden die Berechnungen auf endliche Temperaturen ausgeweitet, wobei Kompaktifizierung einer Raumdimension auftritt. Die kompaktifizierte Gleichung wird in Abwesenheit der transversalen Gluonen gelöst und das Quarkkondensat bei endlichen Temperaturen bestimmt. Zum Abschluss dieser Arbeit wird die große Flexibilität des Hamilton-Variationszugangs anhand einer aktuellen Fragestellung aus der Festkörperphysik – den elektronischen Korrelationen in Graphen – demonstriert.

Abstract

Despite being considered as the correct theory for describing the interaction between gluons and quarks, Quantum Chromodynamics ("QCD") still has elusive features which should be investigated. Although the theory can be dealt with at high energy by means of perturbation theory, at low energies one needs non-perturbative methods for investigating phenomena such as confinement and chiral symmetry breaking. One possible method which has been used in this thesis is the variational Hamiltonian approach. In this method, after considering an ansatz for the vacuum wave functional and calculating the vacuum energy by taking the vacuum expectation value of the Hamiltonian, the variational method can be applied which leads to the gap equation. A non-trivial solution of this equation can be considered as a sign of chiral symmetry breaking.

In this thesis, after an overview of Yang-Mills theory and QCD, I introduce the Hamiltonian approach to the QCD in Coulomb gauge. The ansatz for the vacuum wave functional is introduced and the vacuum energy for the quark sector of QCD is calculated. Next, the gap equation for the quarks both in the absence and presence of the coupling to transverse gluons is derived. These gap equations are then solved numerically and the quark condensate as an order parameter for the spontaneous breaking of chiral symmetry is calculated. Furthermore, the calculations are extended to finite temperatures by compactification of a spatial dimension. The compactified gap equation in the absence of the transverse gluons is solved and the quark condensate at finite temperatures is calculated. Finally, the great flexibility of the variational Hamiltonian approach is demonstrated by applying it to an interesting question in solid state physics, namely the electronic correlations in graphene.

Publications Related to this Thesis

Original Articles

- Davide R. Campagnari, Ehsan Ebadati, Hugo Reinhardt and Peter Vastag
  Revised variational approach to QCD in Coulomb gauge,
  Phys. Rev. D94: 074027 (2016), arXiv: 1608.06820

- Markus Quandt, Ehsan Ebadati, Hugo Reinhardt and Peter Vastag
  Chiral symmetry restoration at finite temperature within the Hamiltonian approach to QCD in Coulomb gauge,
  Submitted to *Phys. Rev.* D (April 2018)

Conference Proceedings

- H. Reinhardt, G. Burgio, D. Campagnari, E. Ebadati, J. Heffner, M. Quandt, P. Vastag, and H. Vogt
  Hamiltonian Approach to QCD in Coulomb Gauge: A Survey of Recent Results
  Adv.High Energy Phys. 2018: 2312498 (2018), arXiv:1706.02702

- Davide Campagnari, Hugo Reinhardt, Markus Q. Huber, Peter Vastag and Ehsan Ebadati
  Dyson–Schwinger Approach to Hamiltonian QCD
  EPJ Web of Conf. 137: 03004 (2017), arXiv:1507.01414

- H. Reinhardt, G. Burgio, D. Campagnari, E. Ebadati, J. Heffner, M. Quandt, P. Vastag
  Hamiltonian approach to QCD in Coulomb gauge at zero and finite temperature
  EPJ Web of Conf. 137: 03019 (2017), arXiv:1609.09370

- H. Reinhardt, G. Burgio, D. Campagnari, M. Quandt, P. Vastag, H. Vogt, E. Ebadati
  Hamiltonian approach to QCD in Coulomb gauge: Gribov's confinement scenario at work
  EPJ Web of Conf. 164: 03004 (2017), arXiv:1607.08143

Acknowledgment

At the beginning of this thesis I want to thank Prof. Dr. Hugo Reinhardt for accepting me as his PhD student. I would like to appreciate his help, supports and guidance during my PhD in his research group. Furthermore, I would like to thank Dr. Davide Campagnari and Priv. Doz. Dr. Markus Quandt for their scientific advices and their corrections on this thesis. I would also like to thank my former PhD friends and colleagues in our research group: Dr. Hannes Vogt, Dr. Peter Vastag, Dr. Jan Heffner, Dr. Peter Watson and Priv. Doz. Dr. Giuseppe Burgio for the useful discussions and talks during my PhD studies. Furthermore, I would like to thank Dr. Julien Fraisse and Maggie Gora for their comments on the literature of this thesis. I would also like to thank Ingrid Estiry for her help and supports during my stay in Tübingen from the first day that I started my work in the research group until the last day.

I would like to thank my parents who always motivated me on the path to my goals in my life. I want to thank them for their support and love. I want also to thank my sisters and wish them all the best as always.

I want to thank all my professors, advisers, classmates, family members all who were my role models and motivated me on the path to my PhD studies. I would like to thank all the professors in the university of Tübingen, who let me work for them as their tutor. I would like to thank all the students who I tutored during the last five years. I would also like to thank the people of Tübingen, for accepting me as a foreign researcher between them and their hospitality during my stay in this beautiful city. At last, I would like to thank the people of Baden-Württemberg and Germany for motivating me to learn their language and to get familiar with their culture and history beside my studies.

Contents

Introduction

Describing nature by means of a simple model can be considered as a simplified definition for the mission which the theoretical physicists have always carried. However, it has not always been the matter of description but also in most of the cases the simplification of the phenomena, is the major goal of physics. One can mention the *theory of everything* as the ultimate goal which is the construction of a theory by unification of the *Standard Model* of particle physics and gravitation. We know that at the microscopic level all the phenomenology can be understood by means of three fundamental interactions: *strong*, *electromagnetic*, and *weak interactions* which are described by the Standard Model, while at the astrophysical scales the gravitational force is the dominant one. However, the Standard Model satisfies an intention of the theoretical physicists, which is the prediction of the phenomena earlier than the observation by the experimentalists. The most recent success of the Standard Model in describing the experimental observation and predicting them, was proved in 2012 when the Higgs boson was detected in *Large Hadron Collider* (LHC) at *CERN* [1, 2] and subsequently the Noble prize was awarded to P. Higgs and F. Englert for their prediction of this particle almost half a century earlier [3, 4]. However, this was not the first notable prediction of the Standard Model. It was in 1995 when the scientists detected the "top" quark in Fermilab, which had been predicted by M. Kobayashi and T. Maskawa in 1973 [5].

Although the Standard Model is successful in describing many phenomena in the nature and testing them by experimental approaches, it cannot provide explanation for all of them. For that matter, one can mention the discovery of the *neutrino oscillation* which shows that neutrinos have mass and led to the award of the Nobel Prize in Physics to T. Kajita and B. McDonald in 2015. However, according to the Standard Model, neutrinos were predicted to be massless [6, 7]. Furthermore, the Standard Model does not contain any viable *dark matter* particle which is believed to constitute almost 85% of the matter in the universe as a result for the need to explain the *accelerating expansion of the universe* [8, 9]. Therefore, it is clear that for the expansion of the prospective of the physicists and also satisfaction of the progress in the predictions in the theoretical physics and their matching with the experimental data, there is a demand for a more complete model *beyond* the Standard Model [10, 11].

One of the steps which led to the Standard Model occurred when M. Gell-Mann and G. Zweig proposed a model in 1972, in which they proposed that all hadrons consist of smaller particles, which were later named *quarks* [12–14]. According to the *quark model*, in which quarks were first considered in three flavors and then their number increased up to six, quarks are the building blocks of matter. Explaining the latter in the language of physics, it means that all the *hadron*s are composite of quarks or more in detail: all *baryon*s are made of three quarks and all *meson*s are made of one quark and one anti-quark. As the tradition between theoretical and experimental physics, despite being a good candidate for the explanation of the elementary particles nature, the quark model should have also passed the experimental tests. These tests were based on the assumption that if according to the theory a proton is made of three quarks, that should have the meaning that if one hits it strongly enough with another particle, the small particles should somehow get revealed. Furthermore, even if all quarks are permanently bound in

the hadrons in any kind of way, studying them as how Rutherford studied the atom by shooting some particles through them, should be somehow possible [15]. Such experiments were conducted during the 70's at CERN and SLAC[1] [16–18]. The results from these experiments, which are called *deep inelastic scattering* ("DIS"), were essentially the same as the one from Rutherford's experiment [19]. According to the deep inelastic scattering experiments, most of the particles were passing through the hadrons except some fraction which were scattered off some pointlike constituents which means that most of the positive charge of proton is concentrated in small particles. This result was a great success for both theoretical and experimental physicists which led to the start of a new era in physics.

If we try to describe mathematically all the interactions in nature except gravitation, we deal with the local relativistic quantum mechanics. Furthermore, if we treat the particles simply as point-like objects each associated with a suitable field transformation, we deal with *gauge* invariance [20]. At the classical level, gauge invariance is a property of the Maxwell equations in electrodynamics [21]. In the quantum field theory case, the basic gauge theory is quantum electrodynamics ("QED"), which is the combination of the quantum mechanics and special relativity for explaining electrically charged particles. The symmetry of the Lagrangian in QED, for which a simple example would be the emission of a photon from an electron and absorption of that by an other electron, is described by the Abelian group $U(1)$. However, the gauge theory for the Standard Model is a more complex theory based on the symmetry group $SU(3) \otimes SU(2) \otimes U(1)$. The latter, as non-Abelian gauge theory, contains 12 non-commutative generators implying that the gauge theory for the Standard Model contains the *Glashow-Salam-Weinberg* theory [22–24]. It unifies the description of electromagnetism as well as weak force into *electroweak* interaction and describes the theory of the strong interactions or *quantum chromodynamics* ("QCD").

This thesis includes works both in QED and QCD. Although the treatment of both theories is in a sense different, the theory of the QCD is based on QED. The world of QED is built up on the interaction of photons and matter, however the QCD world, as an extension of the familiar QED framework, includes the gluons mediating the strong interactions between quarks. However, regarding the interactions of the gluons with each other, even a QCD theory without fermions is a non-trivial theory. It was initially invented by C. N. Yang and R. Mills in early 60's where they extended the Abelian gauge theories to the non-Abelian groups, which formed our early understandings of the Standard Model [25].

The term QCD, the theory based on the $SU(3)$ symmetry group, is always in association with two interesting phenomena, *asymptotic freedom* and *color confinement*. The first one, predicted in 1973 by D. Gross and F. Wilczek [26] and independently by D. Politzer [27], for which the three later shared the Nobel Prize in 2004, simply implies that the coupling constant changes its behavior for large and small distances which technically defines the frontiers between the perturbative and non-perturbative approaches to QCD. In more detail, asymptotic freedom defines that at high energies or small distances, smaller than the scale of proton diameter, the coupling constant becomes small so that the interaction between quarks and gluons becomes weak. However, for the case of the low-energy regime, we face the absence of the free quarks and gluons which are *confined* in the mesons and baryons. Here, the term *confinement* means that there is no single particle carrying colored charge and all elementary particles in the nature are in the form of color singlets.

The important point here, which defines the border in the high energy physics, is that we expect at short distances to have the Coulomb potential between quarks, which can be investigated by means of perturbative methods. However, for large distances we should use

[1] Stanford Linear Accelerator Center.

non-perturbative methods such as phenomenological models. Nowadays, there are different approaches to QCD which consider the structure of the vacuum as a complex model of the quantum fields. These models are defined by means of topological entities like *center vortices*, *magnetic monopoles* or *merons* which have contributions to explanation of the confinement problem [28]. Moreover, although the *lattice* formulation, as a first principle approach in which the 3+1 dimensional space-time is discretized, has been the popular approach for the non-perturbative QCD, its famous sign problem for non-zero chemical potentials can be a good reason to use *continuum* approaches to non-perturbative QCD [29–31]. As a prime candidate, one should mention the *variational approach* [32, 33] in which the calculation and minimization of the energy in a fixed gauge is carried out for a trial vacuum wave functional. This allows to analyze the *chiral symmetry breaking* ("CSB") which is in relation with the *mass generation* for chiral quarks and matter in general. Furthermore, there is a probable relation between confinement and CSB: for example if one removes center vortices in the theory, there is no CSB and there is no confinement [34]. Thus, one can notice the importance of the CSB and mass generation and the motivation of its investigation.

One powerful non-perturbative tool in continuum QCD, both in *Coulomb gauge* [35–40] as the gauge used in this work and covariant *Landau gauge* [41–43], is *Dyson-Schwinger* equations ("DSEs") approach [44] which allows us to evaluate the *n-point* functions in QCD in a more convenient way. Technically, by means of DSEs one can calculate the propagators in the *Hamiltonian approach* for non-Gaussian functionals [45].

The Hamiltonian approach is very versatile and can be applied to a variety of physical problems. To demonstrate this I will consider the electronic correlations in graphene, a 2D monolayer of carbon atoms condensed in a honeycomb lattice. The linear dispersion in the conduction band implies an effective description as 2+1 dimensional QED but with a coupling strength 300 times larger as in QED. This means, among other things, that the electronic correlations in graphene are strong and not accessible via perturbation theory. I will use the *variational Hamiltonian approach* to study this system.

In this thesis we start with gauge theory by introducing *local gauge symmetry* as the symmetry which leads to Yang-Mills theory. We study topics as the *canonical quantization* of Yang-Mills fields and *gauge fixing*. Moreover, we review concepts like Coulomb gauge, *Gribov copies* and *Wilson loop*. After reviewing the basics of Yang-Mills theory, we add quarks to the theory leading to QCD, where we can introduce chiral symmetry breaking. After a quick review over gauge theory and QCD in chapter 2 we introduce the variational approach to QCD where motivated by a similar approach to Yang-Mills theory, we apply the same method to a theory which also includes quarks. We introduce a vacuum wave functional ansatz as trial state and we calculate the energy for a coupled quark-gluon system by taking the expectation value of the Hamiltonian of the system in the wave functional. We minimize the energy of the system in order to find the structure of the considered wave functional which leads us to gap equations whose structure includes the kernels we had as an ansatz in the wave functional. We solve the quark gap equation looking for a non-trivial solution as a sign of chiral symmetry breaking for a system of quarks in the absence of spatial gluons numerically and we calculate the *quark condensate*. Furthermore, in the second part of chapter 2, we consider a more complex ansatz for the vacuum wave functional in comparison with the former one, which includes a new coupling term and enables us to solve the quark gap equation for the coupled system of quarks and gluons. In chapter 3, we extend the study of the quark mass generation and CSB to finite temperature. The latter is introduced by means of a *dimensional compactification*, which leads to the introduction of *Matsubara frequencies* and *Poisson summation* over them. In

chapter 4 we apply our variational tools to the study of graphene in order to demonstrate the flexibility and efficiency of the method. In the appendix B, we review the numerical methods which have been used for solving the equations numerically in chapters 2, 3 and 4. We introduce the mathematical approach we used in order to solve integral equations in both two and three dimensions.

1. Quantum Chromodynamics

In this chapter we give an introduction to Quantum Chromodynamics. As the first step for the definition of the theory we start with the Yang-Mills theory, which is the gauge theory based on the symmetry group $SU(N)$. After introducing gauge fixing as the method for eliminating the unphysical degrees of freedom of the theory which leads us to work in the desired gauge (i.e. *Coulomb* gauge as the preferred gauge in this work), we describe quantization of the Yang-Mills fields. Furthermore, we discuss the behavior of the Coulomb potential in both short and long range distances as a term in the Coulomb part of the Yang-Mills Hamiltonian. Moreover, we mention the *Gribov problem* arising from fixing the gauge in our theory which leads to a different scenario for the definition of the confinement problem. Additionally, we review the *Wilson loop* as one of the *order parameter*s of confinement. At last, we talk about QCD where we have the coupling between the quarks and the gluons. Also, we look over the definition of *chirality* of the quarks and the *chiral symmetry breaking* concept and we introduce the analogy between the QCD vacuum and the BCS vacuum of superconductors. This chapter includes the standard topics in quantum field theory introducing which, we follow mainly the references [21, 46, 47].

1.1. Gauge Theory

Historically, one can say that gauge theory had a confusing past. Although it might be claimed [21] that the Yang-Mills equations were already discovered in 1938 by O. Klein [48, 49], it was later in 1954 when the Yang-Mills equations got attention [25]. The revolutionary characteristic of the Yang-Mills equations at their time, was the possibilities they made for the studies of the particles, by considering the *local symmetry* which means that Yang-Mills theory is invariant under a symmetry which changes in every space-time point, so that it is *locally* invariant. In more detail, the theory is based on fields carrying a non-Abelian charge commonly called "color" in the case of QCD. To discuss the color algebra, we recall the commutator relation between generators of a *Lie algebra*

$$[\mathfrak{t}^a, \mathfrak{t}^b] = i f^{abc} \mathfrak{t}^c \tag{1.1}$$

where f^{abc} are the *structure constant*s and $\mathfrak{t}^d$ the *generator*s of the algebra. Considering the fermion field ψ_i in any representation of $SU(N_c)$, where N_c denotes the number of the colors we deal with[1], one can define the transformation as

$$\psi_i(x) \to \Omega_{ij}(x)\psi_j(x) \tag{1.2}$$

in which Ω_{ij} is an element of $SU(N_c)$. Here we defined Ω as a function of space-time, which changes in every point in the universe which we introduce as[2]

$$\Omega_{ij}(x) = \left(e^{-i\theta^a(x)\mathfrak{t}^a}\right)_{ij} \tag{1.3}$$

[1] In the case of QCD, $N_c = 3$.

[2] We employ the sum convention, i.e. paired indices in a factor are automatically summed over.

where $\theta^a(x)$ is a locally changing variable and $\mathfrak{t}^a$ are the generators of $SU(N)$. The problem here is that the derivatives of fermion fields are not covariant under this transformation. The naive transformations of the derivatives would create a new term like $\partial\Omega$ which is unwanted. In order to cancel such a term, we define a new derivative operator which is covariant under the group transformations and that is called the *covariant derivative*

$$D_\mu \equiv \partial_\mu - igA_\mu. \tag{1.4}$$

In the above formula A_μ is the so called connection (gauge field) which in the non-compact notation has the form

$$A_\mu(x) \equiv A^a_\mu(x)\mathfrak{t}^a \tag{1.5}$$

and a is the color index of QCD. The covariant derivative of ψ field is gauge covariant

$$(D_\mu\psi)' = \Omega D_\mu\psi \tag{1.6}$$

where the gauge field $A^a_\mu(x)$ satisfies

$$A'^{\,a}_\mu(x) = A^a_\mu(x) + \delta A^a_\mu(x) \tag{1.7}$$

or explicitly

$$A'_\mu(x) = -\frac{i}{g}[\partial_\mu\Omega(x)]\Omega^{-1}(x) + \Omega(x)A_\mu(x)\Omega^{-1}(x) \tag{1.8}$$

in which, the variation for a transformation parametrized by a infinitesimal θ in equation (1.3) reads

$$\delta A^a_\mu = -\frac{1}{g}\partial_\mu\theta^a + f^{abc}\theta^b A^c_\mu. \tag{1.9}$$

The obvious point above is that if we reduce the $SU(N)$ down to $U(1)$, then we have the field transformations for QED. Furthermore, since the D_μ is covariant, its commutator relation

$$[D_\mu, D_\nu] \to \Omega[D_\mu, D_\nu]\Omega^{-1} \tag{1.10}$$

is also covariant. By introducing above transformation we have for the field strength tensor

$$\begin{aligned} F_{\mu\nu} &= \frac{i}{g}[D_\mu, D_\nu] \\ &= \partial_\mu A_\nu - \partial_\nu A_\mu - ig[A_\mu, A_\nu] \\ &= (\partial_\mu A^a_\nu - \partial_\nu A^a_\mu + gf^{abc}A^b_\mu A^c_\nu)\mathfrak{t}^a \end{aligned} \tag{1.11}$$

which means that the field strength tensor is also covariant

$$F_{\mu\nu} \to \Omega F_{\mu\nu}\Omega^{-1}. \tag{1.12}$$

Knowing that the trace of the commutator is also invariant because of the invariance of the $F_{\mu\nu}$

$$\mathrm{Tr}(\Omega F_{\mu\nu}\Omega^{-1}\Omega F^{\mu\nu}\Omega^{-1}) = \mathrm{Tr}(F_{\mu\nu}F^{\mu\nu}) \tag{1.13}$$

we can define the action of the Yang-Mills theory

$$S_{YM} = -\frac{1}{2}\int d^4x\Big(\mathrm{Tr}\, F_{\mu\nu}F^{\mu\nu}\Big) = -\frac{1}{4}\int d^4x\Big(F^a_{\mu\nu}F^{a\mu\nu}\Big) \tag{1.14}$$

which is the starting point for all the discussions in gauge field theory. Furthermore, since $\bar\psi \to \bar\psi\Omega^\dagger$ and $D_\mu\psi \to \Omega D_\mu\psi$, the coupled invariant fermion action has the form

$$S_D = \int d^4x\bar\psi(i\not{D} - m)\psi \tag{1.15}$$

where we used the Feynman slash notation

$$\not{D} = \gamma^\mu D_\mu \tag{1.16}$$

and γ^μ are the Dirac matrices. The action of QCD is the sum of the two actions above in the equations (1.14) and (1.15)

$$S_{\mathrm{QCD}} = S_{\mathrm{YM}} + S_{\mathrm{D}}. \tag{1.17}$$

1.1.1. Canonical Formulation of Yang-Mills Theory

In the gauge theory, the gauge field components play the role of the coordinates of the theory. However, in addition to the discrete Lorentz and color indices, the gauge fields also carry the continuous spatial index x. Recalling the action of the theory as

$$S_{\mathrm{YM}} = \int d^4x \; \mathcal{L}(x) \tag{1.18}$$

we first define the canonical conjugate momenta in the theory as

$$\Pi^a_\mu(x) = \frac{\partial S_{\mathrm{YM}}}{\partial \dot{A}^a_\mu(x)} \tag{1.19}$$

where $\dot{A}_\mu(x) \equiv \partial_0 A_\mu(x)$ is the time derivative of the field. Since the Lagrange density in (1.18) does not depend on $\dot{A}_0(x)$, the related canonical momentum vanishes

$$\Pi^a_0(x) = 0 \tag{1.20}$$

which would be a problem when we try to set up the canonical commutation relation with A_0 (see next section). In order to circumvent this problem we make use of the gauge invariance and choose the *Weyl* gauge

$$A^a_0(x) = 0 \tag{1.21}$$

where as the consequence, the only surviving part of the gauge field (i.e. the spatial part $A^a_i(x)$) plays the role of the coordinates of the field resulting the conjugate of the canonical momenta for the spatial gauge field to be defined as the color-electric field

$$\Pi^a_i(x) = \partial_0 A^a_i(x) = -F^a_{i0} = -E^a_i(x). \tag{1.22}$$

Furthermore, we have the agreement of the classical Hamiltonian density

$$\mathcal{H}(x) = \Pi^a_i(x)\partial_0 A^a_i(x) - \mathcal{L}(x) \tag{1.23}$$

and the classical energy density of the gauge field

$$\mathcal{H} = \frac{1}{2}(\Pi^a_i(x)\Pi^a_i(x) + B^a_i(x)B^a_i(x)) - g j^a_i(x) A^a_i(x) \tag{1.24}$$

where we have the non-Abelian magnetic field $B^a_i(x) = -\frac{1}{2}\epsilon_{ijk}F_{jk}$ and we introduced the sources $j^a_i(x)$. The equations of motion have the form

$$\dot{A}^a_i(x) = \{\mathcal{H}, A^a_i(x)\} = \Pi^a_i(x) = -E^a_i(x) \tag{1.25}$$

$$\dot{\Pi}^a_i(x) = \{\mathcal{H}, \Pi^a_i(x)\} = -\left(\hat{\mathbf{D}}^{ab} \times \mathbf{B}^b\right)_i + g j^a_i(x) \tag{1.26}$$

where the first equation reproduces the same result as (1.22) and the second equation is the non-Abelian generalization of Ampere's law, which is the spatial part of the *Euler-Lagrange* equation of the Yang-Mills fields. However, because of working in the Weyl gauge the temporal part of the field equations (Gauss' law) is missing . One can check the invariance of the equations (1.24) and (1.23) under the infinitesimal time-independent gauge transformations. This invariance can be viewed a conventional symmetry of the redefined canonical action in Weyl gauge

$$S[A] = \int d^4x \Big(\Pi_i^a(x) \partial_0 A_i^a(x) - \mathcal{H} \Big) \tag{1.27}$$

which by *Noether*'s theorem gives rise to a conserved current. Explaining the latter explicitly, if we use the infinitesimal gauge transformation in (1.3) the gauge invariance of the action (1.27) requires that the first variation with respect to the *gauge function* $\theta(x)$ to vanish which leads to the definition of the quantity

$$G^a(x) = [D_i, \Pi_i]^a \tag{1.28}$$

as the time component of a conserved Noether current for which one can define the conserved Noether charge

$$\bar{G}^a = \int d^3x G^a(x). \tag{1.29}$$

The invariance of the action (1.27) means that the considered Noether color charge density $G^a(x)$ also conserves [50]. Noether currents are conserved for the field configurations which satisfy the classical equation of motion. Since $[H, G^a] = 0$ from the Heisenberg equation of motion

$$\frac{dG^a}{dt} = i[H, G^a] \tag{1.30}$$

follows that G^a is time-independent and therefore it is constant of motion both in the classical and quantum level.

1.1.2. Canonical Quantization of Yang-Mills Theory

The canonical quantization starts in the standard manner by replacing the Poisson brackets of the canonical conjugated fields $A_i^a(x)$ and $\Pi_i^a(x)$ with the corresponding equal time commutation relations[3]

$$\begin{aligned} [A_i^a(x,t), A_j^b(y,t)] &= [\Pi_i^a(x,t), \Pi_j^b(y,t)] = 0 \\ [A_i^a(x,t), \Pi_j^b(y,t)] &= i\delta_{ij}\delta^{ab}\delta(x-y) \end{aligned} \tag{1.31}$$

where we consider the gauge fields as the coordinates of the theory. The momentum operator has the form

$$\Pi_i^a(x) = \frac{\delta}{i\delta A_i^a(x)} \tag{1.32}$$

which satisfies the above commutation relations in (1.31). Replacing the canonical momentum with its operator form in equation (1.24), we have

$$H_{\mathrm{YM}} = \frac{1}{2} \int d^3x \Big[\frac{\delta}{i\delta A_i^a(x)} \frac{\delta}{i\delta A_i^a(x)} + B_i^a(x) B_i^a(x) \Big] + \int d^3x j_i^a(x) A_i^a(x). \tag{1.33}$$

[3] In this thesis we use units in which $c = \hbar = 1$.

From left to right, first we have the kinetic term, the potential term and also the interaction with the external current j_i^a. We know that the classical electric and magnetic fields transform covariantly under the gauge transformation $A \to A^\Omega$. In quantum level, the magnetic field follows the same transformation. Moreover, one can show that the momentum operator also follows the expected transformation as below [50]

$$\Pi_i(A^\Omega) = \Omega \Pi_i(A) \Omega^{-1}. \tag{1.34}$$

Defining the infinitesimal gauge transformations (equation (1.9)), for the wave functional we have

$$\Psi(A^\Omega) = e^{-i \int d^3x \delta\theta^a(x) G^a(x)} \Psi(A) \tag{1.35}$$

where $G^a(x)$ is the Gauss law operator

$$G^a(x) = \left[D_i, \Pi_i\right] = \hat{D}_i^{ab}(x) \Pi_i^a(x). \tag{1.36}$$

What can be read from equation (1.35) is that the Gauss law is the generator of the infinitesimal time-independent gauge transformations. Now considering the same procedure for the infinite number of the infinitesimal small gauge transformations one can define the unitary Hilbert space operator

$$\mathcal{G}_0(\Theta) = e^{-i \int d^3x \Theta^a(x) G^a(x)} \tag{1.37}$$

with finite gauge function Θ generating finite gauge transformations for which in general for an arbitrary observable $O(A, \Pi)$ as a function of canonically conjugated coordinates $A_i^a(x)$ and momenta $\Pi_i^a(x)$ we have

$$O(A, \Pi) \to O(A^\Omega, \Pi^\Omega) = \mathcal{G}_0(\Theta) O(A, \Pi) \mathcal{G}_0^{-1}(\Theta). \tag{1.38}$$

Having the relations

$$\begin{aligned} \mathcal{G}_0 A_i(x) \mathcal{G}_0^{-1} &= \Omega(D_i \Omega^{-1}) = A^\Omega \\ \mathcal{G}_0 \Pi_i(x) \mathcal{G}_0^{-1} &= \Omega \Pi_i \Omega^{-1} \end{aligned} \tag{1.39}$$

and (1.38), we have

$$\Psi(A^\Omega) \equiv \Psi(\mathcal{G}_0(\Theta) A_i(x) \mathcal{G}_0(\Theta)^{-1}) = \mathcal{G}_0(\Theta) \Psi(A). \tag{1.40}$$

In order to guarantee that our quantum mechanics has a good classical limit, we require the physical states to be annihilated by the operator (1.36)

$$G^a(x) \left|\psi\right\rangle = 0. \tag{1.41}$$

This constraint is the only choice regarding the fact that the Gauss law operators are constants of motion and they do not commute with each other. In particular, it is not possible to implement Gauss' law as an operator identity [50]. Because G^a is the generator of the small gauge transformations, this constraint assures that the constrained wave functionals are invariant under small gauge transformations.

If we rewrite (1.41) as

$$\nabla \cdot \mathbf{E}^a(x) \left|\psi\right\rangle = -[A_i, E_i]^a \left|\psi\right\rangle \tag{1.42}$$

we recognize the classical Gauss law, with a non-Abelian charge density

$$\rho^a = -[A_i, E_i]^a. \tag{1.43}$$

In the case of existence of the matter fields participating in the gauge theory, the Gauss law (1.41) changes as

$$G^a(x)\,|\psi\rangle = \rho^a_{\rm M}\,|\psi\rangle \tag{1.44}$$

where by integrating the above equation one can find the gluon and matter charges

$$\begin{aligned} Q^a\,|\psi\rangle &= -\int d^3x \big(A(x)\Pi(x)\big)^a\,|\psi\rangle \\ Q^a_{\rm M}\,|\psi\rangle &= \int d^3x \rho^a_{\rm M}(x)\,|\psi\rangle \end{aligned} \tag{1.45}$$

and the total charge which should vanish

$$Q^a_{\rm tot}\,|\psi\rangle = (Q^a + Q^a_{\rm M})\,|\psi\rangle = 0. \tag{1.46}$$

Yang-Mills Equations in Schrödinger Picture

In quantum field theory the states are defined by the functionals $\Psi[A] = \langle A|\Psi\rangle$. We work in the Schrödinger picture in which the operators are time independent and the time dependence of the theory is included in the wave functional. In this picture energy eigenstates are stationary and obey the usual time-independent Schrödinger equation

$$H\,|\Psi\rangle = E\,|\Psi\rangle \tag{1.47}$$

where, as we see the gauge fields $A^a_i(x)$ have been treated as coordinates of the theory. As we already know, by imposing the Gauss law, we put a constraint on the Hilbert space of the Yang-Mills theory in order to acquire a set of gauge invariant functionals. Moreover, in the Schrödinger picture the matrix elements are given as

$$\langle\Psi|\hat{O}|\Phi\rangle = \int DA\Psi^*[A]O[\hat{A},\hat{\Pi}]\Phi[A] \tag{1.48}$$

where we integrate over all spatial components of the gauge field A.

1.1.3. Gauge Fixing

Since the wave functional is gauge invariant, the functional integral which is defined for the Yang-Mills expectation value of the observable (1.48) gets vanished if the observable would be gauge variant and it is not well defined for gauge invariant observables. Therefore, since the integration is over all the degrees of freedoms of the gauge group, it leads to the production of an infinite volume factor which means divergence. This problem can be cured by a gauge-fixing method called *Fadeev-Popov* method [51] which is based on the identity introduced as integration over all gauge transformations

$$1 = \int d\mu(\Omega)\delta(\Phi^a[A^\Omega])\mathrm{Det}G^{-1}_A. \tag{1.49}$$

Here, $d\mu(\Omega)$ is the invariant group measure or the *Haar measure* [52] and the gauge constraint is defined as

$$\Phi^a[A] = 0. \tag{1.50}$$

Moreover

$$\Big(G^{-1}_A(x,y)\Big)^{ab} = \frac{\delta\Phi^b[A^\Omega]}{\delta\Theta^a(x)} \tag{1.51}$$

is the Faddeev-Popov operator. Using the chain rule for the integral above, we can modify the form of the operator as

$$\left(G_A^{-1}(x,y)\right)^{ab} = \int d^3z \frac{\delta(A^\Omega)^c_k(z)}{\delta\Theta^a(x)} \frac{\delta\Phi[A^\Omega]}{\delta(A^\Omega)^c_k(z)} \tag{1.52}$$

where from (1.9)

$$\frac{\delta(A^\Omega)^c_k(z)}{\delta\Theta^a(x)} = \hat{D}^{ca}_k(z)\delta(z-x) \tag{1.53}$$

so that the operator (1.52) becomes

$$\left(G_A^{-1}(x,y)\right)^{ab} = \int d^3z \hat{D}^{ca}_k(z)\delta(z-x) i\Pi^c_k(z)\Phi^b[A](y). \tag{1.54}$$

Looking at the canonical momentum above, the first thing coming to the mind of the reader might be the definition of the Gauss law operator, by use of which we can rewrite the above equation as

$$\left(G_A^{-1}(x,y)\right)^{ab} = -i[G^a(x), \Phi^b(y)]. \tag{1.55}$$

In a nutshell, the Faddeev-Popov determinant is basically the Jacobian from Cartesian coordinates to curvilinear one, whose application will be seen in the next chapter. Nonetheless, by introducing a measure on the fixed gauge manifold $\mathcal{J}[A]$ as

$$\mathcal{J}[A] = \text{Det}\left(G_A^{-1}(x,y)\right)^{ab} \tag{1.56}$$

where $\left(G_A^{-1}(x,y)\right)^{ab}$ is the Faddeev-Popov matrix (1.54) in the adjoint representation of the gauge group, we can define a term in the effective action of the Yang-Mills theory as

$$\text{Det } G_A^{-1} = e^{\text{Tr}\ln G_A^{-1}} \tag{1.57}$$

for which for the gauge fixed action we have

$$S_{\text{gf}}[A] = S_{\text{YM}}[A] - \text{Tr}\ln G_A^{-1} \tag{1.58}$$

which is highly non-local. According to Feynman, the modification of the naive Yang-Mills action is necessary, because the naive quantization of the theory is not unitary [53]. Thus, the convenient way would be to represent G_A^{-1} as an functional integration over scalar fermion fields $c_a(x)$ and $\bar{c}_a(x)$ which live in the adjoint representation of the gauge group

$$\text{Det } G_A^{-1} = \int \mathcal{D}c\mathcal{D}\bar{c}\ \exp\Big\{\int d^4x d^4y \bar{c}_a(x)\Big(G_A^{-1}(x,y)\Big)_{ab} c_b(y)\Big\} \tag{1.59}$$

or the *ghosts*. The fields $c_a(x)$ restore unitarity in each order of the loop expansion.

1.1.4. Yang-Mills Theory in Coulomb Gauge

As we already know, at the classical level the existence of the Gauss law as a constraint requires the electric field to be transversal $\partial_i E_i = 0$. Moreover, at the quantum level the Gauss law eliminates the longitudinal part of the gauge potential in the wave functional which is equivalent to the Coulomb gauge $\partial_i A_i = 0$. However, in the non-Abelian theory that is not the case, although it is still the convenient gauge for the latter case. Working in the Weyl gauge, we should impose the Gauss law as a constraint on the wave functional

$$\hat{D}\Pi\Psi = \rho\Psi \tag{1.60}$$

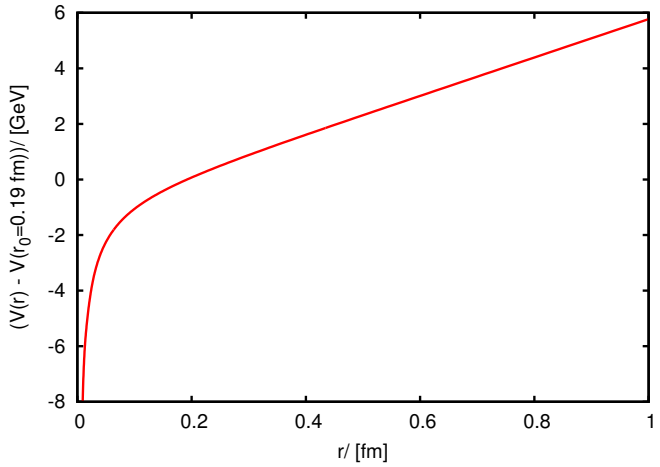

Figure 1.1.: The non-Abelian Coulomb potential showing the behavior of the formula (1.64). The linear part is the confinement region [56].

where ρ is given by (1.43). The more convenient way for the treatment of the Yang-Mills theory is to impose the Coulomb gauge, which leaves only the transversal parts of the gauge field (i.e. $A^{\perp}$), which means the transition from the Cartesian coordinates for gauge field to the curvilinear ones. However, by just imposing the Coulomb gauge to the theory we are left only with the transversal part of the gauge field in the equations except for the longitudinal part of the canonical momentum which can not simply eliminated and that is where the Gauss law helps us. By implementing Weyl and Coulomb gauges and resolving the Gauss law for getting rid of the longitudinal components of the gauge fields, we have finally the form for the Hamiltonian [54]

$$\begin{aligned} H_{YM} =& \frac{1}{2}\int d^3x (\mathcal{J}^{-1}[A^{\perp}]\Pi_i^{\perp a}(x)\mathcal{J}[A^{\perp}]\Pi_i^{\perp a}(x) + B_i^a[A^{\perp}]B_i^a[A^{\perp}]) \\ &+ \int d^3x d^3x' \mathcal{J}^{-1}[A^{\perp}]\rho_i^a(x)\,\langle x,a|(-\hat{D}\partial)^{-1}(-\partial^2)(-\hat{D}\partial)|x',b\rangle\,\mathcal{J}[A^{\perp}]\rho_i^b(x') \end{aligned} \quad (1.61)$$

where the Jacobian $\mathcal{J}[A^{\perp}]$ is given by Fadeev-Popov determinant (1.56) and we have the so called *Coulomb term*

$$F^{ab}(x,x') \equiv \langle x,a|(-\hat{D}\partial)^{-1}(-\partial^2)(-\hat{D}\partial)|b,x'\rangle \quad (1.62)$$

arising from the interaction of the fermions, whose expectation value defines the non-Abelian Coulomb potential

$$V(x-x') = g^2\,\langle F(x,x')\rangle \quad (1.63)$$

which as it has been mentioned in [55] has the form

$$V(r) \approx -\frac{g^2}{4\pi r} + \sigma_C \cdot r \quad (1.64)$$

where σ_C is the Coulomb *string tension*.

Gribov Problem and Confinement

The Gribov problem arises, because the Coulomb gauge $\partial_i A_i = 0$ does not fix uniquely the gauge and it is possible to find a A'_i, equivalent to A_i, for which $\partial_i A'_i = 0$. Because of this

problem we have infinite identical copies of the gauge fields each satisfying the Coulomb constraint which are called the *Gribov copies*. That means we can set an index for the number of the Gribov copies as

$$\partial_i A_i^{(n)} = 0 \tag{1.65}$$

where n takes infinitely many values. However, such a problem does not occur in perturbation theory. In a non-perturbative approach the functional integral (1.59) should be restricted to the first *Gribov region* [57]. This is the region in the field space where the Faddeev-Popov determinant is positive, i.e. where the gauge condition is locally invertible or unique. A globally unique gauge requires further restriction to the so-called *fundamental modular region*. This leads to the so called *Gribov-Zwanziger scenario*, where the main contributions to the functional integral come from points on the common boundary of the Gribov and fundamental modular region. As a consequence, ghosts dominate in the infrared region and the dielectric function of the Yang-Mills vacuum vanishes. The scenario also leads to Coulomb confinement, which is a necessary condition for the color confinement [58–61]

1.1.5. Wilson Loop and 't Hooft Loop

To discuss confinement, we deal with the Wilson loop as one of the order parameters which has the form [62]

$$W[A](C) = P \exp\left[i \oint dx^\mu A_\mu \right] \tag{1.66}$$

where P denotes path ordering and C represents a closed curve in space-time. The vacuum expectation value of a *temporal* Wilson loop [63] can be related to the energy $V(r)$ of an infinitely heavy static quark-antiquark pair. More precisely, for a rectangular loop C with extensions T and r in time/space direction, respectively

$$\operatorname{Tr} W(T, r) = e^{-TV(r)} \qquad T \to \infty. \tag{1.67}$$

In general the temporal Wilson loop can have either an *area law* or *perimeter law* phase

$$\langle W[A](C) \rangle \sim \begin{cases} \exp\big(-\sigma \mathcal{A}(C) \big) \ , & \text{area law} \\ \exp\big(-\kappa \mathcal{P}(C) \big) \ , & \text{perimeter law.} \end{cases} \tag{1.68}$$

The area law implies a linearly rising potential with the slope given by σ or the *Wilsonian string tension* as the sign for confinement, whereas in the deconfinement phase the expectation value decays with the perimeter of the loop $\mathcal{P}$ which leads to $V(r) = \text{const}$ as $r \to \infty$. Here, the Wilsonian string tension σ has the relation with the Coulomb string tension in equation (1.64) as

$$\sigma_C \approx (2...3) \cdot \sigma \tag{1.69}$$

where the factor 2...3 is determined in lattice simulations with quite large uncertainties [64–66].

The Wilson loop is difficult to calculate in the continuum non-Abelian approach despite the attempts which have been made [63, 67]. Therefore, this problem can be considered as a motivation for introducing another order parameter which is called the *'t Hooft* loop and it is easier to calculate in the continuum theory [68]. The operator $\hat{V}$ of the 't Hooft loop basically acts on the Wilson loop as

$$\hat{V}(C_1) W(C_2) = z^{L(C_1, C_2)} W(C_2) \hat{V}(C_1) \tag{1.70}$$

for closed loops C_1 and C_2, where L is the Gaussian linking number and z is the non-trivial center element of the gauge group. The 't Hooft loop is dual to the Wilson Loop, which means that the perimeter law for the former implies confinement and the area law implies deconfinement. Furthermore, the operator of the 't Hooft loop has the form [69]

$$\hat{V}(C) = \exp\left[i \int a(C)\Pi\right] \tag{1.71}$$

where Π is the momentum operator of the gauge field and $a(C)$ is the gauge potential of a thin center vortex which is a closed magnetic flux tube at the loop C. The effect of the 't Hooft operator on the wave functional displaces the argument of the wave functional by a center vortex field, meaning [69]

$$\hat{V}(C)\psi[A] = \psi[a(C) + A]. \tag{1.72}$$

Furthermore, in reference [70] the 't Hooft loop has been calculated with the wave functional that we later use in the variational approach and the perimeter law has been observed which is a good motivation for the ansatz of the wave functional we use and also a confirmation for the method we use.

1.2. QCD

After the investigation of the gauge fields by means of Yang-Mills theory in Coulomb gauge, we can now discuss QCD as the accepted theory for the strong interactions by including quarks in our theory for which by recalling equation (1.17) we have the Lagrangian

$$\mathcal{L}_{QCD} = -\frac{1}{4}F^{\mu\nu}F_{\mu\nu} + \sum_{f}^{6} \bar{\psi}_f(i\not{D} - m)\psi_f. \tag{1.73}$$

In the first part of the Lagrangian the Yang-Mills field, described by the *gluon*s, carries the SU(3) *color force* and the quark part expressed by the second term in the theory describing the matter fields and their interaction with the gluons. The quarks carry the index f, representing the flavor, that changes for six *flavor*s of the quarks: *up, down, strange, charm, top* and *bottom*. Moreover, quarks also carry local SU(3) color index which is suppressed here. In other words, although quarks are defined in six flavors and three colors, the index which participates in local gauge symmetry is the color index [21].

1.2.1. Chiral Symmetry

In the limit that quarks have vanishing mass QCD action acquires a symmetry which is called *chiral symmetry*. The concept of chirality for the Dirac fermions is defined by means of the Dirac matrix γ_5 which means that any Dirac field can be projected on its left- or right-handed component by the projection operators

$$P_{\pm} = \frac{1 \pm \gamma_5}{2}. \tag{1.74}$$

The QCD action for N massless flavors of the quarks is invariant under the chiral $SU_V(N) \otimes SU_A(N) \otimes U_V(1) \otimes U_A(1)$ symmetry which is, for the quarks "q", generated by

$$q \to e^{i\mathrm{t}^a\theta^a}q; \quad q \to e^{i\gamma_5\mathrm{t}^a\theta^a}q. \tag{1.75}$$

The $U_V(1) \otimes U_A(1)$ symmetry is the case when we do not have $\mathfrak{t}^a$ in the above expression [21]. Here the first $U_V(1)$ or the *vector symmetry* corresponds to the baryon number conservation and the second or the *axial symmetry* does not correspond to a conserved quantity because it is violated due to a *quantum anomaly*. Moreover, since the three quarks u, d and s have relatively small masses, the QCD action has the approximate global chiral symmetry[4]

$$m_u \sim m_d \sim m_s \sim \ 0 \to SU_V(3) \otimes SU_A(3) \otimes U_V(1) \otimes U_A(1). \tag{1.76}$$

Furthermore, the chiral symmetry is broken in nature and the π mesons, K mesons and η meson can be considered as the *Goldstone* bosons for the broken chiral symmetry. The Goldstone bosons appear in the procedure of the *spontaneous symmetry breaking* when the Lagrangian of the system is globally symmetric under some transformations, but the ground state is not invariant under the same transformations [71, 72]. The Goldstone bosons were discovered by Y. Nambu [73] in the context of the BCS superconductivity, which as we will see in next chapter, is the motivation for us to consider a BCS type vacuum wave functional for the treatment of the QCD in our method.

[4] By changing the generators of the group we have the change from the left/right chiral symmetry to axial and vector symmetry i.e. $SU_L(3), SU_R(3) \to SU_V(3), SU_A(3)$. It is the $SU_A(3)$ which is spontaneously broken in the nature.

2. Variational Approach to QCD

2.1. Overview

In this chapter we study the application of the *variational approach*, first for the Yang-Mills fields and then in QCD. Although the approach has already been applied to the Yang-Mills case [33, 40, 74], it will be discussed in this chapter regarding its application for the coupled equations in QCD, which include the gluons. Furthermore, the model in which we only consider the interaction between quarks leading to the BCS type equation is solved again in this work in order not to only review the model but also examine the computer programs and the numerical approaches. One important result of this part is a more efficient numerical treatment for the BCS type of gap equation. In the second part of this chapter, this simple model will be evaluated by a more refined variational ansatz which improves the handling of the gap equation [32].

In this chapter, we start with the *Dyson-Schwinger* equations ("DSEs") as the equations of motion for the Green functions for the quantum fields. After reviewing the DSEs we review the application of the DSEs in both Yang-Mills theory and also QCD as a tool for calculating propagators. After calculation of the energy by means of the variational approach, we solve the mass gap equation in search of non-trivial answer as the result of chiral symmetry breaking for the *leading-order* approximation. Furthermore, in the second part of this chapter we introduce a more complex ansatz for the kernel in the vacuum wave functional, expected to take care of the divergences in the gap equation, using which we find the solution for the coupled energy up to *two-loop* order. It should be mentioned here that most of the work in this chapter is based on references [40, 45, 75, 76]; the novel improved variational approach, in particular, has been published in [32].

2.2. Variational Approach to the Yang-Mills Fields

2.2.1. Variational Principle

A *variational principle* is an alternative method for determining the ground state of a physical system, by identifying it as an extremum of a function or functional. Although the *calculus of variations* as the idea for minimizing or maximizing the functionals might have a long history, the idea of its application can be in connection with the *Fermat's principle of the least time* which introduces the rays of light in the optics of 17th century: *"light travels between two given points along the path of shortest time"* [77]. However, consequently it was later *Maupertuis* who formulated the same principle for the *action* as the *least action principle* which states that whatever happens in the nature follows the least action or *"nature is thrifty in all its actions"* [78].

In quantum mechanics the variational method, which is based on the variational principle, allows us to estimate the ground state energy of the system not by solving the Schrödinger equation analytically, but by approximation. In this method, we consider a trial state as an ansatz which depends on some variational parameters and then we minimize the energy of the system with respect to the variational parameters using *Ritz's method* [79]. This gives an approximation for our trial state whose accuracy depends on

different specifications including the form of variational kernel we consider in the wave function. The variational approach to the Hamiltonian for the Yang-Mills theory in Coulomb gauge was first initiated by D. Schuette [80] who used a Gaussian trial state as an ansatz for the vacuum. However, in this work we also deal with the quarks which has been originally treated by Finger and Mandula [81] for a BCS type ansatz for the vacuum.

2.2.2. Ansatz for the Yang-Mills Vacuum

Following the same procedure in the approach used in our group, we also use the variational approach to the Yang-Mills theory in Coulomb gauge which differs from the earlier approach in [80] in terms of the ansatz for the vacuum, the treatment of the Fadeev-Popov determinant and also the renormalization of the theory [33, 55, 82]. Dealing only with the gluons in the Yang-Mills theory, we deal with the Hamiltonian (1.61), for which we consider the Gaussian ansatz as the trial state in the form[1] [33]

$$\Psi[A] = \frac{\mathcal{N}}{\sqrt{\mathcal{J}[A]}} \exp\left\{ -\frac{1}{2} \int A\omega A \right\} \tag{2.1}$$

where $\mathcal{J}$ is the Fadeev-Popov determinant (1.54) and ω is the variational kernel determined by the minimization of the Yang-Mills Hamiltonian

$$\langle \Psi | H_{\mathrm{YM}} | \Psi \rangle = \int \mathcal{D}A \mathcal{J}[A] \Psi^*[A] H_{\mathrm{YM}} \Psi[A]. \tag{2.2}$$

2.2.3. Evaluation of the Kernel and Dyson Schwinger Equations

One of the points that should be considered here, is the reason for using the DSEs for finding the propagators. As it can be seen in figure 2.1, the non-Gaussian ansatz for the vacuum state is the one which is more in agreement with the lattice calculations. Moreover, choosing a non-Gaussian ansatz for the vacuum means to deal with more parameters and in result have a better approximation in the variational approach which is what we are interested in. However, choosing a non-Gaussian ansatz for the vacuum means that not all the *n-point* functions reduce to the two-point functions (i.e. propagators) and that is where the application of the DSEs becomes important. By means of the DSEs the various n-point functions, needed in expectation values of observables like the Hamilton operator, can be expressed in terms of the variational kernels of our trial ansatz and at the end the equations of motion for these variational kernels can be derived by minimizing the energy density and solved numerically [44].

DSEs

In general Dyson-Schwinger equations, which are named after *Freeman Dyson* and *Julian Schwinger*, are functional techniques which allow us to formulate quantum field theory in a way that lets us to treat it in both perturbative and non-perturbative approaches. These equations are the equations of motion of the Green functions.

[1] We often use a shorthand notation, where integration/summation indices are suppressed and follow from the context. In the present case, for instance

$$\int A\omega A = \int d^3(x,y) A_i^a(x) \omega_{ij}^{ab}(x,y) A_j^b(y).$$

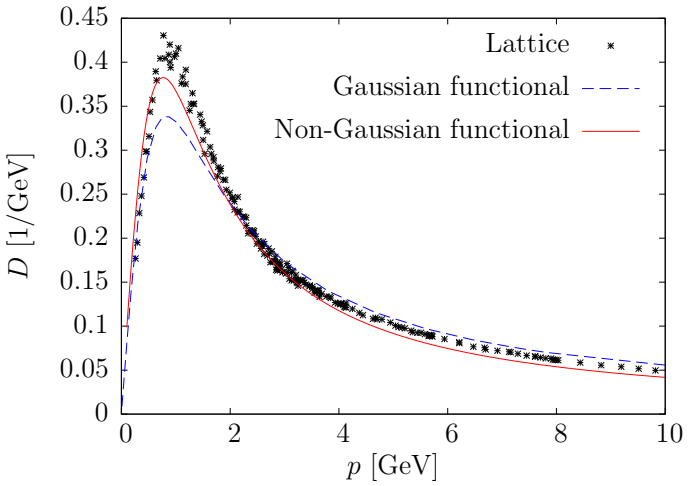

Figure 2.1.: The comparison between the results for the gluon propagator for different ansätze for the vacuum wave functional. The figure is adopted from [56].

The DSEs are based on the simple observation that the integral of a total derivative is zero. That means if consider a single scalar field ϕ, we have [21]

$$\int D\phi \frac{\delta}{\delta\phi} = 0. \tag{2.3}$$

However, considering the *generating functional* in the general form as [40]

$$Z[j] = \int D\phi \ \exp\left\{ -S(\phi) + \int j.\phi \right\} \tag{2.4}$$

and putting it in the formula (2.3), we have

$$\int D\phi \frac{\delta}{\delta\phi} \exp\left\{ -S(\phi) + \int j.\phi \right\} = 0. \tag{2.5}$$

After taking the derivative from above equation, we simply get

$$\int D\phi \{S'(\phi) + j\} \exp\left\{ S(\phi) + \int j.\phi \right\} = 0 \tag{2.6}$$

which can be written as

$$\left[S'\left(-\frac{\delta}{\delta j(x)} \right) + j(x) \right] Z[j] = 0. \tag{2.7}$$

Equation (2.7) is the general Dyson-Schwinger relation which generates the tower of DSEs.

In the next sections where we derive the DSEs in the Hamiltonian approach to the Yang-Mills theory and QCD, we follow the references [40, 45].

2.2.4. Derivation of the DSEs in the Hamiltonian Approach to the Yang-Mills Theory

Considering an arbitrary functional $K[A]$, in the Yang-Mills theory in the Coulomb gauge on the first *Gribov region* [83], we have for the expectation value

$$\langle K[A]\rangle = \int_{\mathrm{FG}} \mathcal{D}A\mathcal{J}[A]\psi^2[A]K[A] \tag{2.8}$$

where we have the Fadeev-Popov determinant (1.56) as $\mathcal{J}[A] = \mathrm{Det}(G_A^{-1})$ for which the Fadeev-Popov operator is defined as

$$\left[G_A^{-1}\right]^{ab}(r,r') = (\,-\delta^{ab}\partial_r^2 - gf^{abc}A_i^c(r)\partial_i^r)\delta(r-r'). \tag{2.9}$$

If we only consider the gauge fields in the theory, we can write the identity

$$\int_{\mathrm{FG}} \mathcal{D}A\frac{\delta}{\delta A(1)}\left\{\mathcal{J}[A]e^{-S[A]}K[A]\right\} = 0. \tag{2.10}$$

Here we used the compact notation

$$A_{l_1}^{a_1}(\boldsymbol{x}_1) = A(1), \qquad A\cdot B = A(1)B(1) = \int d^d\boldsymbol{x}A_i^a(\boldsymbol{x})\cdot B_i^a(\boldsymbol{x}) \tag{2.11}$$

where the repeated label signifies the summation over discrete Lorenz and color indices in accordance with the integration over spatial coordinates [40]. Working out the derivatives in equation (2.10), we have

$$\left\langle\left[\frac{\delta\ln\mathcal{J}[A]}{\delta A(1)} - \frac{\delta S[A]}{\delta A(1)}\right]K[A]\right\rangle + \left\langle\frac{\delta K[A]}{\delta A(1)}\right\rangle = 0. \tag{2.12}$$

The first term in the equation (2.12) can be written as

$$\frac{\delta\ln\mathcal{J}[A]}{\delta A(1)} = \frac{\delta}{\delta A(1)}\mathrm{Tr}\ln G_A^{-1} = \tilde{\Gamma}_0(1;3,2)G_A(2,3) \tag{2.13}$$

where

$$\tilde{\Gamma}_0(1;2,3) = \frac{\delta G_A^{-1}(2,3)}{\delta A(1)} \tag{2.14}$$

is the bare ghost-gluon vertex. The equation (2.12) can be written as

$$\left\langle\frac{\delta S[A]}{\delta A(1)}K[A]\right\rangle = \left\langle\frac{\delta K[A]}{\delta A(1)}\right\rangle + \tilde{\Gamma}_0(1;3,2)\left\langle G_A(2,3)K[A]\right\rangle \tag{2.15}$$

which is the DSE for the Yang-Mills sector, where the bare vertex $\tilde{\Gamma}_0$ is the lowest-order perturbative contribution to the full ghost-gluon vertex $\tilde{\Gamma}$, defined as [84]

$$\langle A(1)G_A(2,3)\rangle = \langle A(1)c(2)\bar{c}(3)\rangle = -D(1,1')G(2,2')\tilde{\Gamma}(1';2',3')G(3',3) \tag{2.16}$$

where

$$D(1,1') = \langle A(1)A(1')\rangle \tag{2.17}$$

is the gluon propagator and

$$G(2,2') = \langle G_A(2,2')\rangle = \langle c(2)\bar{c}(2')\rangle \tag{2.18}$$

is the ghost propagator[2].

The most remarkable feature for the lattice data for the gluon propagator (see figure 2.1) in the equation (2.17) is that it can be nicely fitted by the Gribov formula [57]

$$\omega(p) = \sqrt{p^2 + M_G^4/p^2} \tag{2.19}$$

with the Gribov mass $M_G \simeq 880$ MeV$\simeq 2\sqrt{\sigma}$ where σ is the Wilsonian string tension [85].

The ghost propagator in equation (2.18), by translational invariance of the Yang-Mills vacuum, in momentum space has the form

$$G(\boldsymbol{p}) = \frac{d(\boldsymbol{p})}{\boldsymbol{p}^2} \tag{2.20}$$

where we introduce the *ghost form factor* $d(\boldsymbol{p})$. One can identify the inverse of the ghost form factor as the dielectric function of the Yang-Mills vacuum [58]

$$\epsilon(\boldsymbol{p}) = 1/d(\boldsymbol{p}). \tag{2.21}$$

Generally, the ghost form factor in QCD is infrared divergent

$$d^{-1}(\boldsymbol{p} = 0) = 0 \tag{2.22}$$

as the so called *horizon condition* which is required for confinement in the Gribov-Zwanziger confinement scenario[3]. By this condition the dielectric function of the Yang-Mills vacuum vanishes for the infrared region and and hence the Yang-Mills vacuum is a perfect color dielectric medium [86, 87].

2.3. Variational Approach to QCD

2.3.1. Ansatz for the Vacuum State

Considering the Yang-Mills vacuum as a color dielectric, we have an analogy between superconductors and the color dielectric model of the QCD vacuum. A type-II superconductor exhibits a diamagnetic body to which the magnetic field can not penetrate except in thin flux tubes (i.e. *Abrikosov vortices*) [88]. However, the vacuum of the QCD also can be considered as color dielectric which suppresses the color electric fields to narrow strings. This argument motivates us for considering the vacuum of the QCD almost the same as the vacuum in the BCS theory

$$|\Phi_{\mathrm{BCS}}\rangle = e^{\sum_{m,n} C_{mn} a_m^\dagger b_n^\dagger} |0\rangle \tag{2.23}$$

where we have the creation operators of the electrons and holes which below the critical temperature form the famous *Cooper pairs* [89]. Furthermore, C_{mn} is the amplitude in which the variational kernels denoting the occupation probabilities for the different single-particle states are included [90]. At last, variation of the expectation value of the BCS Hamiltonian with respect to the kernels leads us to the gap equation, which is a equation for the energy gap for the lowest excited states. In QCD we have the dual of this situation, i.e. the magnetic flux tubes get substituted with the string between quark anti-quark pairs.

[2] We do not introduce ghost fields explicitly as dynamical fields and only use them to make the meaning of the various variational kernels clearer.

[3] This condition follows automatically in D=2+1, while it has to be imposed as a boundary condition in D=3+1 in order to select the correct physical solution of the variational equations.

Furthermore, by considering the transversal gluons in the theory, the vacuum of the QCD can be constructed by the unification of the Yang-Mills and the fermionic vacuum

$$|\Phi_{\mathrm{QCD}}\rangle \to |\Phi_{\mathrm{YM}}\rangle \otimes |\Phi_{\mathrm{Q}}\rangle \tag{2.24}$$

where the gluonic part (i.e. Φ_{YM}) is given by (2.1) and the quark part has the form

$$|\Phi_{\mathrm{Q}}\rangle = \exp\left(- \int d^3(1,2,1',2')\psi^\dagger(1)\Lambda_+(1,1')K(1',2')\Lambda_-(2',2)\psi(2)\right)|0\rangle \tag{2.25}$$

where ψ represents the Dirac field and $\Lambda_\pm$ are the projectors onto negative and positive particles energy.

By the motivation arising form the analogy between the QCD vacuum model and the BCS theory, the first attempts for solving the model for the uncoupled quarks were started in references [81, 91]. However, one can mention the work done by Adler and Davis [92] which led to the consideration of a kernel only for the quarks that are not coupled to the transverse gluons as the vacuum ansatz. As we see in the next sections, the gap equation derived by Adler and Davis (*Adler-Davis equation*) plays a very important role in the understanding of the chiral symmetry breaking in terms of the physical behavior of its numerical solution for the mass function. It is also the basis for the later calculations at finite temperature.

Calculation of the Expectation Values

As we know for the calculation of the energy we need to calculate the expectation value of the Hamiltonian which means the effect of the operators on the vacuum states depending on the sector we consider (either bosonic or fermionic). For that reason, we need to represent the wave functionals in coordinate form for which in the first step we have the definition for the gluon sector as

$$\langle A|\hat{A}(1)|\Psi\rangle = A(1)\Psi[A], \qquad \langle A|\hat{\Pi}(1)|\Psi\rangle = \frac{\delta\Psi[A]}{i\delta A(1)} \tag{2.26}$$

where $\Psi[A] \equiv \langle A|\Psi\rangle$. Furthermore, for the fermionic part, considering the fermionic coherent states explained in appendix C, we have

$$\begin{aligned}\langle\xi|\hat{\psi}(1)|\Phi\rangle &= \left(\xi_-(1) + \frac{\delta}{\delta\xi_+^\dagger(1)}\right)\Phi(\xi_+^\dagger,\xi_-)\\ \langle\xi|\hat{\psi}^\dagger(1)|\Phi\rangle &= \left(\xi_+^\dagger(1) + \frac{\delta}{\delta\xi_-(1)}\right)\Phi(\xi_+^\dagger,\xi_-)\end{aligned} \tag{2.27}$$

where $\xi_\pm = \Lambda_\pm\xi$ are the energy-projected *Grassmann variables*. Considering the fermionic sector of the theory, we know that for the calculation of the expectation value we have the definition of an general operator $\mathcal{O}$ sandwiched between two Fock states $|\Phi\rangle$ as

$$\langle\Phi|\mathcal{O}[\hat{\psi},\hat{\psi}^\dagger]|\Phi\rangle = \int \mathcal{D}\xi^\dagger\mathcal{D}\xi e^{-\mu}\Phi^*\mathcal{O}\left[\xi_- + \frac{\delta}{\delta\xi_+^\dagger}, \xi_+^\dagger + \frac{\delta}{\delta\xi_-}\right]\Phi \tag{2.28}$$

where we have

$$\mu = \xi^\dagger(1)[\Lambda_+(1,2) - \Lambda_-(1,2)]\xi(2) \equiv 2\xi^\dagger(1)S_0(1,2)\xi(2) \tag{2.29}$$

and where S_0 which in the momentum space reads

$$S_0(\boldsymbol{p}) = \frac{\boldsymbol{\alpha}\cdot\boldsymbol{p} + \beta m}{2E(\boldsymbol{p})} \tag{2.30}$$

is the bare fermion propagator. Preparing the basics of the theory, the vacuum state of the QCD can be written as

$$\Phi[A, \xi_+^\dagger, \xi_-] =: \exp\left\{ -\frac{1}{2}S_A[A] - S_f[\xi_+^\dagger, \xi_-, A]\right\} \tag{2.31}$$

where S_f is the fermionic part of the vacuum and S_A is the pure Yang-Mills part. However, although S_f represents the fermionic vacuum functional of the theory, it also contains the quark-gluon interaction. Furthermore, one can write the perturbative gluonic action in equation (2.31) as [40]

$$S_A[A] = \int \bar{d}^3p A_i^a(\boldsymbol{p})|\boldsymbol{p}|A_i^a(-\boldsymbol{p}), \qquad \bar{d}^3p = d^3p/(2\pi)^3. \tag{2.32}$$

The expectation values in the interacting theory in QCD in Coulomb gauge according to equations (2.26), (2.27) and (2.28) have the form

$$\left\langle \mathcal{O}[\hat{\psi}, \hat{\psi}^\dagger, A, \Pi]\right\rangle = \int \mathcal{D}\xi^\dagger\mathcal{D}\xi\mathcal{D}A\mathcal{J}_A e^{-\mu}e^{-\frac{1}{2}S_A - S_f^*}\mathcal{O}\left[\xi_- + \frac{\delta}{\delta\xi_+^\dagger}, \xi_+^\dagger + \frac{\delta}{\delta\xi_-}, A, -i\frac{\delta}{\delta A}\right]e^{-\frac{1}{2}S_A - S_f}. \tag{2.33}$$

Introducing the integral measure

$$\eta = -\mu - S_A - S_f^* - S_f \tag{2.34}$$

and after the evaluation of the derivatives, the vacuum expectation value (2.33) can be written in a shorter form as

$$\langle f[A, \xi, \xi^\dagger]\rangle = \int \mathcal{D}\xi^\dagger\mathcal{D}\xi\mathcal{D}A\ \mathcal{J}_A\ e^\eta f[A, \xi, \xi^\dagger] \tag{2.35}$$

where f is some functional of $\xi^\dagger, \xi, A$.

2.3.2. Kernel Structure for the Coupled Quarks

To be more precise about the fermionic vacuum state, we start with the form below as for the fermionic action

$$S_f = \xi^\dagger(1)\Lambda_+(1,1')K_A(1',2')\Lambda_-(2',2)\xi(2) \tag{2.36}$$

where K_A contains the interaction of the quarks with the transversal gluons in our case

$$K_A(1,2) = K_0(1,2) + K_1(1,2;3)A(3) \tag{2.37}$$

in which K_0 and K_1 are the variational kernels. The ansatz above can be considered as the leading order expansion of K_A in powers of the gauge field. Furthermore, this ansatz represents the quark wave functional in the form of the *Slater determinant* [93] and guarantees the validity of *Wick's theorem* [94] in the theory [45]. Writing explicitly the Hermitian conjugate of the fermionic part of the action in equation (2.33) we have

$$S_f + S_f^* + \mu = \xi^\dagger(1)\left[2S_0(1,2) + \bar{\gamma}(1,2) + \bar{\Gamma}_0(1,2;3)A(3)\right]\xi(2) \tag{2.38}$$

where

$$\bar{\gamma}(1,2) = \Lambda_+(1,1')K_0(1',2')\Lambda_-(2',2) + \Lambda_-(1,1')K_0^\dagger(1',2')\Lambda_+(2',2) \tag{2.39}$$

is the *biquark* kernel and

$$\bar{\Gamma}_0(1,2;3) = \Lambda_+(1,1')K_1(1',2';3)\Lambda_-(2',2) + \Lambda_-(1,1')K_1^\dagger(1',2';3)\Lambda_+(2',2). \tag{2.40}$$

the bare quark-gluon vertex. Furthermore, the biquark kernel must have non-trivial Dirac structures in order to avoid the bare vacuum $S_f = 0$ rising from the orthogonality of the projectors $\Lambda_\pm$. Moreover, the color index also appears here in the kernel part

$$K_0^{mn} = \beta\delta^{mn}s(\boldsymbol{p}) \tag{2.41}$$

and

$$K_i^{mn,a} = g\mathfrak{t}_a^{mn}\alpha_i V(\boldsymbol{p},\boldsymbol{q}) \tag{2.42}$$

where $V(\boldsymbol{p},\boldsymbol{q})$ and $s(\boldsymbol{p})$ are the so called vector part[4] and scalar part of the variational kernel. Furthermore, the α and β are the Dirac matrices and $\mathfrak{t}_a^{mn}$ is the color generator. Here, for the momentum we have the conservation relation meaning $\boldsymbol{p}+\boldsymbol{q}+\boldsymbol{k} = 0$. Moreover, the kernels $V(\boldsymbol{p},\boldsymbol{q})$ and $s(\boldsymbol{p})$ have been considered real and symmetric meaning

$$s(\boldsymbol{p}) = s(-\boldsymbol{p}) = s^*(\boldsymbol{p}) \tag{2.43}$$

and

$$V(\boldsymbol{p},\boldsymbol{q}) = V(-\boldsymbol{q},-\boldsymbol{p}) = V^*(\boldsymbol{q},\boldsymbol{p}). \tag{2.44}$$

Working in the chiral limit ($m = 0$) and considering the kernels as real and symmetric functions, for the vertex, we have the form

$$\bar{\Gamma}_{0,i}^{mn,a}(\boldsymbol{p},\boldsymbol{q};\boldsymbol{k}) = 2g\mathfrak{t}_a^{mn}V(\boldsymbol{p},\boldsymbol{q})M_i(\boldsymbol{p},\boldsymbol{q}) \tag{2.45}$$

where

$$M_i(\boldsymbol{p},\boldsymbol{q}) \equiv \frac{1}{4}(1+\boldsymbol{\alpha}\cdot\hat{\boldsymbol{p}})\alpha_i(1+\boldsymbol{\alpha}\cdot\hat{\boldsymbol{q}}) \tag{2.46}$$

which satisfies the relations

$$\begin{aligned}\boldsymbol{\alpha}\cdot\hat{\boldsymbol{p}}M_i(\boldsymbol{p},\boldsymbol{q}) =& M_i(\boldsymbol{p},\boldsymbol{q}) = M_i(\boldsymbol{p},\boldsymbol{q})\boldsymbol{\alpha}\cdot\hat{\boldsymbol{q}}\\ M_i(\boldsymbol{p},\boldsymbol{q})\beta =& -\beta M_i(-\boldsymbol{p},-\boldsymbol{q})\end{aligned} \tag{2.47}$$

and equation (2.39) casts to

$$\bar{\gamma}(\boldsymbol{p}) = \beta s(\boldsymbol{p}). \tag{2.48}$$

Considering the Yang-Mills sector, we use a Gaussian functional

$$S_A = \omega(1,2)A(1)A(2) \tag{2.49}$$

for which, it could have been also considered a non-Gaussian functional[5].

[4] Here one should pay attention that the vector characteristics of this part is hidden in the vector α_i and the vector part $V(\boldsymbol{p},\boldsymbol{q})$ is a scalar function.

[5] For further reading the interested reader is referred to the reference [40].

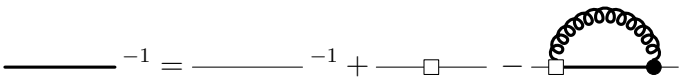

Figure 2.2.: Diagrammatic representation of the equation (2.57). The straight and wavy lines represent the quark and gluon propagators, respectively. The thin and thick lines are for the bare and full propagators, while the empty boxes show the variational kernels and the full dots are for the one particle irreducible vertices. The diagrams in this section are adopted and reprinted with permission from [45].

Quark Propagator DSE

With the explicit form of the fermionic vacuum defined in the formula (2.38) we have the DSEs for the QCD case as

$$[2S_0(1,2) + \bar{\gamma}(1,2)]\,\langle \xi(2) f\rangle + \bar{\Gamma}_0(1,2;3)\,\langle \xi(2) A(3) f\rangle = \left\langle \frac{\delta f}{\delta \xi^\dagger(1)} \right\rangle \tag{2.50}$$

$$[2S_0(2,1) + \bar{\gamma}(2,1)]\,\langle \xi(2) f\rangle + \bar{\Gamma}_0(2,1;3)\,\langle \xi(2) A(3) f\rangle = \left\langle \frac{\delta f}{\delta \xi(1)} \right\rangle \tag{2.51}$$

$$2\omega(1,2)\,\langle A(2) f\rangle + \bar{\Gamma}_0(3,2;1)\,\langle \xi(2)\xi^\dagger(3) f\rangle - \tilde{\Gamma}_0(1;3,2)\,\langle G_A(2,3) f\rangle = \left\langle \frac{\delta f}{\delta A(1)} \right\rangle \tag{2.52}$$

where the choice for the functional f can include any form letting us to express the different n-point functions of the fields in QCD. Putting $f = \xi^\dagger$ in the DSE (2.50), we have

$$\big[2S_0(1,3) + \bar{\gamma}(1,3)\big]\langle \xi(3)\xi^\dagger(2)\rangle + \bar{\Gamma}_0(1,3;4)]\langle \xi(3)\xi^\dagger(2) A(4)\rangle = \delta(1,2). \tag{2.53}$$

For rewriting the above formula in terms of the propagators we define

$$\langle \xi(1)\xi^\dagger(2)\rangle = Q(1,2) \tag{2.54}$$

where $Q(1,2)$ is not the true quark propagator but rather the so-called *Grassmann propagator* [75] using which we can write the full quark-gluon vertex $\bar{\Gamma}$ as

$$\langle A(4)\xi(3)\xi^\dagger(2)\rangle =: -\bar{\Gamma}(3',2';4') D(4,4') Q(3,3') Q(2,2'). \tag{2.55}$$

However, for the real quark propagator we have

$$S(1,2) = \big[\langle \xi(1)\xi^\dagger(2)\rangle + \Lambda_-(1,2)\big] - \frac{1}{2}\delta(1,2) = Q(1,2) - S_0(1,2). \tag{2.56}$$

Using the above expressions we have

$$Q^{-1}(1,2) = 2S_0(1,2) + \bar{\gamma}(1,2) - \bar{\Gamma}(1,3;4) D(4,4') Q(3,3') \bar{\Gamma}(3',2;4') \tag{2.57}$$

which in momentum space after inserting equation (2.48) for $\bar{\gamma}$ reads

$$\begin{aligned} Q^{-1}(\boldsymbol{p}) &= \delta^{mn}[\boldsymbol{\alpha}\cdot\hat{\boldsymbol{p}} + \beta s(\boldsymbol{p})] \\ &\quad - \int \bar{d}^3 q \Gamma^{mk,a}_{0,i}(\boldsymbol{p},\boldsymbol{q};-\boldsymbol{q}-\boldsymbol{p}) Q(-\boldsymbol{q}) D_{ij}(\boldsymbol{p}+\boldsymbol{q}) \bar{\Gamma}^{kn,a}_{j}(-\boldsymbol{q},-\boldsymbol{p};\boldsymbol{p}+\boldsymbol{q}). \end{aligned} \tag{2.58}$$

Equation (2.58) is represented diagrammatically in figure 2.2. Furthermore, what is also possible here is to use equation (2.51) for the calculation of the quark propagator, in which one should put $f = \xi$ instead of $f = \xi^\dagger$.

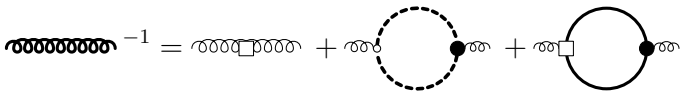

Figure 2.3.: Diagrammatic representation of the equation (2.65). The empty boxes represent the variational kernels, dashed lines represent the propagators and the dots represent the bare ghost-gluon vertex.

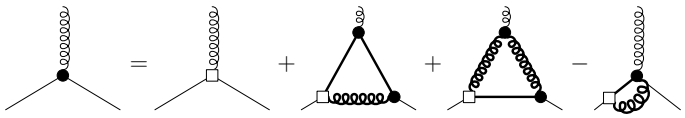

Figure 2.4.: Diagrammatic representation for the equation (2.67).

Gluon Propagator DSE

Recalling the gluon propagator (2.17), we have

$$\langle A(1)A(2)\rangle =: D(1,2) \equiv [2\Omega(1,2)]^{-1} \tag{2.59}$$

where in momentum space, $\Omega(\boldsymbol{p})$ is the gluon dispersion relation, i.e. Ω represents the energy of a single gluon state with momentum $\boldsymbol{p}$. We will call Ω simply the "gluon energy". The DSE for the gluon propagator can be obtained by putting $f = A$ in the equation (2.52) leading to

$$2\omega(1,3)D(3,2) - \bar{\Gamma}_0(4,3;1)\,\langle \xi(3)\xi^\dagger(4)A(2)\rangle - \tilde{\Gamma}_0(1;4,3)\,\langle G_A(3,4)A(2)\rangle = t(1,2). \tag{2.60}$$

Moreover, $t(1,2)$ in equation (2.60) is the transversal projector

$$t_{ij}(\boldsymbol{x}) = \int \bar{d}^3 p e^{i\boldsymbol{p}\cdot\boldsymbol{x}} t_{ij}(\boldsymbol{p}) \tag{2.61}$$

which in the momentum space has the form

$$t_{ij}(\boldsymbol{p}) = \delta_{ij} - \hat{p}_i\hat{p}_j. \tag{2.62}$$

To introduce loop contributions, we follow the references [40] and [33] and define

$$\chi(1,2) = \frac{1}{2}\tilde{\Gamma}_0(1;3,4)G(3',3)G(4,4')\tilde{\Gamma}(2;4',3') \tag{2.63}$$

where the full and bare ghost-gluon vertices are given by equations (2.14) and (2.16). Moreover, the quark loop has the form

$$\sigma(1,2) = \frac{1}{2}\bar{\Gamma}_0(3,4;1)Q(3',3)Q(4,4')\bar{\Gamma}(4',3';2). \tag{2.64}$$

Considering the definitions above, the DSE (2.60) for the gluon propagator can be written as

$$\Omega(1,2) = \omega(1,2) + \chi(1,2) + \sigma(1,2) \tag{2.65}$$

where, ω is the kernel for the Yang-Mills part of the theory (see equation (2.32)). Equation (2.65) is shown diagrammatically in figure 2.3.

Figure 2.5.: Diagrammatic representation of the DSE (2.69) for the ghost propagator.

Quark-Gluon Vertex DSE

For the calculation of the quark-gluon vertex DSE, we put $f = \xi^\dagger A$ in the equation (2.50) and by knowing that $\langle A \rangle = 0$ we have

$$[Q_0(1,4) + \bar{\gamma}(1,4)] \langle \xi(4)\xi^\dagger(2)A(3)\rangle + \bar{\Gamma}_0(1,4;5) \langle \xi(4)A(5)\xi^\dagger(2)A(3)\rangle = 0. \tag{2.66}$$

As the consequence, the DSE result for the quark-gluon vertex has the form as

$$\begin{aligned}\bar{\Gamma}(1,2;3) = \bar{\Gamma}_0(1,2;3) &+ \bar{\Gamma}_0(1,4;6')Q(4,4')\bar{\Gamma}(4',5;3)Q(5,5')\bar{\Gamma}(5',2;6)D(6,6') \\ &+ \bar{\Gamma}_0(1,4;6')D(4,4')\Gamma(4',5,3)D(5,5')\bar{\Gamma}(6,2;5')Q(6,6') \\ &- \bar{\Gamma}_0(1,5;4)D(4,4')Q(5,5')\bar{\Gamma}(5',2;4',3)\end{aligned} \tag{2.67}$$

which as it can be observed in the last diagram of figure 2.4 leads to two gluon-two quark vertices. Moreover, there is also another possible equation for the quark-gluon vertex which can be obtained by putting $f = AA$ in the equation (2.52) which would have as a new element a two ghost-two gluon vertex which is, however, equivalent to the equation above [75].

Ghost DSE

In order to calculate the ghost DSE, we call the Fadeev-Popov operator in the form [45, 75]

$$G_A(1,2) = G_0(1,2) - G_0(1,4)A(3)\tilde{\Gamma}_0(4,5;3)G_A(5,2). \tag{2.68}$$

Taking the expectation value of above equation and using the definition of the ghost-gluon vertex (2.16) we have for the ghost DSE

$$G^{-1}(1,2) = G_0^{-1}(1,2) - \tilde{\Gamma}_0(1,4;3)D(3,3')G(4,4')\tilde{\Gamma}(4',2;3') \tag{2.69}$$

which diagrammatically shown in the figure 2.5.

2.3.3. Bare Vertex Approximation

In the equations which we have for the quark propagator in the last subsection, for the sake of simplicity, one can replace the full vertex with the bare vertex, although we know that this would not give a realistic answer for the chiral symmetry breaking. The bare vertex approximation means that in the non-perturbative approach we just consider the leading-order loop contribution (*tree level*) in the vertex part of our calculations [95]. Furthermore, we know that for the calculation of the kernel arising from the bare vertex, we need to calculate the energy. To express the energy, it is useful to define the inverse of the quark propagator in terms of Dirac matrices

$$Q^{-1}(\boldsymbol{p}) = A(\boldsymbol{p})\boldsymbol{\alpha}\cdot\hat{\boldsymbol{p}} + \beta B(\boldsymbol{p}) - i\beta\boldsymbol{\alpha}\cdot\hat{\boldsymbol{p}}C(\boldsymbol{p}) + D(\boldsymbol{p}) \tag{2.70}$$

which is the inverted form of

$$Q(\boldsymbol{p}) = \frac{A(\boldsymbol{p})\boldsymbol{\alpha}\cdot\hat{\boldsymbol{p}} + \beta B(\boldsymbol{p}) - i\beta\boldsymbol{\alpha}\cdot\hat{\boldsymbol{p}}C(\boldsymbol{p}) - D(\boldsymbol{p})}{\Delta(\boldsymbol{p})} \tag{2.71}$$

where

$$\Delta(\boldsymbol{p}) = A^2(\boldsymbol{p}) + B^2(\boldsymbol{p}) + C^2(\boldsymbol{p}) - D^2(\boldsymbol{p}). \tag{2.72}$$

Although the Dirac structure considered above has four coefficients called the *dressing functions* [96], which are basically the corrections to the form factors in Dirac structure considered here [97], by indication from the lattice and perturbation theory we can consider just the α and β parts. So that, by putting $C = D = 0$ and using equation (2.58), we have

$$A(\boldsymbol{p}) = 1 + \frac{g^2 C_F}{2}\int đ^3q \frac{X(\boldsymbol{p},\boldsymbol{q})A(\boldsymbol{q})V^2(\boldsymbol{p},\boldsymbol{q})}{\Omega(\boldsymbol{p}+\boldsymbol{q})\Delta(\boldsymbol{q})} \tag{2.73}$$

$$B(\boldsymbol{p}) = s(\boldsymbol{p}) + \frac{g^2 C_F}{2}\int đ^3q \frac{X(\boldsymbol{p},\boldsymbol{q})B(\boldsymbol{q})V^2(\boldsymbol{p},\boldsymbol{q})}{\Omega(\boldsymbol{p}+\boldsymbol{q})\Delta(\boldsymbol{q})} \tag{2.74}$$

where

$$X(\boldsymbol{p},\boldsymbol{q}) = 1 - \frac{[\hat{\boldsymbol{p}}\cdot(\boldsymbol{p}+\boldsymbol{q})][\hat{\boldsymbol{q}}\cdot(\boldsymbol{p}+\boldsymbol{q})]}{(\boldsymbol{p}+\boldsymbol{q})^2}. \tag{2.75}$$

Furthermore, C_F is the quadratic Casimir coefficient in the fundamental representation

$$C_F = \frac{N_c^2 - 1}{2N_c} \tag{2.76}$$

where N_c is the number of colors [98].

The importance of the DSEs is that they allow us to use the non-Gaussian functionals. However, in case of the Gaussian functionals the DSEs become trivial and using them would not be anymore necessary [58]. The DSEs allow us to express the propagators in terms of the variational kernels which build the vacuum state structure. The Dyson-Schwinger approach is a straightforward approach for the calculation of the propagators and that is why it has been used in this thesis. However, as we see in section 2.6, it is also possible to use methods other than DSEs for calculating the propagators. Furthermore, as we see in the next section, the DSEs allow us to express the expectation value of the QCD Hamiltonian in terms of the variational kernels and enable us to use the variational principle for the non-Gaussian wave functionals, which are required for the fields with interaction.

2.4. QCD Full Hamiltonian

The Hamiltonian operator of QCD in Coulomb gauge is given by adding the quarks to the equation (1.61) [54]

$$\begin{aligned} H_{QCD} = &-\frac{1}{2}\int d^3x \mathcal{J}_A^{-1}\frac{\delta}{\delta A_i^a(\boldsymbol{x})}\mathcal{J}_A\frac{\delta}{\delta A_i^a(\boldsymbol{x})} + \frac{1}{4}\int d^3x F_{ij}^a(\boldsymbol{x})F_{ij}^a(\boldsymbol{x}) \\ &+ \int d^3x \psi^{m\dagger}(\boldsymbol{x})[-i\alpha_i(\partial_i) + \beta m]\psi^m(\boldsymbol{x}) - g\int d^3x \psi^{m\dagger}(\boldsymbol{x})\alpha_i A_i^a \mathfrak{t}_a^{mn}\psi^n(\boldsymbol{x}) \\ &+ \frac{g^2}{2}\int d^3(x,y)\mathcal{J}_A^{-1}\rho^a(\boldsymbol{x})\mathcal{J}_A F^{ab}(\boldsymbol{x},\boldsymbol{y})\rho^b(\boldsymbol{y}) \end{aligned} \tag{2.77}$$

where $\mathcal{J}_A$, F^{ab} and F^a_{ij} are given by the equations (1.56), (1.62) and (1.11). Moreover, the color charges in the Coulomb interaction part of the Hamiltonian are defined as

$$\rho^a(\boldsymbol{x}) = \rho^a_A(\boldsymbol{x}) + \rho^a_q(\boldsymbol{x}) = f^{abc}A^b_i(\boldsymbol{x})\frac{\delta}{i\delta A^c_i(\boldsymbol{x})} + \psi^{m\dagger}(\boldsymbol{x})\mathfrak{t}^{mn}_a\psi^n(\boldsymbol{x}) \tag{2.78}$$

which can be written in our digit notation as

$$\rho^a(1) = \rho^a_A(1) + \rho^a_q(1) := R(1;2,3)A(2)\frac{\delta}{\delta A^a_i(3)} + \bar{R}(1;2,3)\psi^\dagger(2)\psi(3) \tag{2.79}$$

where we have the kernels [75]

$$\begin{aligned}\bar{R}(1;2,3) &= \mathfrak{t}^{m_2m_3}_{a_1}\delta_{\alpha_2\alpha_3}\delta(\boldsymbol{x}_1-\boldsymbol{x}_2)\delta(\boldsymbol{x}_1-\boldsymbol{x}_3)\\ R(1;2,3) &= f^{a_1a_2a_3}\delta_{i_2i_3}\delta(\boldsymbol{x}_1-\boldsymbol{x}_2)\delta(\boldsymbol{x}_1-\boldsymbol{x}_3).\end{aligned} \tag{2.80}$$

Basically we can write the QCD Hamiltonian (2.77) in the form

$$H_{QCD} = H_E + H_B + H^{AA}_C + H^{qA}_C + H^{qq}_C + H_D \tag{2.81}$$

where for the kinetic (*chromoelectric*) part we have

$$H_E = -\frac{1}{2}\mathcal{J}_A^{-1}\frac{\delta}{\delta A(1)}\mathcal{J}_A\frac{\delta}{\delta A(1)} \tag{2.82}$$

and the magnetic term of the Yang-Mills theory has the form

$$H_B = -\frac{1}{2}A(1)\Delta(1,2)A(2) + \frac{1}{3!}T_3(1,2,3)A(1)A(2)A(3) + \frac{1}{4!}T_4(1,2,3,4)A(1)A(2)A(3)A(4) \tag{2.83}$$

where the tensor structures $\Delta(1,2)$, T_3 and T_4 can be found in reference [40].

The Coulomb part of the Hamiltonian is defined for the interactions between gluons and quarks. For the first part in the Coulomb part for the gluon interactions as the pure Yang-Mills part we have

$$H^{AA}_C = \frac{g^2}{2}\mathcal{J}_A^{-1}\rho_A(1)\mathcal{J}_A F(1,2)\rho_A(2), \tag{2.84}$$

for the fermion-gluon interaction part

$$H^{qA}_C = \frac{g^2}{2}[\mathcal{J}_A^{-1}\rho_A(1)\mathcal{J}_A F(1,2)\rho_q(2) + \rho_q(1)F(1,2)\rho_A(2)], \tag{2.85}$$

and for the fermionic Coulomb interaction we have

$$H^{qq}_C = \frac{g^2}{2}\rho_q(1)F(1,2)\rho_q(2) \tag{2.86}$$

where F is given by (1.62). For the quark section of QCD, it is a viable approximation to only consider the direct Coulomb interaction of quarks from equation (2.86).

As the last term in the Hamiltonian, the Dirac part (single particle quark part) has the form

$$H_D = \psi^\dagger(1)[h_D(1,2) - J(1,2;3)A(3)]\psi(2) \tag{2.87}$$

where h_D represents the single particle quark Hamiltonian

$$h_D(\boldsymbol{p}) = \boldsymbol{\alpha}\cdot\boldsymbol{p} + \beta m \tag{2.88}$$

and

$$J(1,2;3) = g\mathfrak{t}^{m_1m_2}_{\alpha_3}(\alpha_{i3})_{\alpha_1\alpha_2}\delta(\boldsymbol{x}_1-\boldsymbol{x}_2)\delta(\boldsymbol{x}_2-\boldsymbol{x}_3). \tag{2.89}$$

2.4.1. Calculation of the Energy

In this part we calculate the energy terms by taking the expectation value of the Hamiltonian for each part in equation (2.81). The results are the terms that depend on the kernel defined in our vacuum ansatz which we later variate in order to determine the variational kernel.

Single-Particle Term

We start with the single-particle part of the Hamiltonian which after taking the expectation value yields [45]

$$\begin{aligned}\langle H_D\rangle = h_D(1,2)[\langle\xi^\dagger(1)\xi(2)\rangle + \Lambda_+(2,1)] \\ - J(1,2;3)[\langle\xi^\dagger(1)\xi(2)A(3)\rangle + \Lambda_+(2,1)\,\langle A(3)\rangle].\end{aligned} \tag{2.90}$$

Knowing that $\langle A\rangle = 0$ and using the definition of the equation (2.55) the above equation takes the form

$$\langle H_D\rangle = h_D(1,2)[\Lambda_+(2,1) - Q(2,1)] - J(1,2;3)D(3,3')Q(2,2')Q(1',1)\bar{\Gamma}(2',1';3'). \tag{2.91}$$

Writing the above equation in momentum space we have

$$E_D = -\int đ^3q\ \mathrm{Tr}[\boldsymbol{\alpha}.\boldsymbol{q}Q(\boldsymbol{q})] - g\int đ^3(q,l)D_{ij}(\boldsymbol{q}+\boldsymbol{l})\mathfrak{t}_a^{mn}\mathrm{Tr}[\alpha_i Q(\boldsymbol{q})\Gamma_j^{nm,a}(\boldsymbol{q},\boldsymbol{l};-\boldsymbol{q}-\boldsymbol{l})Q(-\boldsymbol{l})] \tag{2.92}$$

which after replacing the full quark-gluon vertex $\bar{\Gamma}$ by the bare vertex $\bar{\Gamma}_0$ and working out the traces can be cast into the form

$$\begin{aligned}E_D = &-4N_c\int đ^3q\frac{|\boldsymbol{q}|A(\boldsymbol{q})}{\Delta(\boldsymbol{q})} + 2g^2N_cC_F\int đ^3(q,l)\frac{X(\boldsymbol{q},\boldsymbol{l})}{\Delta(\boldsymbol{q})\Delta(\boldsymbol{l})\Omega(\boldsymbol{q}+\boldsymbol{l})} \\ &\times V(\boldsymbol{q},\boldsymbol{l})[A(\boldsymbol{q})A(\boldsymbol{l}) + B(\boldsymbol{q})B(\boldsymbol{l})]\end{aligned} \tag{2.93}$$

as the single particle energy part.

Fermion-Fermion Coulomb Interaction

Following the calculation of the single particle energy, we have the quark Coulomb part of the Hamiltonian whose expectation value leads us to the quark Coulomb energy. In our calculation, the Coulomb energy of two interacting quarks has the form

$$\langle H_C^{qq}\rangle = \frac{g^2}{2}\bar{R}(1;3,4)\bar{R}(2;5,6)\,\langle\psi^\dagger(3)\psi(4)F(1,2)\psi^\dagger(5)\psi(6)\rangle \tag{2.94}$$

where g is the coupling constant and $F(1,2)$ represents the Coulomb kernel which, as it has already been explained in chapter 1, arises from the application of the Gauss law in Coulomb gauge. Considering the expectation value of four fermion operators, equation (2.94) has the form [45]

$$\begin{aligned}\langle H_C^{qq}\rangle = \frac{g^2}{2}\bar{R}(1;3,4)\bar{R}(2;5,6)\Big[&\langle\xi^\dagger(3)\xi(4)F(1,2)\xi^\dagger(5)\xi(6)\rangle \\ &+\langle\xi^\dagger(3)\xi(4)F(1,2)\rangle\,\Lambda_+(6,5) + \langle\xi(4)\xi^\dagger(5)F(1,2)\rangle\,\Lambda_+(6,3) \\ &+\langle\xi^\dagger(5)\xi(6)F(1,2)\rangle\,\Lambda_+(4,3) + \langle\xi^\dagger(3)\xi(6)F(1,2)\rangle\,\Lambda_-(4,5) \\ &+[\Lambda_+(4,3)\Lambda_+(6,5) + \Lambda_+(6,3)\Lambda_-(4,5)]\,\langle F(1,2)\rangle\Big].\end{aligned} \tag{2.95}$$

Here, we should pay attention that up to two loops in the energy it is sufficient to replace the Coulomb kernel with its vacuum expectation value [75]. One should also pay attention that up to one loop arising from the variation of the $\langle H_C^{qq}\rangle$, we can ignore the variation of the Coulomb kernel with respect to the gluon propagator which leads us to drop out the last term in (2.95). Furthermore, since the projectors $\Lambda_\pm$ are unit matrices in the color space their contraction with $\bar{R}$ (2.80) leads to the trace of the gauge group generators resulting the 2nd and 4th terms of equation (2.95) to vanish

$$\langle H_C^{qq}\rangle \simeq \frac{g^2}{2}\bar{R}(1;3,4)\bar{R}(2;5,6)F(1,2)\Big[\,\langle\xi(4)\xi^\dagger(3)\xi(6)\xi^\dagger(5)\rangle + Q(4,5)\Lambda_+(6,3) - Q(6,3)\Lambda_-(4,5)\Big]. \tag{2.96}$$

Writing the four-point expectation value up to the leading order contribution, we have

$$\langle\xi(4)\xi^\dagger(3)\xi(6)\xi^\dagger(5)\rangle = Q(4,3)Q(6,5) - Q(4,5)Q(6,3). \tag{2.97}$$

Since the quark propagator $Q(1,2)$ is color diagonal, the contribution of the first term in the right-hand side of equation (2.97) vanishes when we insert that in equation (2.96) because of the trace over color indices. The Coulomb term then reads

$$\langle H_C^{qq}\rangle \simeq \frac{g^2}{2}\bar{R}(1;3,4)\bar{R}(2;5,6)F(1,2)Q(4,5)[Q_0(6,3) - Q(6,3)]. \tag{2.98}$$

After Fourier transformation and considering the symmetric properties of the Coulomb kernel $F(1,2) = F(2,1)$ symmetrizing the above formula, we have

$$E_C = -\frac{g^2}{2}\int đ^3(q,l)F(\boldsymbol{q}-\boldsymbol{l})\,\mathrm{Tr}\Big\{\big[Q(\boldsymbol{l}) - S_0(\boldsymbol{l})\big]\big[Q(\boldsymbol{q}) - S_0(\boldsymbol{q})\big]\Big\}. \tag{2.99}$$

By inserting the explicit form of $Q(\boldsymbol{p})$ from equation (2.71) and working out the traces we have the Coulomb energy term as

$$E_C = -\frac{g^2 C_F}{2}\int đ^3(q,l)\frac{F(\boldsymbol{q}-\boldsymbol{l})}{\Delta(\boldsymbol{q})\Delta(\boldsymbol{l})}\big[4B(\boldsymbol{q})B(\boldsymbol{l}) - \hat{\boldsymbol{q}}\cdot\hat{\boldsymbol{l}}\big(2A(\boldsymbol{q}) - \Delta(\boldsymbol{q})\big)\big(2A(\boldsymbol{l}) - \Delta(\boldsymbol{l})\big)\big]. \tag{2.100}$$

Yang-Mills Chromoelectric Term

The chromoelectric term of the Hamiltonian has the form

$$\langle H_E\rangle = \frac{1}{2}\int \mathcal{D}A\mathcal{D}\xi^\dagger\mathcal{D}\xi e^{-\mu}\Big\{\frac{\delta}{\delta A(1)}e^{-S_f^* - \frac{S_A}{2}}\Big\}\mathcal{J}_A\frac{\delta}{\delta A(1)}e^{-S_f - \frac{S_A}{2}} \tag{2.101}$$

which becomes

$$\langle H_E\rangle = \frac{1}{8}\left\langle\frac{\delta S_A}{\delta A(1)}\frac{\delta S_A}{\delta A(1)}\right\rangle + \frac{1}{4}\left\langle\frac{\delta S_A}{\delta A(1)}\frac{\delta(S_f + S_f^*)}{\delta A(1)}\right\rangle + \frac{1}{2}\left\langle\frac{\delta S_f^*}{\delta A(1)}\frac{\delta S_f}{\delta A(1)}\right\rangle. \tag{2.102}$$

Using the DSE (2.52), this can be written as [45]

$$\langle H_E\rangle = \frac{1}{8}\left[\left\langle\frac{\delta^2 S_A}{\delta A(1)\delta A(1)}\right\rangle - \left\langle\frac{\delta(S_f - S_f^*)}{\delta A(1)}\frac{\delta(S_f - S_f^*)}{\delta A(1)}\right\rangle + \tilde{\Gamma}_0(3,2;1)\left\langle G_A(2,3)\frac{\delta S_A}{\delta A(1)}\right\rangle\right]. \tag{2.103}$$

For a Gaussian trial wave functional we have

$$\langle H_E\rangle = \frac{1}{4}[\Omega(1,2) - \chi(1,2)]\Omega^{-1}(2,3)[\Omega(3,1) - \chi(3,1)] - \frac{1}{4}[\sigma(1,1) + \Sigma(1,1)] \tag{2.104}$$

where $\Sigma(1,1)$ has the same definition as σ (2.64) but with both vertices replaced by

$$\bar{\Gamma}_-(1,2,3) = \Lambda_+(1,1')K_1(1',2';3)\Lambda_-(2',2) - \Lambda_-(1,1')K_1^\dagger(1',2;3)\Lambda_+(2',2). \tag{2.105}$$

Writing the energy density $E_E = \frac{H_E}{N_C V}$ in momentum space we have

$$E_E = C_F \int đ^3q \frac{[\Omega(\boldsymbol{q}) - \chi(\boldsymbol{q})]^2}{\Omega(\boldsymbol{q})} - g^2 C_F \int đ^3(q,l) V^2(\boldsymbol{q},\boldsymbol{l}) t_{ij}(\boldsymbol{q}+\boldsymbol{l}) \\ \times \mathrm{Tr}[\Lambda_+(\boldsymbol{q})Q(\boldsymbol{q})\Lambda_+(\boldsymbol{q})\alpha_i\Lambda_-(-\boldsymbol{l})Q(-\boldsymbol{l})\Lambda_-(-\boldsymbol{l})\alpha_j] \tag{2.106}$$

which after taking the traces leads to

$$E_E = C_F \int đ^3q \frac{[\Omega(\boldsymbol{q}) - \chi(\boldsymbol{q})]^2}{\Omega(\boldsymbol{q})} - g^2 C_F \int đ^3(q,l) \frac{X(\boldsymbol{q},\boldsymbol{l})}{\Delta(\boldsymbol{q})\Delta(\boldsymbol{l})} V^2(\boldsymbol{q},\boldsymbol{l}) A(\boldsymbol{q}) A(\boldsymbol{l}) \equiv \quad E_E^{YM} + E_E^Q. \tag{2.107}$$

2.5. Determination of the Variational Kernels

After the calculation of the energy terms by taking the expectation value of the Hamiltonian, we are now at the stage in which we can determine the variational kernels. For this purpose we use the Ritz's variational method, meaning that we minimize the energy with respect to the various kernels K

$$\frac{\partial \langle H_{\mathrm{QCD}} \rangle}{\partial K} \stackrel{!}{=} 0. \tag{2.108}$$

Rewriting the calculated energy terms[6], we have

$$E_D = -4 \int đ^3q \frac{|\boldsymbol{q}| A_q}{\Delta_q} + 2g^2 C_F \int đ^3(q,l) \frac{X(\boldsymbol{q},\boldsymbol{l})V(\boldsymbol{q},\boldsymbol{l})}{\Omega(\boldsymbol{q}+\boldsymbol{l})} \frac{A_q A_l + B_q B_l}{\Delta_q \Delta_l}$$

$$E_E = g^2 C_F \int đ^3(q,l) \frac{X(\boldsymbol{q},\boldsymbol{l})V^2(\boldsymbol{q},\boldsymbol{l})}{\Delta_q \Delta_l} A_q A_l$$

$$E_C = -g^2 \frac{C_F}{2} \int đ^3(q,l) F(\boldsymbol{q}-\boldsymbol{l}) \frac{4B_q B_l + \hat{\boldsymbol{q}}\cdot\hat{\boldsymbol{l}}[A_q(2-A_q) - B_q^2][A_l(2-A_l) - B_l^2]}{\Delta_q \Delta_l}. \tag{2.109}$$

As we see in the equations in (2.74), the energy integrals contain the scalar kernel s only implicitly through the dressing functions A and B and the vector kernel V both implicitly and explicitly. Furthermore, by using the gluon DSE, the energy density can be written as a function of the inverse gluon propagator Ω [40]. It is then convenient to choose B and V (instead of s and V) as the variational kernels, so that s and A depend on B and V. Explicitly, the relevant variations have the form[7]

$$\frac{\delta A_k}{\delta V(\boldsymbol{p},\boldsymbol{q})} = g^2 \frac{C_F}{2} \frac{X(\boldsymbol{p},\boldsymbol{q})V(\boldsymbol{p},\boldsymbol{q})}{\Omega(\boldsymbol{p}+\boldsymbol{q})} \left[đ(\boldsymbol{k}-\boldsymbol{p}) \frac{A_q}{\Delta_q} + đ(\boldsymbol{k}-\boldsymbol{q}) \frac{A_p}{\Delta_p} \right] \\ + g^2 \frac{C_F}{2} \int đ^3l \frac{X(\boldsymbol{k},\boldsymbol{l})V(\boldsymbol{k},\boldsymbol{l})^2}{\Omega(\boldsymbol{k}+\boldsymbol{l})} \frac{B_l^2 - A_l^2}{\Delta_l^2} \frac{\delta A_{\boldsymbol{l}}}{\delta V(\boldsymbol{p},\boldsymbol{q})} \tag{2.110}$$

[6] Here, in order to simplify the notation, we express the momentum dependence of the dressing function as a subscript (i.e. $A(\boldsymbol{p}) \equiv A_p$).

[7] One should pay attention that for a symmetric vector kernel the variation of $V(a,b)$ with respect to $V(c,d)$ has the form

$$\frac{\delta V(a,b)}{\delta V(c,d)} = \frac{1}{2}\big(\delta(a-c)\delta(b-d) + \delta(a-d)\delta(b-c)\big).$$

and

$$\frac{\delta A_k}{\delta B_p} = -g^2 C_F \frac{X(\boldsymbol{p},\boldsymbol{q})V^2(\boldsymbol{p},\boldsymbol{q})}{\Omega(\boldsymbol{p}+\boldsymbol{q})}\frac{A_p B_p}{\Delta_p^2} + \int \bar{d}^3 l \frac{X(\boldsymbol{k},\boldsymbol{l})V^2(\boldsymbol{k},\boldsymbol{l})}{\Omega(\boldsymbol{k}+\boldsymbol{l})}\frac{B_l^2 - A_l^2}{\Delta_l^2}\frac{\delta A_l}{\delta B_p}. \tag{2.111}$$

Vector Kernel

Differentiating the energy terms in (2.109) with respect to the vector kernel V means taking the vector kernel from the diagrams out. However, for the two-loop contributions to the energy, it is enough to consider the explicit dependence on V while for the one-loop term (the first part in equation (2.93)) we must include the implicit dependence on V through the dressing functions A and B [45].

The variation with respect to V leads to

$$V(\boldsymbol{p},\boldsymbol{q}) = -\frac{A_p A_q + B_p B_q}{A_p A_q \Omega(\boldsymbol{p}+\boldsymbol{q}) + |\boldsymbol{p}| A_q \frac{A_p^2 - B_p^2}{\Delta_p} + |\boldsymbol{q}| A_p \frac{A_q^2 - B_q^2}{\Delta_q}}. \tag{2.112}$$

Introducing

$$b_p \equiv \frac{B_p}{A_p} \tag{2.113}$$

we can rewrite equation (2.112) as

$$V(\boldsymbol{p},\boldsymbol{q}) = -\frac{(1 + b_p b_q)}{\Omega(\boldsymbol{p}+\boldsymbol{q}) + \frac{|\boldsymbol{p}|}{A_p}\frac{1-b_p^2}{1+b_p^2} + \frac{|\boldsymbol{q}|}{A_q}\frac{1-b_q^2}{1+b_q^2}} \tag{2.114}$$

which is in accordance with the perturbative result at large momenta [45].

2.5.1. Gluon Gap Equation

To derive the gluon gap equation we should perform the variation of the energy terms with respect to Ω or, in a more convenient way, with respect to Ω^{-1}. For this, we need the variation of the dressing function A (2.73), which has the form

$$\frac{\delta A_q}{\delta \Omega_p^{-1}} = g^2 \frac{C_F}{2}\frac{X(\boldsymbol{q},\boldsymbol{p}-\boldsymbol{q})}{\Delta_{p-q}} A_{p-q} V^2(\boldsymbol{q},\boldsymbol{p}-\boldsymbol{q}). \tag{2.115}$$

Variating the energy, we have

$$\Omega^2(\boldsymbol{p}) = \boldsymbol{p}^2 + \text{Yang-Mills terms} - 2g^2 \int \bar{d}^3 q \frac{X(\boldsymbol{q},\boldsymbol{p}-\boldsymbol{q})V^2(\boldsymbol{q},\boldsymbol{p}-\boldsymbol{q})}{A_q A_{p-q}(1+b_q^2)(1+b_{p-q}^2)}\Big(\Omega(\boldsymbol{p}) + \frac{|\boldsymbol{q}|}{A_q}\frac{1-b_q^2}{1+b_q^2}\Big) \tag{2.116}$$

where we have omitted to write the explicit form of the Yang-Mills terms due to their irrelevance to this work. The integral in equation (2.116) shows the quark-loop contribution, which should be distinguished from the quark loop which occurs in equation (2.65). The integral in equation (2.116) is UV divergent. Introducing a sharp UV cutoff Λ, the divergent terms are [40]

$$\frac{g^2}{(4\pi)^2}\left[-\frac{8}{3}\Lambda^2 + \frac{2}{3}(\boldsymbol{p}^2 + \Omega^2(\boldsymbol{p}))\ln\Lambda^2\right]. \tag{2.117}$$

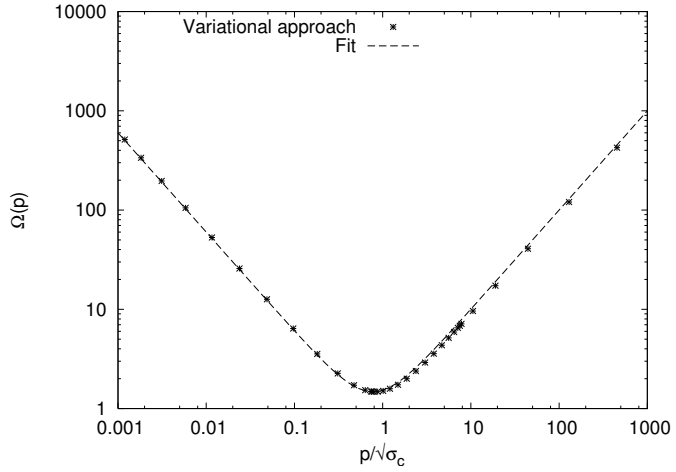

Figure 2.6.: The result obtained as the solution for the gluon energy $\Omega(\boldsymbol{p})$ in [40].

Here, the quadratic divergence is the effect of the cutoff regularization in Hamiltonian approach, while the logarithmic divergence leads, after renormalization, to the correct coefficient β_0 of the QCD β-*function* [75]. The solution for the equation (2.116) obtained in [40] is shown in figure 2.6.

2.5.2. Quark Gap Equation

Variation of the energy terms in (2.109) with respect to B leads us to the quark gap equation

$$\begin{aligned}|\boldsymbol{p}|b_p =& \frac{g^2 C_F}{2}\int \bar{d}^3 q F(\boldsymbol{p}-\boldsymbol{q})\frac{b_q(1-b_p^2)-\hat{\boldsymbol{p}}\cdot\hat{\boldsymbol{q}}\,b_p[2-A_q(1+b_q^2)]}{A_q(1+b_q^2)}\\ &+\frac{g^2 C_F}{2}\int \bar{d}^3 q \frac{X(\boldsymbol{p},\boldsymbol{q})}{\Omega(\boldsymbol{p}+\boldsymbol{q})}\frac{V^2(\boldsymbol{p},\boldsymbol{q})}{A_q(1+b_q^2)(1+b_p b_q)}\\ &\left\{(b_q-b_p)\left[2\frac{|\boldsymbol{p}|}{A_p}\frac{1-b_p^2}{1+b_p^2}+\frac{|\boldsymbol{q}|}{A_q}\frac{1-b_q^2}{1+b_q^2}+\Omega(\boldsymbol{p}+\boldsymbol{q})\right]-\frac{|\boldsymbol{p}|b_q(1-b_p^2)}{A_p}\right\}.\end{aligned} \tag{2.118}$$

One should pay attention that the two integrals in the equation above are UV divergent, giving the divergent contributions on the right-hand side

$$g^2\frac{C_F}{(4\pi)^2}b_p\left[-2\Lambda+|\boldsymbol{p}|\ln\Lambda^2(-\frac{4}{3}+\frac{1}{6})\right] \tag{2.119}$$

where in the logarithmic divergence, the contribution of the interacting quarks equation (the factor $-\frac{4}{3}$) and the transverse gluon integral (the factor $\frac{1}{6}$) are shown separated [45].

2.5.3. Quark Condensate

The static quark propagator has the form

$$G_{ij}^{mn}(\boldsymbol{x},\boldsymbol{y}) = \frac{1}{2}\left\langle[\psi_i^m(\boldsymbol{x}),\psi_j^{n\dagger}(\boldsymbol{y})]\right\rangle. \tag{2.120}$$

After Fourier transformation, the quark propagator is color diagonal and its Dirac structure can be expressed in quasi-particle form [76]

$$G(\boldsymbol{p}) = Z(\boldsymbol{p})\frac{\boldsymbol{\alpha}\cdot\boldsymbol{p} + \beta M(\boldsymbol{p})}{2\sqrt{\boldsymbol{p}^2 + M^2(\boldsymbol{p})}} \tag{2.121}$$

where $Z(\boldsymbol{p})$ is the field renormalization factor and $M(\boldsymbol{p})$ is the mass function.

The *quark condensate* is an order parameter of chiral symmetry breaking and it is expressed as

$$\rho = \langle\bar{\psi}(\boldsymbol{x})\psi(\boldsymbol{x})\rangle = -\operatorname{Tr}\langle\beta G(\boldsymbol{x},\boldsymbol{x})\rangle\,. \tag{2.122}$$

Recalling (2.121) in momentum space, the quark condensate (2.122) has the form

$$\rho = -2N_c\int đ^3q\frac{Z(\boldsymbol{q})M(\boldsymbol{q})}{\sqrt{\boldsymbol{q}^2 + M^2(\boldsymbol{q})}} \tag{2.123}$$

which obviously vanishes in the absence of a dynamically generated mass (i.e. $M(\boldsymbol{q}) = 0$).

2.5.4. Adler-Davis Equation

Neglecting the coupling to the transversal gluons ($V = 0$, $A = 1$ and $B = s$), equation (2.118) reduces to the BCS type or the well-known Adler-Davis equation which only depends on the scalar part of the kernel (i.e. $s(\boldsymbol{p})$) [92]

$$|\boldsymbol{p}|s(\boldsymbol{p}) = \frac{C_F}{2}\int đ^3qF(\boldsymbol{p}-\boldsymbol{q})\frac{s(\boldsymbol{q})(1-s^2(\boldsymbol{p})) - s(\boldsymbol{p})(1-s^2(\boldsymbol{q}))\hat{\boldsymbol{p}}\cdot\hat{\boldsymbol{q}}}{1+s^2(\boldsymbol{q})}. \tag{2.124}$$

In the Adler-Davis model $Z(\boldsymbol{p}) = 1$ in equation (2.121) and the mass function has the form [76, 92]

$$M(\boldsymbol{p}) = \frac{2|\boldsymbol{p}|s(\boldsymbol{p})}{1+s^2(\boldsymbol{p})}. \tag{2.125}$$

This expression shows that the non-vanishing scalar kernel $s(\boldsymbol{p})$ implies a non-zero quark mass and in result chiral symmetry breaking. Furthermore, by $O(3)$ invariance, the kernel $s(\boldsymbol{p})$ depends on $|\boldsymbol{p}|$ only and the same holds for our mass function $M(\boldsymbol{p})$.

Using the definition (2.125), equation (2.124) transforms to

$$M(\boldsymbol{p}) = \frac{C_F}{2}\int đ^3qF(\boldsymbol{p}-\boldsymbol{q})\frac{M(\boldsymbol{q}) - \dfrac{\boldsymbol{p}\cdot\boldsymbol{q}}{\boldsymbol{p}^2}M(\boldsymbol{p})}{E(\boldsymbol{q})}. \tag{2.126}$$

where for the quark energy we have the dispersion relation

$$E(\boldsymbol{p}) = \sqrt{\boldsymbol{p}^2 + M^2(\boldsymbol{p})}. \tag{2.127}$$

Numerical Treatment of Adler-Davis Equation

Equation (2.126) is the so-called the mass gap equation, whose non-trivial solution results in chiral symmetry breaking and mass generation. Although this equation has been already solved numerically before [92, 99, 100], I here repeated this calculation to check the numerics and prepare the later extensions. Solving equation (2.126) includes different steps some of which are explained in appendix B. Although the steps for the numerical

calculations might seem easy at the first glimpse, they play a big role in the form of the solution. Regarding the form of the Coulomb kernel

$$F(\boldsymbol{p}-\boldsymbol{q}) = \frac{8\pi\sigma_C}{(\boldsymbol{p}-\boldsymbol{q})^4} \tag{2.128}$$

although the physical scale here is the Coulomb string tension, for technical reasons we employ units as in reference [100] which removes both the Coulomb string tension and the Casimir factor from the dimensionless gap equation. In the units, equation (2.126) takes the form

$$M(\boldsymbol{p}) = \int \mathrm{d}^3 q F(\boldsymbol{p}-\boldsymbol{q}) \frac{M(\boldsymbol{q}) - \dfrac{\boldsymbol{p}\cdot\boldsymbol{q}}{\boldsymbol{p}^2} M(\boldsymbol{p})}{E(\boldsymbol{q})}. \tag{2.129}$$

All numerical factors are absorbed in the Coulomb kernel meaning we solve the equation (2.129) in energy units of $\lambda = \sqrt{C_F \cdot \sigma_C}$, where $\sigma_C = 2.5\sigma$ and $\sigma = (440\ \mathrm{MeV})^2$ is the Wilsonian string tension favored by the lattice calculations reported in [101]. This leads to the values $\lambda \approx 803$ MeV for the $SU(3)$ case and $\lambda \approx 600$ MeV for the case of $SU(2)$ group.

After fixing the scale, the second step should be shifting the loop momentum argument

$$F(\boldsymbol{p}-\boldsymbol{q}) \to F(\boldsymbol{q}) \tag{2.130}$$

which is a very logical step and that is because it reduces the probability of having singularities for $\boldsymbol{p} = \boldsymbol{q}$ in the Coulomb kernel to the minimum (i.e. $\boldsymbol{q} = 0$). However, the latter also changes the form of loop momentum argument $\boldsymbol{q} \to (\boldsymbol{q}+\boldsymbol{p})$ which leads to rewriting the equation as

$$M(\boldsymbol{p}) = \int \mathrm{d}^3 q F(\boldsymbol{q}) \frac{M(\boldsymbol{q}+\boldsymbol{p}) - \dfrac{\boldsymbol{p}\cdot(\boldsymbol{p}+\boldsymbol{q})}{\boldsymbol{p}^2} M(\boldsymbol{p})}{E(\boldsymbol{q}+\boldsymbol{p})}. \tag{2.131}$$

Another issue which might arise as the third step of the preparation of the equation for numerical calculation is the implementation of equation (2.131) in ratio or non-ratio form. Explaining the latter more, we can see that in equation (2.131) we have the mass function with the external momentum argument both in the left- and right-hand side which means that the equation can be written in the rational form by factorizing $M(\boldsymbol{p})$ from left hand side of the equation

$$M(\boldsymbol{p}) = \frac{\displaystyle\int \mathrm{d}^3 q F(\boldsymbol{q}) \frac{M(\boldsymbol{q}+\boldsymbol{p})}{E(\boldsymbol{q}+\boldsymbol{p})}}{1 + \displaystyle\int \mathrm{d}^3 q F(\boldsymbol{q}) \frac{\boldsymbol{p}\cdot(\boldsymbol{p}+\boldsymbol{q})}{\boldsymbol{p}^2 E(\boldsymbol{q}+\boldsymbol{p})}}. \tag{2.132}$$

This way of implementing equation (2.131), which has been used in [100], as it is explained in appendix B, has the advantage of a better stability during the iteration. The integrals in both denominator and numerator of equation (2.132) are divergent and introducing a regulator for both divergences automatically stabilizes the iteration. This will be worked out in more detail in chapter 3.

If we consider the more complex Dirac structure for the kernel in the next chapter, the gap equation cannot be written in ratio form. Therefore, we keep the non-ratio form of equation (2.131) to test our numerical procedure. The details of this procedure are explained in appendix B. Figure 2.7 shows the resulting mass function which is in agreement with the one calculated in [92, 100, 102, 103] where the generated mass corresponds to the

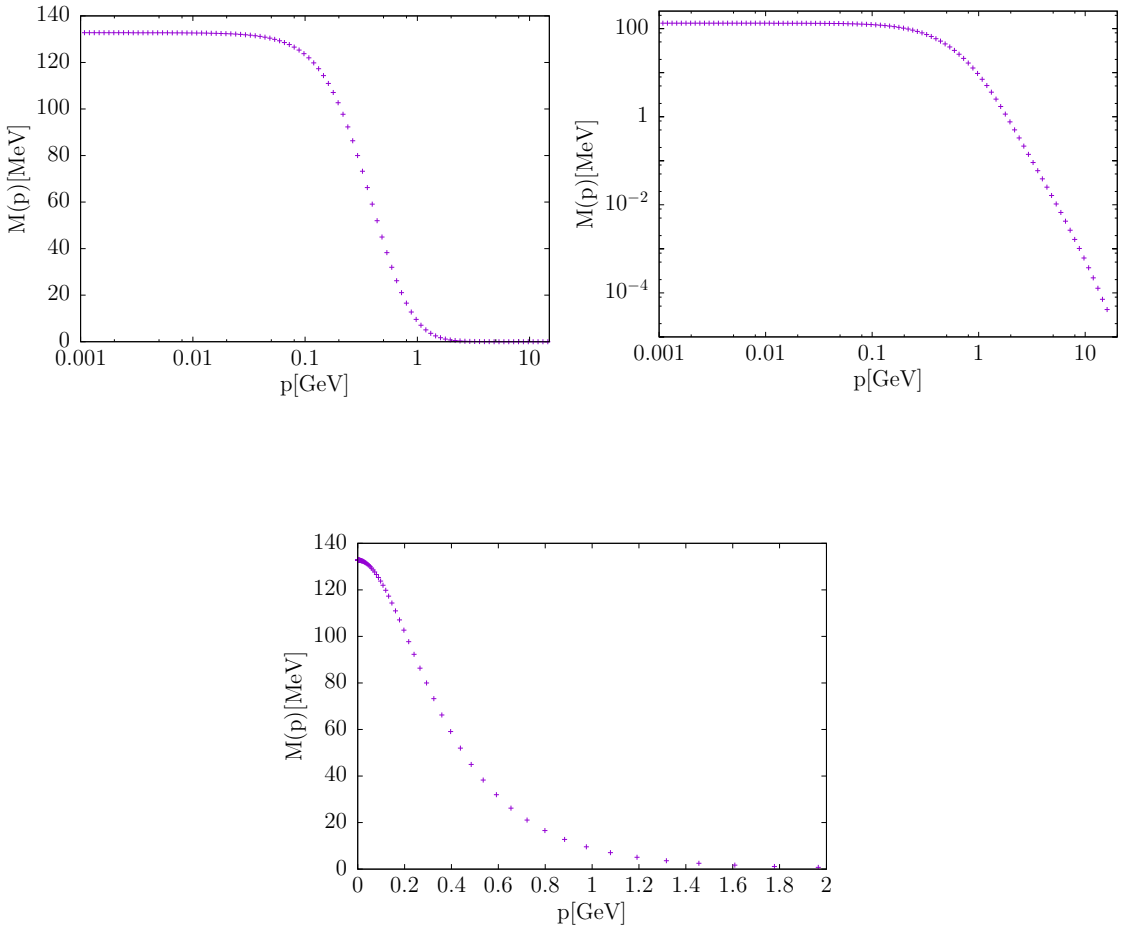

Figure 2.7.: The behavior of the mass function as the solution for equation (2.126), in different scales from left to right: logarithmic-linear, logarithmic-logarithmic and linear-linear. Equation (2.126) is solved numerically for IR cutoff $\mu \approx 0.8$ MeV and $\Lambda \approx 16$ GeV as the UV cutoff (see appendix B) giving the infrared mass value $M(0) \approx 132$ MeV.

chiral symmetry breaking. For the calculated mass function the condensate (2.123) gives the value around

$$\rho = (-185 \text{ MeV})^3 \tag{2.133}$$

which is in accordance with the result obtained in [100]. As we see in next sections, this result can be the touchstone for the later calculations in this work where we can examine the results either for the coupled equations or finite-temperature calculations by reducing them to the uncoupled, zero-temperature model.

2.6. Improved Ansatz for the Variational Kernel

In this part we present the variational method which we have used in the former section but with a more improved ansatz for the kernel as it has been introduced in [76]. Here, the necessity of the extra term in the kernel arises from the fact that it cancels the linear divergences of the UV part of the gap equation in the last section. As we already discussed in the last section, we consider the most general form of the Slater determinant and by Thouless's theorem (see reference [104] for details), we have[8]

$$|\phi_q[A]\rangle = \exp\left\{ -\int d^3(x,y)\psi_+(\boldsymbol{x})K(\boldsymbol{x},\boldsymbol{y})\psi_-(\boldsymbol{y})\right\}|0\rangle \tag{2.134}$$

where the kernel K, as before in (2.37) connects the positive to the negative energy subspace of the (single particle) Dirac Hamiltonian (2.88). The use of the Slater determinant for the quark trial vacuum allows us the application of Wick's theorem, which facilitates the evaluation of the quark expectation value. Furthermore, the norm of the fermionic wave functional (2.134) is given as [105]

$$\langle\phi_q[A]\,|\,\phi_q[A]\rangle = \det(\mathbb{1} + K^\dagger K). \tag{2.135}$$

We now let the kernel K to have a more complete structure in comparison with the form considered in the last sections

$$K(\boldsymbol{x},\boldsymbol{y}) = \beta s(\boldsymbol{x},\boldsymbol{y}) + g\int d^3z\{V(\boldsymbol{x},\boldsymbol{y};\boldsymbol{z}) + \beta W(\boldsymbol{x},\boldsymbol{y};\boldsymbol{z})\}\boldsymbol{\alpha}\cdot\mathbf{A}^a(\boldsymbol{z})\mathfrak{t}^a. \tag{2.136}$$

Here, s and V refer to the old kernel structure (2.41), (2.42) and W is the new part of the variational kernel. However, for $W = V = 0$ the ansatz for the vacuum wave functional $|\phi_q[A]\rangle$ reduces to the BCS-type ansatz that has been solved in the previous section and which has been used in references [81, 92, 99]. The coupling term proportional to W improves the former ansatz with the advantage that it removes all the linear UV divergences arising from the scalar kernel part s [76].

2.6.1. Variational Equations

As it can be noticed, in the new case we have four variational kernels s, V, W for the quarks and Ω for the gluons. Here, also by variation of the expectation value of the Hamiltonian with respect to s, we find the gap equation for the quark sector along with variation with respect to the Ω which leads us to the gluon gap equation. Furthermore, the variations with respect to V and W lead to equations which can be solved explicitly. After calculation of the expectation value of the Hamiltonian (2.77) as before but with the new ansatz (2.136) we first start with the variation with respect to the scalar part of the kernel s, which yields to the gap equation [32, 76]

$$|\boldsymbol{p}|s(\boldsymbol{p}) = I_C(\boldsymbol{p}) + I_{VV}(\boldsymbol{p}) + I_{WW}(\boldsymbol{p}) + I_{VQ}(\boldsymbol{p}) + I_{WQ}(\boldsymbol{p}) + I_E(\boldsymbol{p}). \tag{2.137}$$

The first term in the above equation has the form

$$I_C(\boldsymbol{p}) = \frac{C_F}{2}\int \bar{d}^3q\frac{V_C(\boldsymbol{p}-\boldsymbol{q})}{\Delta_s(\boldsymbol{p})}\left[s(\boldsymbol{q})(1-s^2(\boldsymbol{p})) - s(\boldsymbol{p})(1-s^2(\boldsymbol{q}))\hat{\boldsymbol{q}}\cdot\hat{\boldsymbol{p}}\right] \tag{2.138}$$

where

[8] Note that $\psi_\pm(\boldsymbol{x}) = \int d^3y\Lambda_\pm(\boldsymbol{x},\boldsymbol{y})\psi(\boldsymbol{y})$ with the positive/negative energy projector $\Lambda_\pm$.

Figure 2.8.: Diagrammatic representation of the contribution of the equation (2.138) to the quark gap equation. The diagrams in this section are adopted and reprinted with permission from [76].

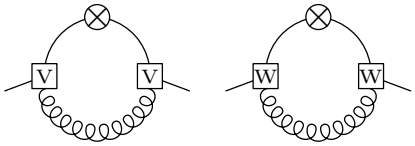

Figure 2.9.: Diagrammatic representation of equations (2.141) and (2.142).

$$\Delta_s(\boldsymbol{p}) = 1 + s(\boldsymbol{p}). \tag{2.139}$$

Equation (2.138) is the contribution of the Coulomb part of the Hamiltonian (i.e. equation (2.86)), shown diagrammatically in figure 2.8, with

$$V_C(\boldsymbol{p}) = \frac{8\pi\sigma_C}{\boldsymbol{p}^4} + \frac{g^2}{\boldsymbol{p}^2} = V_C^{IR}(\boldsymbol{p}) + V_C^{UV}(\boldsymbol{p}) \tag{2.140}$$

representing the Coulomb potential [55, 85]. Here, the reader should pay attention that the Coulomb potential above is different from the one (2.128) we considered before, which included only $V_C^{IR}(\boldsymbol{p})$. Equation (2.138) has no coupling to the transverse gluons. The second term in (2.136) contains such a coupling; it reads explicitly

$$\begin{aligned} I_{VV}(\boldsymbol{p}) = -\frac{C_F}{2}g^2 \int \mathrm{d}^3q \frac{V^2(\boldsymbol{p},\boldsymbol{q})}{\Omega(\boldsymbol{q}+\boldsymbol{p})\Delta_s(\boldsymbol{q})} X(\boldsymbol{q},\boldsymbol{p}) \Bigg[& \frac{|\boldsymbol{p}|s(\boldsymbol{p})\big[-3+s^2(\boldsymbol{p})\big]}{\Delta_s(\boldsymbol{p})} \\ & + \frac{|\boldsymbol{q}|s(\boldsymbol{p})}{\Delta_s(\boldsymbol{q})}\big[-1+s^2(\boldsymbol{q})\big] + \frac{|\boldsymbol{p}|s(\boldsymbol{q})}{\Delta_s(\boldsymbol{p})}\big[1-3s^2(\boldsymbol{p})\big] + \frac{|\boldsymbol{q}|s(\boldsymbol{q})}{\Delta_s(\boldsymbol{q})}\big[1-s^2(\boldsymbol{p})\big]\Bigg]. \end{aligned} \tag{2.141}$$

The new structure in our ansatz for the quark kernel leads to a new contribution

$$\begin{aligned} I_{WW}(\boldsymbol{p}) = -\frac{C_F}{2}g^2 \int \mathrm{d}^3q \frac{W^2(\boldsymbol{p},\boldsymbol{q})}{\Omega(\boldsymbol{q}+\boldsymbol{p})\Delta_s(\boldsymbol{q})} Y(\boldsymbol{q},\boldsymbol{p}) \Bigg[& \frac{|\boldsymbol{p}|s(\boldsymbol{p})\big[-3+s^2(\boldsymbol{p})\big]}{\Delta_s(\boldsymbol{p})} \\ & + \frac{|\boldsymbol{q}|s(\boldsymbol{p})}{\Delta_s(\boldsymbol{q})}\big[-1+s^2(\boldsymbol{q})\big] - \frac{|\boldsymbol{p}|s(\boldsymbol{q})}{\Delta_s(\boldsymbol{p})}\big[1-3s^2(\boldsymbol{p})\big] - \frac{|\boldsymbol{q}|s(\boldsymbol{q})}{\Delta_s(\boldsymbol{q})}\big[1-s^2(\boldsymbol{p})\big]\Bigg] \end{aligned} \tag{2.142}$$

resulting from the first part of equation (2.93). Equations (2.141) and (2.142) are shown diagrammatically in figure 2.9. Furthermore,

$$I_{VQ}(\boldsymbol{p}) = \frac{C_F}{2}g^2 \int \mathrm{d}^3q \frac{V(\boldsymbol{q},\boldsymbol{p})}{\Omega(\boldsymbol{q}+\boldsymbol{p})\Delta_s(\boldsymbol{q})} X(\boldsymbol{p},\boldsymbol{q})\Big[s(\boldsymbol{q})(1-s^2(\boldsymbol{p})) - 2s(\boldsymbol{p})\Big] \tag{2.143}$$

$$I_{WQ}(\boldsymbol{p}) = \frac{C_F}{2}g^2 \int \mathrm{d}^3q \frac{W(\boldsymbol{q},\boldsymbol{p})}{\Omega(\boldsymbol{q}+\boldsymbol{p})\Delta_s(\boldsymbol{q})} Y(\boldsymbol{p},\boldsymbol{q})\Big[1-s^2(\boldsymbol{p}) - 2s(\boldsymbol{p})s(\boldsymbol{q})\Big] \tag{2.144}$$

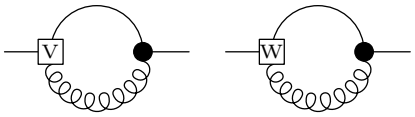

Figure 2.10.: Diagrammatic representation of the equations (2.143) and (2.144).

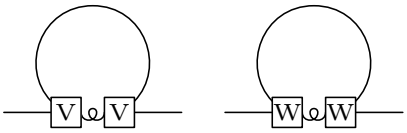

Figure 2.11.: Diagrammatic representation of the two terms on the right hand-side of the equation (2.145).

are the contributions from the quark-gluon coupling in the Dirac Hamiltonian (2.87) which we did not consider in the Adler-Davis model. Equations (2.143) and (2.144) are shown diagrammatically in figure 2.10. Additionally,

$$I_E(\boldsymbol{p}) = \frac{C_F}{2} g^2 s(\boldsymbol{p}) \int đ^3 q \frac{V^2(\boldsymbol{q},\boldsymbol{p}) X(\boldsymbol{p},\boldsymbol{q})}{\Delta_s(\boldsymbol{q})} + \frac{C_F}{2} g^2 s(\boldsymbol{p}) \int đ^3 q \frac{W^2(\boldsymbol{q},\boldsymbol{p}) Y(\boldsymbol{p},\boldsymbol{q})}{\Delta_s(\boldsymbol{q})} \tag{2.145}$$

shown diagrammatically in figure 2.11, is the result from the action of the gluonic kinetic energy (2.82) on the quark wave functional. Here, we have used the definitions

$$X(\boldsymbol{p},\boldsymbol{q}) = 1 - \left[\hat{\boldsymbol{p}} \cdot (\widehat{\boldsymbol{p}+\boldsymbol{q}})\right]\left[\hat{\boldsymbol{q}} \cdot (\widehat{\boldsymbol{p}+\boldsymbol{q}})\right] \tag{2.146}$$

and

$$Y(\boldsymbol{p},\boldsymbol{q}) = 1 + \left[\hat{\boldsymbol{p}} \cdot (\widehat{\boldsymbol{p}+\boldsymbol{q}})\right]\left[\hat{\boldsymbol{q}} \cdot (\widehat{\boldsymbol{p}+\boldsymbol{q}})\right]. \tag{2.147}$$

where $\widehat{\boldsymbol{p}+\boldsymbol{q}}$ is the unit vector in the direction of $\boldsymbol{p}+\boldsymbol{q}$.

After finding the gap equation (2.137) for the quarks, one can derive the equations for the vector parts of the kernel. Starting with variation with respect to the V, we have

$$V(\boldsymbol{p},\boldsymbol{q}) = \frac{1 + s(\boldsymbol{p})s(\boldsymbol{q})}{|\boldsymbol{p}|U(\boldsymbol{p})\Delta_+(\boldsymbol{p},\boldsymbol{q}) + |\boldsymbol{q}|U(\boldsymbol{q})\Delta_+(\boldsymbol{q},\boldsymbol{p}) + \Omega(\boldsymbol{p}+\boldsymbol{q})} \tag{2.148}$$

and also for W

$$W(\boldsymbol{p},\boldsymbol{q}) = \frac{s(\boldsymbol{p}) + s(\boldsymbol{q})}{|\boldsymbol{p}|U(\boldsymbol{p})\Delta_-(\boldsymbol{p},\boldsymbol{q}) + |\boldsymbol{q}|U(\boldsymbol{q})\Delta_-(\boldsymbol{q},\boldsymbol{p}) + \Omega(\boldsymbol{p}+\boldsymbol{q})} \tag{2.149}$$

where

$$\Delta_\pm(\boldsymbol{p},\boldsymbol{q}) = 1 - s^2(\boldsymbol{p}) \pm 2s(\boldsymbol{p})s(\boldsymbol{q}) \tag{2.150}$$

and

$$U(\boldsymbol{p}) = \frac{1}{\Delta_s(\boldsymbol{p})}. \tag{2.151}$$

Equation (2.148) is considerably different from the result obtained in [105] where due to the approximation made there the vector kernel depends only on one momentum. Furthermore, considering the trivial solution (i.e. $s = 0$, $\Omega(\boldsymbol{p}) = |\boldsymbol{p}|$) the expression (2.148) reduces to the perturbative result for the vector part [75]

$$V_0(\boldsymbol{p},\boldsymbol{q}) = \frac{1}{|\boldsymbol{p}| + |\boldsymbol{q}| + |\boldsymbol{p}+\boldsymbol{q}|}. \tag{2.152}$$

Finally, looking to the kernel W with a similar structure as kernel V, we notice that in the limit of $s = 0$, it vanishes which shows the non-perturbative properties of that. If we assume that the scalar kernel s is vanishing fast enough in the UV as it is expected from asymptotic freedom, one can find that the loop terms on the right hand-side of the equation (2.137) containing vector V yield the UV divergence

$$\frac{C_F}{16\pi^2}g^2 s(\boldsymbol{p})\bigg[-2\Lambda+|\boldsymbol{p}|\ln\frac{\Lambda}{\mu}(-\frac{2}{3}+4U(\boldsymbol{p}))\bigg]. \tag{2.153}$$

At the same time, the loop terms which contain the vector kernel W give

$$\frac{C_F}{16\pi^2}g^2 s(\boldsymbol{p})\bigg[2\Lambda+|\boldsymbol{p}|\ln\frac{\Lambda}{\mu}(\frac{10}{3}-4U(\boldsymbol{p}))\bigg]. \tag{2.154}$$

Furthermore, the loop contribution of the Coulomb potential (i.e. (2.138)) gives rise to the UV divergence

$$-\frac{C_F}{16\pi^2}g^2|\boldsymbol{p}|s(\boldsymbol{p})\ln\frac{\Lambda}{\mu}\times\frac{8}{3}. \tag{2.155}$$

The important point here is that the sum of these UV divergent contributions vanish so that the quark gap equation is in fact UV finite. The cancellation of the linear UV divergences requires the inclusion of the Dirac structure of the quark-gluon coupling in the kernel in (2.136). Moreover, in order to cancel the logarithmic UV divergences, we need to include the UV part of the Coulomb potential (i.e. $V_C^{UV}(\boldsymbol{p})$) in (2.140).

2.6.2. Mass Function

If we neglect the coupling of the quarks to the transverse gluons, the mass function is defined as before in equation (2.126) [92]. However, for convenience in the calculations, we use the same definition for the mass function (2.125) which yields the gap equation (2.137) to have the form

$$M(\boldsymbol{p})=\mathcal{I}_C(\boldsymbol{p})+\mathcal{I}_{VV}(\boldsymbol{p})+\mathcal{I}_{WW}(\boldsymbol{p})+\mathcal{I}_{VQ}(\boldsymbol{p})+\mathcal{I}_{WQ}(\boldsymbol{p})+\mathcal{I}_E(\boldsymbol{p}) \tag{2.156}$$

where, by recalling the definition for the energy $E(\boldsymbol{p})$ in (2.127), the terms in the right hand-side are given as

$$\mathcal{I}_C(\boldsymbol{p})=\frac{C_F}{2}\int đ^3q V_C(\boldsymbol{p}+\boldsymbol{q})\frac{M(\boldsymbol{q})+M(\boldsymbol{p})\frac{\boldsymbol{p}\cdot\boldsymbol{q}}{\boldsymbol{p}^2}}{E(\boldsymbol{p})} \tag{2.157}$$

Moreover, for the remaining contributions to the gap equation we have

$$\begin{aligned}\mathcal{I}_{VV}(\boldsymbol{p})=&-\frac{C_F}{2}g^2\int đ^3q\frac{V^2(\boldsymbol{p},\boldsymbol{q})X(\boldsymbol{p},\boldsymbol{q})}{\Omega(\boldsymbol{p}+\boldsymbol{q})}\bigg\{-\frac{E(\boldsymbol{q})+|\boldsymbol{q}|}{2E(\boldsymbol{q})}M(\boldsymbol{p})\frac{E(\boldsymbol{p})+2|\boldsymbol{p}|}{E(\boldsymbol{p})}\\&-\boldsymbol{q}^2\frac{E(\boldsymbol{q})+|\boldsymbol{q}|}{2E^2(\boldsymbol{q})}\frac{M(\boldsymbol{p})}{|\boldsymbol{p}|}+\frac{M(\boldsymbol{q})}{2E(\boldsymbol{q})}\frac{E(\boldsymbol{p})+|\boldsymbol{p}|}{E(\boldsymbol{p})}[-E(\boldsymbol{p})+2|\boldsymbol{p}|]+|\boldsymbol{q}|M(\boldsymbol{q})\frac{E(\boldsymbol{q})+|\boldsymbol{q}|}{2E^2(\boldsymbol{q})}\bigg\}\end{aligned} \tag{2.158}$$

and

$$\begin{aligned}\mathcal{I}_{WW}(\boldsymbol{p})=&-\frac{C_F}{2}g^2\int đ^3q\frac{W^2(\boldsymbol{p},\boldsymbol{q})Y(\boldsymbol{p},\boldsymbol{q})}{\Omega(\boldsymbol{p}+\boldsymbol{q})}\bigg\{-\frac{E(\boldsymbol{q})+|\boldsymbol{q}|}{2E(\boldsymbol{q})}M(\boldsymbol{p})\frac{E(\boldsymbol{p})+2|\boldsymbol{p}|}{E(\boldsymbol{p})}\\&-\boldsymbol{q}^2\frac{E(\boldsymbol{q})+|\boldsymbol{q}|}{2E^2(\boldsymbol{q})}\frac{M(\boldsymbol{p})}{|\boldsymbol{p}|}+\frac{M(\boldsymbol{q})}{2E(\boldsymbol{q})}\frac{E(\boldsymbol{p})+|\boldsymbol{p}|}{E(\boldsymbol{p})}[-E(\boldsymbol{p})+2|\boldsymbol{p}|]+|\boldsymbol{q}|M(\boldsymbol{q})\frac{E(\boldsymbol{q})+|\boldsymbol{q}|}{2E^2(\boldsymbol{q})}\bigg\}.\end{aligned} \tag{2.159}$$

Furthermore,

$$\mathcal{I}_{VQ}(\boldsymbol{p}) = \frac{C_F}{2} g^2 \int \bar{d}^3 q \frac{V(\boldsymbol{p},\boldsymbol{q}) X(\boldsymbol{p},\boldsymbol{q})}{\Omega(\boldsymbol{p}+\boldsymbol{q})} \left\{ \frac{M(\boldsymbol{q})}{E(\boldsymbol{q})} - \frac{E(\boldsymbol{q})+|\boldsymbol{q}|}{E(\boldsymbol{q})} \frac{M(\boldsymbol{p})}{|\boldsymbol{p}|} \right\} \tag{2.160}$$

and

$$\mathcal{I}_{WQ}(\boldsymbol{p}) = \frac{C_F}{2} g^2 \int \bar{d}^3 q \frac{V(\boldsymbol{p},\boldsymbol{q}) Y(\boldsymbol{p},\boldsymbol{q})}{\Omega(\boldsymbol{p}+\boldsymbol{q})} \left\{ \frac{E(\boldsymbol{q})+|\boldsymbol{q}|}{E(\boldsymbol{q})} - \frac{M(\boldsymbol{q})}{E(\boldsymbol{q})} \frac{M(\boldsymbol{p})}{|\boldsymbol{p}|} \right\}. \tag{2.161}$$

Finally

$$\mathcal{I}_{E}(\boldsymbol{p}) = \frac{C_F}{2} g^2 \frac{M(\boldsymbol{p})}{|\boldsymbol{p}|} \int \bar{d}^3 q \Big\{ V^2(\boldsymbol{p},\boldsymbol{q}) X(\boldsymbol{p},\boldsymbol{q}) + W^2(\boldsymbol{p},\boldsymbol{q}) Y(\boldsymbol{p},\boldsymbol{q}) \Big\} \frac{E(\boldsymbol{q})+|\boldsymbol{q}|}{2E(\boldsymbol{q})}. \tag{2.162}$$

All contributions on the right hand-side of the gap equation (2.156) except $\mathcal{I}_C$ contain a prefactor g^2 and thus vanish if $g \to 0$. Therefore, the gap equation (2.156) reduces to the Adler-Davis model from the previous section in the limit $g \to 0$. In addition, equations (2.148) and (2.149) for the vector kernels V and W yield

$$\begin{aligned} V(\boldsymbol{p},\boldsymbol{q}) = & \left(1 + \frac{E(\boldsymbol{p})-|\boldsymbol{p}|}{M(\boldsymbol{p})} \frac{E(\boldsymbol{q})-|\boldsymbol{q}|}{M(\boldsymbol{q})} \right) \\ & \times \left\{ \frac{\boldsymbol{p}^2}{E(\boldsymbol{p})} \left[1 + \frac{M(\boldsymbol{p})}{|\boldsymbol{p}|} \frac{E(\boldsymbol{q})-|\boldsymbol{q}|}{M(\boldsymbol{q})} \right] + \frac{\boldsymbol{q}^2}{E(\boldsymbol{q})} \left[1 + \frac{M(\boldsymbol{q})}{|\boldsymbol{q}|} \frac{E(\boldsymbol{p})-|\boldsymbol{p}|}{M(\boldsymbol{p})} \right] + \Omega(\boldsymbol{p}+\boldsymbol{q}) \right\}^{-1} \end{aligned} \tag{2.163}$$

and

$$\begin{aligned} W(\boldsymbol{p},\boldsymbol{q}) = & \left(\frac{E(\boldsymbol{p})-|\boldsymbol{p}|}{M(\boldsymbol{p})} \frac{E(\boldsymbol{q})-|\boldsymbol{q}|}{M(\boldsymbol{q})} \right) \\ & \times \left\{ \frac{\boldsymbol{p}^2}{E(\boldsymbol{p})} \Big[1 - \frac{M(\boldsymbol{p})}{|\boldsymbol{p}|} \frac{E(\boldsymbol{q})-|\boldsymbol{q}|}{M(\boldsymbol{q})} \Big] + \frac{\boldsymbol{q}^2}{E(\boldsymbol{q})} \Big[1 - \frac{M(\boldsymbol{q})}{|\boldsymbol{q}|} \frac{E(\boldsymbol{p})-|\boldsymbol{p}|}{M(\boldsymbol{p})} \Big] + \Omega(\boldsymbol{p}+\boldsymbol{q}) \right\}^{-1}. \end{aligned} \tag{2.164}$$

2.7. Numerical Solution

In this section we want to explain how to solve the gap equation (2.156) for the mass function, $M(\boldsymbol{p})$. The techniques are the same as which have been used to solve the Adler-Davis equation (2.126). This means that as before, we use the iterative method to solve this equation. Moreover, as it is explained in appendix B, the function from which we start the iteration can be a constant. However, in the case of equation (2.156), it is also possible to use the solution of the equation (2.126) as the starting function which should lead to less iterations. Nonetheless the result obtained with a non-constant starting function is the same for the mass function which is a good test for our numerical procedure. After shifting the loop momentum and transforming the integral to spherical coordinates and choosing the IR and UV cutoffs[9], here we are also able to use the Gauss-Legendre quadrature for taking the integrals. Furthermore, the interpolation and extrapolation methods, as it is explained in appendix B, are the same as the ones we used for solving equation (2.131).

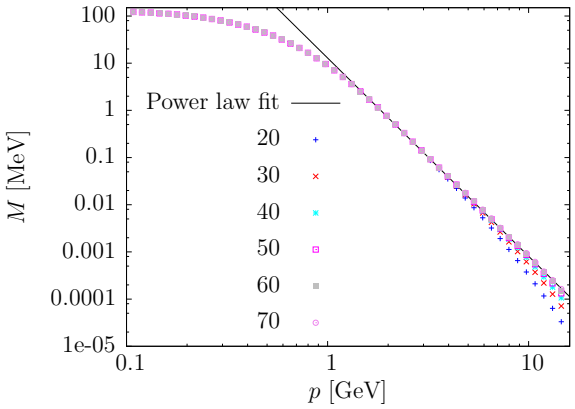

Figure 2.12.: The solution to the equation (2.156) for $g = 0$ (i.e. equation (2.131)) for different numbers of sampling points in the angular integral. The straight line is a fit to the UV part of the solution for the largest number of sampling points (momenta is between 1.7 GeV$< p <$ 3 GeV).

Moreover, in the numerical calculations the value for the Coulomb string tension has been fixed to $\sigma_C = 2.5\sigma$ as before.

One of the interesting aspects of the numerical calculation of the integral equation we deal with, in both the coupled and uncoupled case, is that the number of the nodes we choose for the angular integration effects the behavior of the UV part of the solution, as can be observed in the figure 2.12. However, the solution converges in the UV once the angular integral is carried out with 70 nodes or more, and the precise number is irrelevant for the calculation of the quark condensate below.

As it is shown in figures 2.13 and 2.14 for the case of including or discarding the coupling g there is almost no change in the IR part of the solution for the mass function, although the UV part and the mid-range momentum part change. This is because of the dominance of the IR part of the Coulomb potential ($V_C^{IR} \propto 1/\boldsymbol{p}^4$) which plays the main role in the chiral symmetry breaking. In simpler terms, it means that if we neglect the confining part of the Coulomb potential by putting $\sigma_C = 0$, the solution for the gap equation would be trivial (i.e. $M = 0$). Moreover, the coupling constant g is adjusted in our calculations in order to reproduce the phenomenological value of the quark condensate $\langle\bar{\psi}\psi\rangle \simeq (-235 \text{ MeV})^3$ [106] which is higher than the value $(-185 \text{ MeV})^3$ obtained for the case without coupling $g = 0$ (i.e. the Adler Davis equation). This yields $g \simeq 2.1$ which corresponds to a value of the running coupling constant, calculated in [55] from ghost-gluon vertex, in the mid-momentum regime [32]. Note that the coupling g in our case is a fixed parameter that does not run due to the absence of divergences in the gap equation. Furthermore, for the calculation of the quark condensate we neglected the terms arising from the quark-gluon coupling in the definition of the quark propagator (2.120) [32, 76]. Hence, in our calculations the expression for the quark condensate and mass function are the same as in the Adler-Davis model. Our numerical results for the mass function (figure 2.125) can be fitted for small and mid-momenta by the function

$$M_{fit}^{IR}(p) = \frac{m_0}{1 + (\frac{p}{m_A})^A + (\frac{p}{m_B})^B} \tag{2.165}$$

[9] As for equation (2.126), the cutoffs for IR and UV are considered to be 0.8 MeV and 16 GeV, respectively.

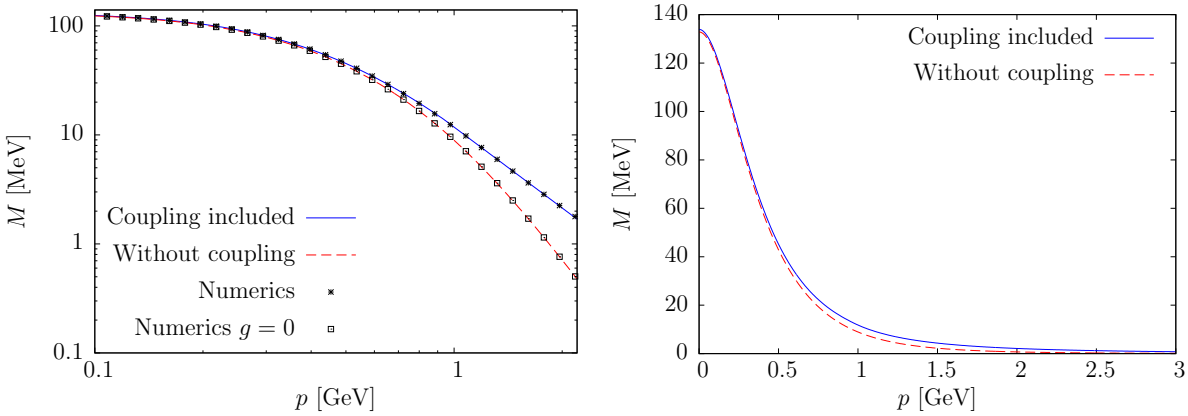

Figure 2.13.: Numerical solution of the quark gap equation (2.156) for the mass function M defined by (2.125) for both cases with coupling ($g \simeq 2.1$) and without coupling ($g = 0$) in logarithmic (left) and linear (right) scale. As it can be observed in the logarithmic plot, in the case of the coupled and uncoupled equation a difference occurs only in the UV part. However in the linear scale both solutions have nearly the same behavior.

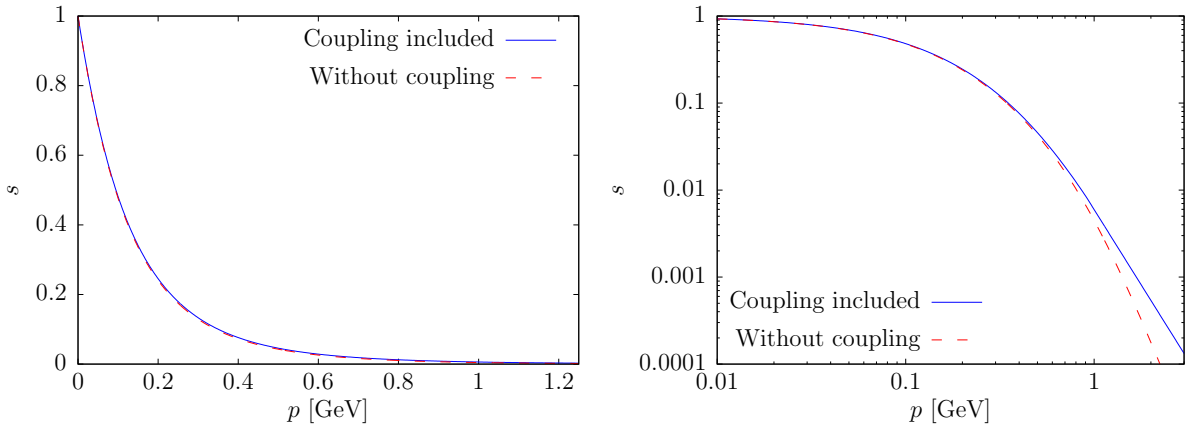

Figure 2.14.: Numerical solution for the quark gap equation (2.156) for the scalar kernel s for $g \simeq 2.1$ and $g = 0$ on logarithmic (left) and linear scale (right).

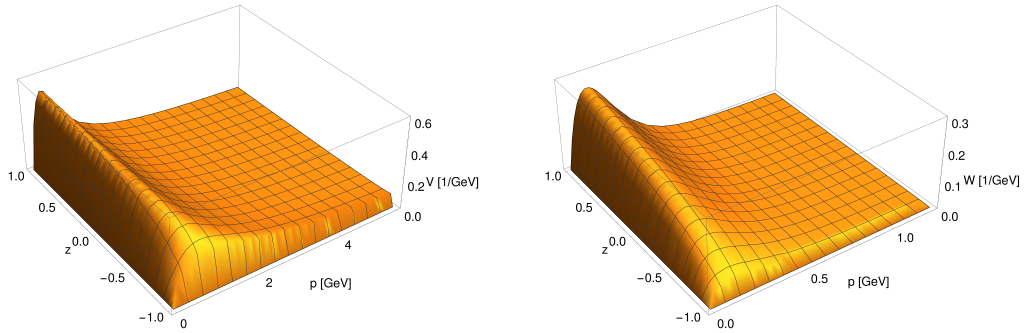

Figure 2.15.: The numerical solutions for the vector kernels $V(\boldsymbol{p}, \boldsymbol{q})$ and $W(\boldsymbol{p}, \boldsymbol{q})$ as the function of $|\boldsymbol{p}| = |\boldsymbol{q}|$ and $z = \cos \sphericalangle(\boldsymbol{p}, \boldsymbol{q})$ for $g \simeq 2.1$ obtained from solving the equation (2.156).

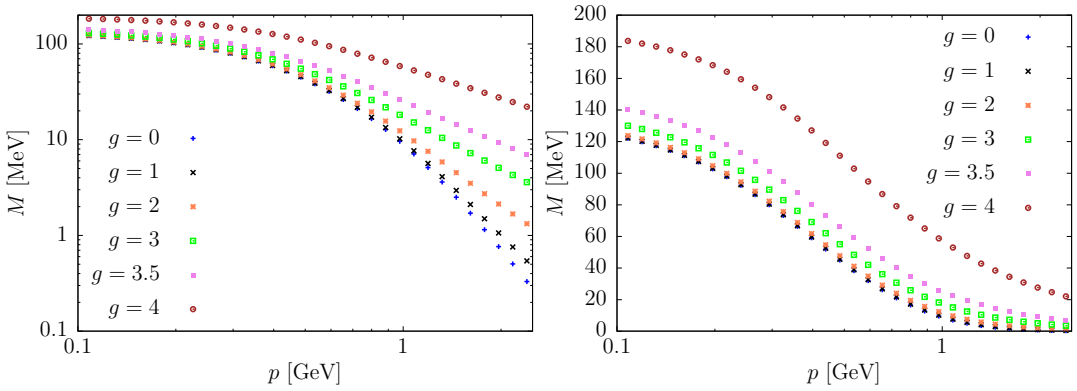

Figure 2.16.: Left: Mass functions for different values of the coupling g. As it can be seen, the mass function generally increases with the coupling g. Right: Mass function plotted for the same values of the coupling g in log-line coordinates.

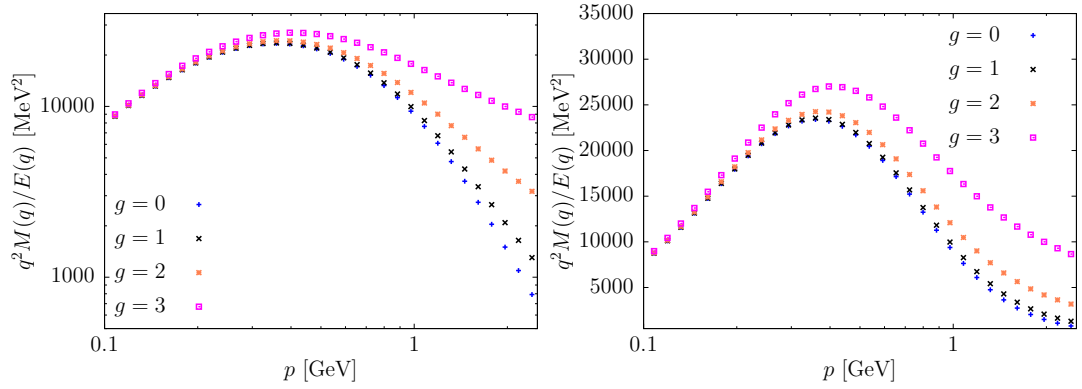

Figure 2.17.: Left: The integrand in the condensate formula (2.123) plotted for different values of coupling constant g. Right: The same plot in log-line coordinates. As it can be observed larger values for g results in larger values for the integrand in (2.123) and as a consequence increasing values for the condensate.

where for the chosen value $g \simeq 2.1$ the optimized fit parameters are

$$\begin{aligned} m_0 &= 134 \text{ MeV} \qquad m_A = 674 \text{ MeV} \qquad m_B = 388 \text{ MeV} \\ A &= 3.598 \qquad\quad B = 1.915. \end{aligned} \tag{2.166}$$

For the large momentum part ($p > 1$ GeV) we use the power-law fit

$$M_{fit}^{UV}(p) = m_C \left(\frac{p}{m_C}\right)^C \tag{2.167}$$

where the fit parameters read $m_C = 278$ MeV and $C = -2.467$. From equation (2.165), we can conclude that the IR limit of the mass function is given by $M(p \to 0) \simeq 134$ MeV which is almost the same value as for the Adler-Davis model (133 MeV). However, the UV exponent C obtained for (2.167) is higher than the numerical solution for the uncoupled case[10]. Furthermore, as it can be observed in table 2.1 the larger values of coupling

[10]However, $M(0)$ only differs significantly from its $g = 0$ value at higher values of the coupling $g > 5$.

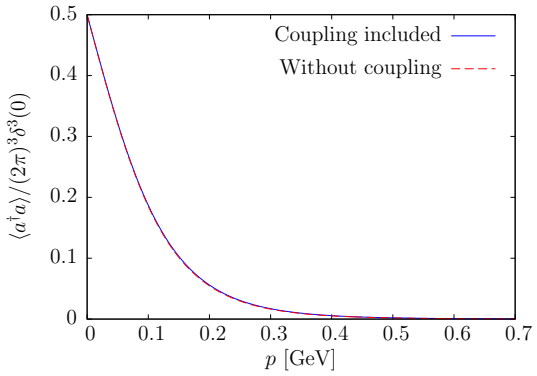

Figure 2.18.: Comparison between the density numbers of the quark states, for the coupled ($g \simeq 2.1$) and uncoupled ($g = 0$) cases.

constant g lead to larger values for condensate and that is the consequence of the behavior of the integrand in (2.123), as it is shown in figure 2.17, depending on the mass function M. Using the algebraic fit (2.165), (2.167), we find vector kernels $V(\boldsymbol{p},\boldsymbol{q})$ and $W(\boldsymbol{p},\boldsymbol{q})$ as shown in figure 2.15 for $|\boldsymbol{q}| = |\boldsymbol{p}|$. Although the shape of both kernels is identical, the non-perturbative kernel (i.e. $W(\boldsymbol{p},\boldsymbol{q})$) is significantly smaller than the V kernel, which is due to choice of $|\boldsymbol{p}| = |\boldsymbol{q}|$ leading W to vanish faster in the UV. However, for the general case of $|\boldsymbol{p}| \neq |\boldsymbol{q}|$ both kernels vanish $\sim 1/|\boldsymbol{p}|$ for $|\boldsymbol{p}| \to \infty$ [76].

g	0	1	2	3
$\rho^{1/3}$	-185 MeV	-194 MeV	-225 MeV	-298 MeV

Table 2.1.: Different approximated values of condensate (2.123) shown in figure 2.17.

At last, figure 2.18 shows the occupation number density of quark states which has been calculated in [76]

$$\frac{\langle a^{s,m\dagger}(\boldsymbol{p})a^{s,m}(\boldsymbol{p})\rangle}{(2\pi)^3\delta^3(0)} = U(\boldsymbol{p})s^2(\boldsymbol{p}) \tag{2.168}$$

where U is given by (2.151).

On linear scale, the results for $g \simeq 2.1$ and $g = 0$ are almost identical. Note that for the chosen ansatz for the vacuum wave functional, the densities of occupied quark and anti-quark states, agree. Furthermore, we noticed the important role of the Coulomb string tension σ_C in the chiral symmetry breaking. If we discard the linearly rising part of the Coulomb potential (i.e. $\sigma_C = 0$) in our equations, chiral symmetry turns out to be not spontaneously broken. Assuming the Coulomb string tension $\sigma_C = 2.5\sigma$ we reproduced the phenomenological value for the quark condensate which is the value of $(-235\ \text{MeV})^3$ for the chosen quark-gluon coupling constant $g \simeq 2.1$.

2.8. Summary

In this chapter, we used the variational method in the Hamiltonian approach to quantum field theory. In addition to reviewing the variational method for Yang-Mills theory, we studied Hamiltonian Dyson-Schwinger equations of QCD, where the ansatz for the vacuum wave functional was including one Dirac structure for the quark-gluon coupling. In the

absence of the coupling to the transverse gluons, the gap equation reduced to the Adler-Davis equation (2.126), and we solved it numerically as a starting point for the further calculations. Furthermore, we derived the gap equation (2.137) for the vacuum energy up to including two-loop order for which the considered vacuum wave functional included a different Dirac structure for the quark-gluon coupling. The advantage of this additional structure in the variational ansatz was the cancellation of the linear UV divergences in the resulting gap equation. We solved the coupled gap equation (2.156) numerically and discussed the results. The findings show a considerable improvement of the strength of the chiral symmetry breaking (quark condensate), which agrees with standard lattice results at a reasonable coupling strength of $g \approx 2.1$.

3. QCD at Finite Temperature

3.1. Introduction

Although the first motivations for studying quantum field theory at finite temperature were initiated by cosmological problems [107, 108], the point of interest for us for the treatment of quantum field theory at finite temperature is to understand the QCD phase diagram [109–112]. The study of the baryonic matter at finite temperature and high chemical potential cannot be performed on the lattice because of the sign problem [29, 113, 114]. Thus, the ideal approaches for us are non-perturbative continuum approaches in which we do not deal with the lattice calculation methods and it gives us more hope to investigate the QCD phase diagram [56]. In order to deal with quantum field theory at finite temperature the basic quantity of interest is the partition function. In the continuum approach, it is possible to calculate the partition function from the functional integral representation in perturbation theory. Moreover, the leading-order perturbative results for the partition function can be expanded to beyond perturbation theory by replacing the bare propagators with the non-perturbative ones [68, 115–117]. Among all possible approaches which can be used for the calculation of the partition function, the Hamiltonian approach is one of the most efficient and transparent methods, in particular since the calculations can be done without computing the full thermal spectrum. Instead, we follow the approach of reference [68] and compactify one spatial dimension. The vacuum wave functional defined on the spatial manifold $\mathbb{R}^2 \times S^1(\beta)$, contains the whole temperature behavior [68]. Therefore, in this approach it is just enough to calculate the vacuum energy in order to find the grand canonical partition function. We apply this approach to the fermionic system because this formulation was already used for the case of Yang-Mills fields in [118, 119] and the results were consistent with the ones obtained from the grand canonical approach [120].

In this chapter, after a quick review of *thermal quantum mechanics*, we introduce the setting for the Hamiltonian approach at finite temperature which includes the compactification of a Euclidean dimension and appearance of the *Matsubara frequencies* [121] arising after the change of the framework to the Euclidean QCD. Furthermore, we explain the treatment of the previously solved Adler-Davis equation (2.126) at finite temperature which leads us to deal with a series of the gap equations, each for one Matsubara frequency. Although solving the compactified gap equation for each Matsubara frequency is possible at very high temperatures, it is not useful since the whole calculation is dominated by the pole arising from Coulomb kernel for a single Matsubara frequency. Therefore, we *Poisson resum* the Matsubara series and after introducing a method in order to carry the divergent part of integrands out, we solve the quark gap equation at finite temperature. Furthermore, we calculate the quark condensate as the order parameter of chiral symmetry breaking for different temperatures. We find a second order chiral phase transition with a critical temperature around 90 MeV.

The first part of this chapter in which we explain the compactification approach to quantum field theory, is adopted from [68] while the solution of the Adler-Davis equation at finite temperature is original research of this thesis published in [122].

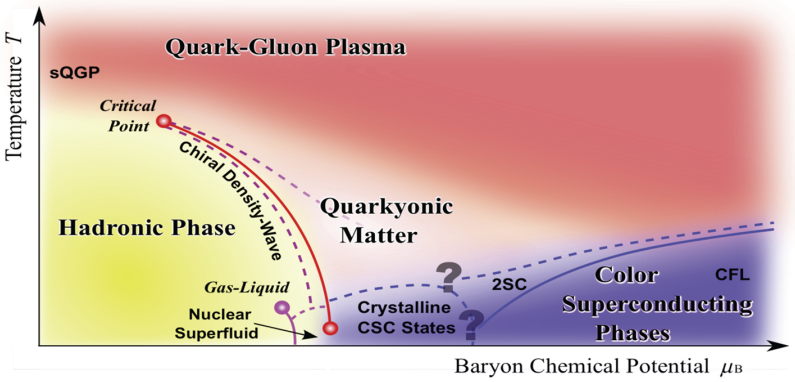

Figure 3.1.: The scheme of the QCD phase diagram, depending on the temperature T and baryonic chemical potential μ_B. The figure is adopted and reprinted with permission from [123].

3.2. Quantum Mechanics at Finite Temperature and Matsubara Frequencies

In order to describe a quantum mechanical system at non-zero temperature we deal with canonical ensembles where we consider just the energy change for the system for a fixed number of particles and volume at fixed temperature. For a system described by the Hamiltonian H at finite temperature, we introduce the partition function

$$Z = \mathrm{Tr}[e^{-\beta H}] \tag{3.1}$$

where $\beta = 1/T$ is the inverse of the temperature in units of Boltzmann's constant (i.e. $k_B = 1$). The partition function is the key to the finite temperature physics because all thermodynamical quantities can be generated from it. For instance by defining the free energy of a system $F = -T\ln(Z)$, we have

$$S = -\frac{\partial F}{\partial T} \tag{3.2}$$

$$P = -\frac{\partial F}{\partial V} \tag{3.3}$$

where S is the entropy and P is the average pressure.

In quantum mechanics at finite temperature, we deal with the thermal expectation value which is given by

$$\langle O \rangle_\beta = \frac{1}{Z} \sum_n \langle n|O|n\rangle \, e^{-\beta H} \tag{3.4}$$

where one can see the partition function appearing in the theory. Nevertheless, one should pay attention that the above definitions are for the canonical ensemble which is a closed system with a fixed number N of particles. In the case of an open system where the number of particles is not fixed so we deal with grand canonical ensemble, for which the grand canonical partition function has the form

$$\mathcal{Z}(\beta, \mu) = \mathrm{Tr}\, e^{-\beta(H - N\mu)}. \tag{3.5}$$

One of the fundamental relations in finite temperature theory is the *Kubo-Martin-Schwinger* (KMS) relation [124, 125] which defines the state of the system in thermal

equilibrium. Furthermore, it shows the necessity of the definition of the imaginary time component in the thermal quantum field theory as the entrance to the Euclidean quantum field theory. If one considers the definition of the thermal two-point correlation function in the Cartesian coordinates [126]

$$\begin{aligned}\langle\psi(\boldsymbol{x},t)\psi(\boldsymbol{y},0)\rangle_\beta &= \frac{1}{Z}\,\mathrm{Tr}[e^{-\beta H}\psi(\boldsymbol{x},t)\psi(\boldsymbol{y},0)]\\ &= \frac{1}{Z}\,\mathrm{Tr}[e^{-\beta H}e^{\beta H}\psi(\boldsymbol{x},t)\psi(\boldsymbol{y},0)e^{-\beta H}]\\ &= \frac{1}{Z}\,\mathrm{Tr}[e^{-\beta H}e^{i(-i\beta H)}\psi(\boldsymbol{x},t)\psi(\boldsymbol{y},0)e^{-i(-i\beta H)}]\\ &= \frac{1}{Z}\,\mathrm{Tr}[e^{-\beta H}\psi(\boldsymbol{x},t)\psi(\boldsymbol{y},-i\beta)]\\ &= \frac{1}{Z}\,\mathrm{Tr}[e^{-\beta H}\psi(\boldsymbol{y},-i\beta)\psi(\boldsymbol{x},t)]\\ &= \langle\psi(\boldsymbol{y},-i\beta)\psi(\boldsymbol{x},t)\rangle_\beta\end{aligned} \tag{3.6}$$

it can be seen that the imaginary time plays the role of temperature. Defining the imaginary time τ by

$$t = -i\tau \tag{3.7}$$

relation (3.6) can be rewritten as

$$\langle\phi(\boldsymbol{x},\tau)\phi(\boldsymbol{y},0)\rangle_\beta = \langle\phi(\boldsymbol{y},\beta)\phi(\boldsymbol{x},\tau)\rangle_\beta\,. \tag{3.8}$$

Here, $\phi(\boldsymbol{x},\tau) = \psi(\boldsymbol{x},-i\tau)$ is the state continued to imaginary times (Euclidean space). The relation (3.8) is called the KMS relation. The fields in above equation can have the relation

$$\phi(\boldsymbol{x},0) = \pm\phi(\boldsymbol{x},\beta) \tag{3.9}$$

where the "$\pm$" signs refer to the fields which commute or anticommute with each other, or in another words, bosons and fermions. The KMS relation shows that at imaginary time, the fields are periodic or anti-periodic. Writing the discrete Fourier transformation in the imaginary time case, we have

$$\phi(\boldsymbol{x},\tau) = \sum_n \phi(\boldsymbol{x},\omega_n)\exp(i\omega_n\tau) \tag{3.10}$$

where according to (3.9) ω_n can only take discrete values for an integer $n \in \mathbb{Z}$

$$\omega_n = \begin{cases}\frac{2n\pi}{\beta}, & \text{bosonic fields}\\ \frac{2(n+1)\pi}{\beta}, & \text{fermionic fields.}\end{cases} \tag{3.11}$$

These frequencies are called the Matsubara frequencies, named after T. Matsubara who first introduced them in the imaginary time quantum theory formalism [121].

3.3. Dimensional Compactification

As the first step to the finite-temperature quantum field theory, the grand canonical partition function should be calculated. The Euclidean Lagrangian density $\mathcal{L}_E$ is the same as

the one defined in the Minkowski space $\mathcal{L}(x;\psi,A,\gamma)$ except for the change in the fourth component of the four-vectors as[1]

$$x^4 \to ix^0, \quad A^4 \to iA^0, \quad \gamma^4 \to i\gamma^0. \tag{3.12}$$

Moreover, from the Euclidean Lagrangian one can define the canonical momenta

$$\Pi_{A^\mu} = \frac{\partial \mathcal{L}_E}{\partial(\partial A^\mu/\partial x^4)}, \qquad \Pi_\psi = \frac{\partial \mathcal{L}_E}{\partial(\partial\psi/\partial x^4)} \tag{3.13}$$

leading to the definition of the Hamiltonian density

$$\mathcal{H} = \Pi_{A^\mu}\frac{\partial A^\mu}{\partial x^4} + \Pi_\psi \frac{\partial \psi}{\partial x^4} - \mathcal{L}_E \tag{3.14}$$

where

$$H = \int dx^1 dx^2 dx^3 \mathcal{H} \tag{3.15}$$

is the Hamiltonian independent of x^4.

The partition function has the form

$$\mathcal{Z}(\beta,\mu) = \int_{x^4-b.c.} \mathcal{D}(\psi,A) \exp\left\{ - S_E[\psi,A] - i\mu \int_{-\beta/2}^{\beta/2} dx^4 \int d^3x \bar{\psi}(x)\gamma^4\psi(x)\right\} \tag{3.16}$$

where S_E is the Euclidean action as the imaginary time action [127, 128]

$$S_E[\psi,A] = \int_{-\beta/2}^{\beta/2} dx^4 \int d^3x \mathcal{L}_E(x;\psi,A,\gamma). \tag{3.17}$$

Moreover, the integration in (3.16) is defined over a temporal constraint implying whether one deals with bosonic or fermionic fields

$$\begin{aligned} \psi(\boldsymbol{x}, x^4 = \beta/2) &= -\psi(\boldsymbol{x}, x^4 = -\beta/2) \\ A^\mu(\boldsymbol{x}, x^4 = \beta/2) &= A^\mu(\boldsymbol{x}, x^4 = -\beta/2). \end{aligned} \tag{3.18}$$

After performing a particular change of variables as [68]

$$\begin{gathered} z^1 = x^2, \quad z^2 = x^3, \quad z^3 = x^4, \quad z^4 = x^1 \\ C^1(z) = A^2(x), \quad C^2(z) = A^3(x), \quad C^3(z) = A^4(x), \quad C^4(z) = A^1(x) \\ \Gamma^1 = \gamma^2, \quad \Gamma^2 = \gamma^3, \quad \Gamma^3 = \gamma^4, \quad \Gamma^4 = \gamma^1 \end{gathered} \tag{3.19}$$

where the new Dirac matrices Γ^μ satisfy the same Clifford algebra as for γ^μ and by changing fermionic fields as

$$\chi(z) = \psi(x) \tag{3.20}$$

equation (3.16) changes the form to

$$\mathcal{Z}(\beta,\mu) = \int_{z^3-b.c.} \mathcal{D}(\chi,C) \exp\left\{ - S_E[\chi,C] - i\mu \int_{-\beta/2}^{\beta/2} dz^4 \int d^3z \bar{\chi}(z)\Gamma^3\chi(z)\right\}. \tag{3.21}$$

In the integral above the integration measure is defined over the compactified manifold $\mathbb{R}^2 \times S^1(\beta)$

$$\int_\beta dz := \int d^2z_\perp \int_{-\beta/2}^{\beta/2} dz^3 \tag{3.22}$$

[1] γ^μ are the matrices of the Clifford algebra for the quarks.

with $z_\perp = (z_1, z_2)$ where the "$\perp$" sign refers to the fact that the compactified dimension z^3 is orthogonal to the two other spatial dimensions. Moreover, here the integration measure goes over the periodic fields for the bosons and anti-periodic fields for the fermions both with respect to z_3 which is implied in integral (3.21)

$$\begin{aligned}\chi(z_\perp, \beta/2, z^4) &= -\chi(z_\perp, -\beta/2, z^4)\\ C(z_\perp, \beta/2, z^4) &= C(z_\perp, -\beta/2, z^4).\end{aligned} \tag{3.23}$$

Finally, by the definition of the spatial coordinates (i.e. z), one reaches to a modified compactified representation for the equation (3.5)

$$\mathcal{Z}(\beta, \mu) = \lim_{l\to\infty} \mathrm{Tr}\left[e^{-l\tilde{H}(\chi, C; \Gamma; \beta, \mu)}\right] \tag{3.24}$$

where $l \to \infty$ is the length of the uncompactified spatial dimensions and $\tilde{H}$ is a pseudo-Hamiltonian

$$\tilde{H}(\chi, C; \Gamma; \beta, \mu) \equiv H(\chi, C; \Gamma; \beta, \mu) + i\mu \int_\beta d^3z \chi^\dagger(x)\alpha_3\chi(x). \tag{3.25}$$

Here, $\alpha_3 = \Gamma^0\Gamma^3$ and $H(\chi, C; \Gamma; \beta, \mu)$ is the Weyl-gauge Hamiltonian in the Minkowski space defined on the compactified manifold $\mathbb{R}^2 \times S^1(\beta)$ and it satisfies the boundary conditions (3.23) [68].

The condition $l \to \infty$ leads to the calculation of the vacuum energy $\tilde{E}_0(\beta, \mu)$ defined by the Hamiltonian (3.25) as

$$\mathcal{Z}(\beta, \mu) = \lim_{l\to\infty} e^{-l\tilde{E}_0(\beta,\mu)} \tag{3.26}$$

which means solving Schrödinger equation for the vacuum wave functional on the spatial manifold $\mathbb{R}^2 \times S^1(\beta)$

$$\tilde{H}(\beta, \mu)\Psi(\chi, C) = \tilde{E}_0(\beta, \mu)\Psi(\chi, C). \tag{3.27}$$

That means finite-temperature quantum mechanics can be treated as in the zero temperature case just by compactification of one spatial dimension and solving the Schrödinger equation for the vacuum sector from which the whole behavior of quantum field theory in finite temperature can be analyzed. In particular, this avoids the computation of the complete spectrum as required e.g. in the grand canonical approach with a traditional density matrix.

In order to show the differences after spatial compactification one can compare the standard formulas of the grand canonical ensemble approach with the new approach. Considering standard definition (3.1) for the partition function, the pressure P and the energy ε have the form

$$\begin{aligned}P &= \frac{\ln \mathcal{Z}(\beta, \mu)}{\beta V},\\ \varepsilon &= \frac{1}{V}\left(-\frac{\partial \ln \mathcal{Z}}{\partial \beta} + \frac{\mu}{\beta}\frac{\partial \ln \mathcal{Z}}{\partial \mu}\right).\end{aligned} \tag{3.28}$$

However, the reformulated version of the partition function (3.26) leads to [68]

$$\begin{aligned}P &= -e\\ \varepsilon &= \frac{\partial}{\partial \beta}(\beta e) - \mu\frac{\partial e}{\partial \mu},\end{aligned} \tag{3.29}$$

where e is the vacuum energy density (pseudo-energy) on $\mathbb{R}^2 \times S^1(\beta)$ related to the vacuum energy by

$$\tilde{E}_0(\beta, \mu) = l^2 \beta e. \tag{3.30}$$

The represented approach can be tested by applying it to free relativistic fields, where as it has been illustrated in [68] it reproduces the correct result obtained from the grand canonical ensemble.

3.4. Treatment of the Adler-Davis model at Finite Temperature

In chapter 2, we solved the the gap equation (2.126) for the Adler-Davis model, where we discarded the explicit coupling of the transverse gluons to the quarks within our variational kernel. As a first step to explore the QCD phase diagram, we are interested to solve the same equation again but at finite temperature. The latter means that we should apply the method explained in section 3.3, where the temperature enters the theory via dimensional compactification. To be more precise, this means that in the heat bath the momentum arguments should change as

$$\boldsymbol{p} \to (\boldsymbol{p}_\perp, \Omega_n) \tag{3.31}$$

where $\boldsymbol{p}_\perp = p_1 \hat{\boldsymbol{e}}_1 + p_2 \hat{\boldsymbol{e}}_2$ is the planar non-compactified momentum vector perpendicular to the heat bath and Ω_n is the fermionic Matsubara frequency for vanishing chemical potential (see equation (3.11)). As we will see below, this seemingly harmless replacement will make a huge difference for the solution of the gap equation. In order to start deriving the gap equation at finite-temperature, let us recall equation (2.124) in the compactified form

$$\begin{aligned}\sqrt{p_\perp^2 + \Omega_m^2}\; s(\boldsymbol{p}_\perp, \Omega_m) = \frac{C_F}{2} \int_\beta đ^3 q \frac{F(\boldsymbol{q}_\perp - \boldsymbol{p}_\perp + (\Omega_n - \Omega_m)\hat{\boldsymbol{e}}_3)}{1 + s^2(\boldsymbol{q}_\perp, \Omega_n)} \\ \times \left[s(\boldsymbol{q}_\perp, \Omega_n)\Big(1 - s^2(\boldsymbol{p}_\perp, \Omega_m)\Big) - s(\boldsymbol{p}_\perp, \Omega_m)\Big(1 - s^2(\boldsymbol{q}_\perp, \Omega_n)\Big) \frac{\boldsymbol{q}_\perp + \Omega_n \hat{\boldsymbol{e}}_3}{\sqrt{q_\perp^2 + \Omega_n^2}} \cdot \frac{\boldsymbol{p}_\perp + \Omega_m \hat{\boldsymbol{e}}_3}{\sqrt{p_\perp^2 + \Omega_m^2}} \right]\end{aligned} \tag{3.32}$$

where in the new notation $q_\perp = |\boldsymbol{q}_\perp|$ and

$$\int_\beta đ^3 q = \frac{1}{\beta} \sum_{m=-\infty}^{\infty} \int đ^2 q_\perp. \tag{3.33}$$

As we see in above equation, compactification of the dimension changed not only the definitions for the momentum $\boldsymbol{p}$ but also the scalar kernel now depends on two variables, $s(\boldsymbol{p}_\perp, \Omega_m)$. The latter also results in the change of the form of the mass function (2.125)

$$M(\boldsymbol{p}_\perp, \Omega_m) = \frac{2\sqrt{p_\perp^2 + \Omega_m^2}\; s(\boldsymbol{p}_\perp, \Omega_m)}{1 + s^2(\boldsymbol{p}_\perp, \Omega_m)} \tag{3.34}$$

and the transformation of (3.32) to

$$M(\boldsymbol{p}_\perp, \Omega_m) = \frac{C_F}{2} \int_\beta đ^3 q F(\boldsymbol{q}_\perp - \boldsymbol{p}_\perp + (\Omega_n - \Omega_m)\hat{\boldsymbol{e}}_z) \frac{M(\boldsymbol{q}_\perp, \Omega_n) - M(\boldsymbol{p}_\perp, \Omega_m) \frac{\boldsymbol{p}_\perp \cdot \boldsymbol{q}_\perp + \Omega_n \Omega_m}{p_\perp^2 + \Omega_m^2}}{\sqrt{q_\perp^2 + \Omega_n^2 + M^2(\boldsymbol{q}_\perp, \Omega_n)}} \tag{3.35}$$

where the Coulomb kernel is given in (2.128).

Equation (3.35) is the finite-temperature form of the gap equation (2.129). Here, also for the finite-temperature case, we follow the same goal: we look for a non-trivial answer for the gap equation as a sign of chiral symmetry breaking and calculate the chiral quark condensate as its order parameter. For that matter, we need to solve equation (3.35) numerically, however, the equation is not suitable yet for numerical calculations. One possible algorithm would be to follow the procedure which we did for the zero-temperature case in chapter 3 which means preparing the equation by shifting the loop momentum and then iterating the coupled system of integral equations for all Matsubara modes simultaneously. However, this method does not work well for equation (3.35) because of two reasons. First, the numerical effect scales quadratically with the number of Matsubara frequencies included in the m sum in the right hand-side of equation (3.35), and up to 60...80 frequencies are necessary to reach to the phase transition region. This calculations at even lower temperatures require an enormous numerical effort. Second and more importantly, the Matsubara sum over m is dominated by the single index $m = n$ where external and loop frequencies match. In this case, however, the Coulomb kernel has a strong infrared singularity which must be regulated, and the resulting mass function and condensate show a strong dependence on the regulator, especially at small temperatures where a large number of frequencies must be summed. We therefore follow a different approach and first Poisson resum the Matsubara frequencies in equation (3.35), which means we use the general formula [68]

$$\int_\beta đ^3p f(\boldsymbol{p}) = \int đ^3p f(\boldsymbol{p}) \sum_{k=-\infty}^{+\infty} (-1)^{n_F k} e^{ik\beta p_z}. \tag{3.36}$$

Using equation (3.36) and shifting the loop momentum, as we did in 2.5.4, in the compact notation equation (3.35) casts to

$$M(\boldsymbol{p}) = 4\pi \sum_{m=-\infty}^{+\infty} (-1)^m \int đ^3q \cos(m\beta(q_z + p_z)) F(|\boldsymbol{q}|) \frac{M(\boldsymbol{p}+\boldsymbol{q}) - (1 + \frac{\boldsymbol{p}\cdot\boldsymbol{q}}{\boldsymbol{p}^2}) M(\boldsymbol{p})}{\sqrt{(\boldsymbol{p}+\boldsymbol{q})^2 + M^2(\boldsymbol{p}+\boldsymbol{q})}} \tag{3.37}$$

where as it can be seen, the $m = 0$ contribution of the sum corresponds to the zero-temperature gap equation (compare with (2.131)). At last we reintroduce the chiral quark condensate (2.123) for the finite-temperature case, which after Poisson summation can be written in compact notation as

$$\rho = -2N_c \sum_{m=-\infty}^{+\infty} (-1)^m \int đ^3p \cos(m\beta p_z) \frac{M(\boldsymbol{p})}{\sqrt{\boldsymbol{p}^2 + M^2(\boldsymbol{p})}} \tag{3.38}$$

where again by fixing $m = 0$ one can see that we derive the zero-temperature formula (i.e. (2.123)).

3.4.1. Numerical Treatment

As it was mentioned, the numerical treatment of equation (3.35) follows a different procedure in comparison with the zero-temperature case. As we saw in chapter 2, in order to solve the gap equation in Adler-Davis model at zero temperature we used the non-ratio form for equation (2.129) despite the advantage of the ratio form in giving us the possibility to use bigger steps in the updating procedure. There, we argued that writing the gap equation in the ratio form (i.e. (2.132)) is a bad idea since in that form we divide two infrared divergence integrals to each other. However, if one introduces a lower cutoff like

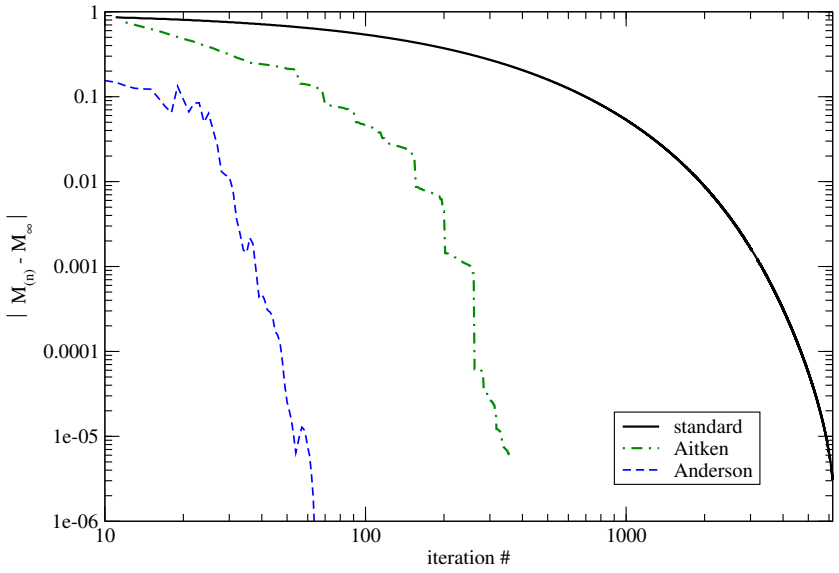

Figure 3.2.: The pattern of iteration for standard and accelerated methods. In this plot $|M_n - M_\infty|$ refers to the distance between the result at nth iteration to the final solution.

μ as the IR regulator for equation (2.132), in the limit $\mu \to 0$ the right hand-side of the equation reads

$$M(p) + \mu\left[\frac{2}{\pi}\frac{M(p)}{\sqrt{p^2 + M^2(p)}} + \text{non-local}\right] + \mathcal{O}(\mu^2). \tag{3.39}$$

Thus iterating equation (2.132) only produces changes for the mass function of the order μ for a finite infrared cutoff i.e. it automatically underrelaxes the iteration for greater stability. Furthermore, we know from the calculations in chapter 2 that there the equation (2.129) was not a stable form of integral equation where in the IR limit the changes were order of $\mathcal{O}(1)$ and we needed to underrelax the iteration process. However, equation (2.132) can be overrelaxed without loosing any stability and that is the advantage of its ratio form. Thus if one takes care of the infrared divergences, it is possible to use the ratio form (2.132) for the calculation of the mass function in the case of Adler-Davis model. Comparing the zero- and finite-temperature cases, in the zero-temperature case the advantage of writing the gap equation in the ratio form was just less number of iterations, however, in the finite-temperature case the importance of writing the equation in this form lies more in the stability of the answer. Despite reduction of the iterating steps for the gap equation in the ratio form, it still requires a large number for convergence, which becomes even more of a problem in the finite temperature case where each iteration is much more expensive.

Apart from preferring the ratio-formed gap equation, the time consuming iterative process led us to try new algorithms. One of the ways to deal with the expensive iteration procedure is to update equations in a different form and that is where we tested the accelerated methods such as the Aitken's Δ^2 process as one of the possibilities for updating the mass function (see appendix B). Although this method does not follow a smooth pattern of convergence as it is shown in figure 3.2 in comparison with the one we used in the chapter 2, it is exceedingly fast which brings the number of iterations from 7000 to around 400. However, these iteration numbers are obtained for the relative error 10^{-6} (see appendix B). This means that for more accuracy, one needs higher number of iterations. In

order to make the iteration procedure even faster, we use Anderson's acceleration method for $k = 18$ (see appendix B). The advantage of using this method is more accuracy for less iterations, where for the limit of 10^{-9} for the relative error one just needs around 70 iterations which is a very small number compared to the one needed for the standard iteration method.

Solution

In order to solve equation (3.35), one can introduce the polar coordinates: $\boldsymbol{p} = (p_z, p_\perp, \phi_p)$, $\boldsymbol{q} = (q_z, q_\perp, \phi_q)$. Here, as it can be seen the angles $\phi_{p,q}$ appear for both external and loop momenta, where due to the $O(2)$ symmetry of rotations around z axis, one can set ϕ_p to zero while the loop azimuthal angle ϕ_q just appears in the scalar product through its cosine

$$\boldsymbol{p} \cdot \boldsymbol{q} = p_z q_z + p_\perp q_\perp \cos(\phi_q). \tag{3.40}$$

Moreover, here the component of the momentum is in the direction of the heat bath considered positive in our calculations which is due to the symmetry $M(p_z, p_\perp) = M(-p_z, p_\perp)$. However, the polar coordinate system does not seem to be a good choice since in this coordinates the mass function M depends on two non-compact variables p_z and $p_\perp$. This dependence makes the numerical calculations complicated, thus we stick to the spherical coordinates, where numerical calculations should behave better. Moving to the spherical coordinates one can redefine the coordinates as $\boldsymbol{p} = (p_z, \xi_p, \gamma_p)$ and $\boldsymbol{q} = (q_z, \xi_q, \gamma_q)$, where for the external momentum $\boldsymbol{p}$ in the new coordinates the azimuthal angle is set to zero (i.e. $\phi_p = 0$). Therefore, the only remaining angular part is the polar angle θ_p which enters to the calculations via its cosine

$$\xi_p = \frac{p_z}{p} = \cos\theta_p \in [0, 1]. \tag{3.41}$$

For the loop momentum $\boldsymbol{q}$ we should keep the azimuthal angle as $\gamma_q = \cos\phi_q \in [-1, 1]$. Moreover, here also the ξ_q component which takes the place of the non-compactified component is defined as

$$\xi_q = \frac{|q_z|}{q} = \cos\theta_q \in [-1, 1]. \tag{3.42}$$

Writing equation (3.40) via the angles, we have [122]

$$\boldsymbol{p} \cdot \boldsymbol{q} = |\boldsymbol{p}||\boldsymbol{q}| \Big[\cos\theta_p \cos\theta_q + \cos\phi_q \sqrt{1 - \cos^2\theta_q} \sqrt{1 - \cos^2\theta_p} \Big] \tag{3.43}$$

which after introducing the abbreviation $\eta \equiv \gamma_q \sqrt{(1 - \xi_p^2)(1 - \xi_q^2)}$ takes the from

$$\boldsymbol{p} \cdot \boldsymbol{q} = |\boldsymbol{p}||\boldsymbol{q}| \Big[\xi_p \xi_q + \eta \Big]. \tag{3.44}$$

Equation (3.37) in above coordinates has the ratio form

$$M(p, \xi_p) = \frac{U(p, \xi_p)}{1 + W(p, \xi_p)} \tag{3.45}$$

where

$$U(p,\xi_p) = \frac{1}{\pi^2}\sum_{m=-\infty}^{\infty}(-1)^m\int_{-1}^{1}d\xi_q\int_0^{\infty}dq\ q^2F(q)\cos\left[m\beta(p\xi_p+q\xi_q)\right] \times\int_{-1}^{1}\frac{d\gamma_q}{\sqrt{1-\gamma_q^2}}\frac{M(Q,\xi_Q)}{\sqrt{Q^2+M^2(Q,\xi_Q)}}$$
$$W(p,\xi_p) = \frac{1}{\pi^2}\sum_{m=-\infty}^{\infty}(-1)^m\int_{-1}^{1}d\xi_q\int_0^{\infty}dq\ q^2F(q)\cos\left[m\beta(p\xi_p+q\xi_q)\right] \times\int_{-1}^{1}\frac{d\gamma_q}{\sqrt{1-\gamma_q^2}}\frac{1+q/p(\xi_q\xi_p+\eta)}{\sqrt{Q^2+M^2(Q,\xi_Q)}}. \tag{3.46}$$

Here, we have for the shifted momentum

$$Q=\sqrt{q^2+p^2+2pq(\xi_q\xi_p+\eta)}, \qquad \xi_Q=\frac{p\xi_p+q\xi_q}{Q} \tag{3.47}$$

where for the simplification of the notation we write $|\boldsymbol{p}|=p$ and $|\boldsymbol{q}|=q$.

Equation (3.45) is still not ready for numerical investigations. One problem for solving this equation is the divergences arising in the IR region for the Coulomb kernel, which also leads to the slow convergence of the Poisson series. In order to take care of this problem, one can introduce a subtraction method in which we subtract the infrared part of the function from the integrand and then add it back. This method has the advantage that the problematic part can be done analytically which makes the whole calculation faster. By using this method we can evaluate the integration at the limit of $q=0$, which means there is no need to introduce a IR cutoff for our integrals as what we did in chapter 2. However, we will still employ a small IR regulator of the order 0.5 MeV in the Coulomb potential in order to accelerate the calculation. Subtracted integrands in the numerator and denominator of equation (3.45) read

$$u(q,\xi_q,\gamma_q;p,\xi_p) = \frac{M(Q,\xi_Q)}{\sqrt{Q^2+M^2(Q,\xi_Q)}} - \Delta u(q,\xi_q,\gamma_q;p,\xi_p)$$
$$v(q,\xi_q,\gamma_q;p,\xi_p) = \frac{1+q/p(\xi_p\xi_q+\eta)}{\sqrt{Q^2+M^2(Q,\xi_Q)}} - \Delta v(q,\xi_q,\gamma_q;p,\xi_p) \tag{3.48}$$

where

$$\Delta u(q,\xi_q,\gamma_q;p,\xi_p) = \frac{M(p,\xi_p)}{\sqrt{p^2+M^2(p,\xi_p)}}$$
$$\Delta v(q,\xi_q,\gamma_q;p,\xi_p) = \frac{1}{\sqrt{p^2+M^2(p,\xi_p)}}. \tag{3.49}$$

Introducing the subtraction method, equation (3.45) changes it form to

$$M(p,\xi_p) = \frac{g(p,\xi_p)+\mathcal{U}(p,\xi_p)}{h(p,\xi_p)+\mathcal{W}(p,\xi_p)} \tag{3.50}$$

where

$$\mathcal{U}(p,\xi_p) = \frac{1}{\pi^2}\sum_{m=-\infty}^{\infty}(-1)^m\int_{-1}^{1}d\xi_q\int_0^{\infty}dq\ q^2F(q)\cos\left[m\beta(p\xi_p+q\xi_q)\right] \times\int_{-1}^{1}\frac{d\gamma_q}{\sqrt{1-\gamma_q^2}}u(q,\xi_q,\gamma_q;p,\xi_p)$$
$$\mathcal{W}(p,\xi_p) = \frac{1}{\pi^2}\sum_{m=-\infty}^{\infty}(-1)^m\int_{-1}^{1}d\xi_q\int_0^{\infty}dq\ q^2F(q)\cos\left[m\beta(p\xi_p+q\xi_q)\right] \times\int_{-1}^{1}\frac{d\gamma_q}{\sqrt{1-\gamma_q^2}}v(q,\xi_q,\gamma_q;p,\xi_p) \tag{3.51}$$

are the integrals with subtracted integrands and

$$g(p,\xi_p) = \frac{1}{\pi^2}\sum_{m=-\infty}^{\infty}(-1)^m\int_{-1}^{1}d\xi_q\int_0^{\infty}dq\ q^2F(q)\cos\left[m\beta(p\xi_p+q\xi_q)\right] \times\int_{-1}^{1}\frac{d\gamma_q}{\sqrt{1-\gamma_q^2}}\Delta u(q,\xi_q,\gamma_q;p,\xi_p)$$
$$h(p,\xi_p) = 1+\frac{1}{\pi^2}\sum_{m=-\infty}^{\infty}(-1)^m\int_{-1}^{1}d\xi_q\int_0^{\infty}dq\ q^2F(q)\cos\left[m\beta(p\xi_p+q\xi_q)\right] \times\int_{-1}^{1}\frac{d\gamma_q}{\sqrt{1-\gamma_q^2}}\Delta v(q,\xi_q,\gamma_q;p,\xi_p) \tag{3.52}$$

are the integrals carrying the added integrand parts.

In order to profit from using the subtraction method, we should be able to solve the integrals in (3.52) analytically. Indeed, after introducing the regulator $\mu \approx 0.1...1$ MeV for the Coulomb potential $F(q)$, as explained above, one can obtain [122]

$$g(p,\xi_p) = \frac{M(p,\xi_p)}{\sqrt{p^2+M^2(p,\xi_p)}}\sum_{m=-\infty}^{\infty}(-1)^m\frac{\cos(\beta mp\xi_p)}{2\mu}e^{-m\beta\mu} = \frac{M(p,\xi_p)}{\sqrt{p^2+M^2(p,\xi_p)}}\cdot\frac{1}{2\mu}\frac{\sinh(\beta\mu)}{\cosh(\beta\mu)+\cos(\beta p\xi_p)}. \tag{3.53}$$

The result for $h(p,\xi_p)$ is the same as formula above except the mass function which does not appear in the numerator (i.e. $h(p,\xi_p) = g(p,\xi_p)/M(p,\xi_p)$). What can be seen here is that at zero temperature limit where the dominant frequency in the Poisson-sum is the zeroth one (i.e. $m = 0$) the formula diverges since it has the form $1/2\mu$, however, including more terms in the summation takes care of this divergency.

Results

In our approach for investigating equation (3.50) as the equation we want to solve, we analyze each integrand separately. In this study we replace the mass function with its zero-temperature form for simplicity. We fix the value of the external momentum to a typical value $p = 200$ MeV and the cosine on $\xi_p = 0.5$ as the region where the mass function has its main structure. Moreover, we use Anderson's method (see appendix B) as the sequence accelerator, since it has been very successful in the zero-temperature case

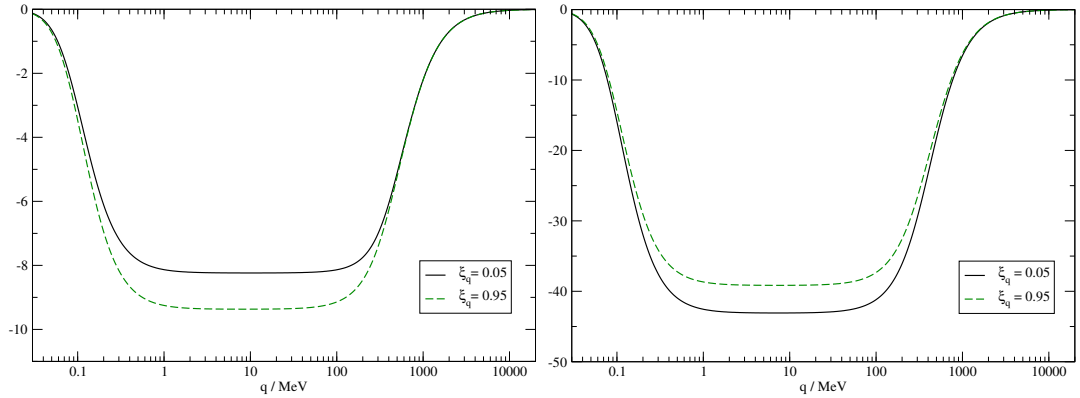

Figure 3.3.: The behavior of the momentum integrand without cosine function (i.e. equation (3.55)). Left: the numerator and Right: the denominator of the gap equation plotted for the values $\xi_q = 0.05$ and $\xi_q = 0.95$ for the fixed values $p = 200$ MeV and $\xi_p = 0.5$ for the external momentum.

(see figure 3.2). Additionally, in order to deal with the integrals over ξ_q we symmetrize the integrand which means

$$\int_{-1}^{1} d\xi_q f(\xi_q) \to \int_{0}^{1} d\xi_q \sum_{\pm} f(\pm\xi_q). \tag{3.54}$$

In order to start the investigation of the integrands, let us recall the loop momentum integrand in equation (3.50) without cosine part

$$f(q) = q^2 F(q) \int_{-1}^{1} \frac{d\gamma}{\sqrt{1-\gamma^2}} \sum_{\pm} u(q, \pm\xi_q, \gamma_q; p, \xi_p) \tag{3.55}$$

which can be done numerically by means of the Gauss-Chebychev integration method (see appendix B). The behavior of the above function is shown in figure 3.3 for both numerator and denominator in the gap equation (3.50). As we can see, the integrand goes to zero as $q \to \infty$. Moreover, it goes to a constant at $q \to 0$ as expected due to the subtraction, before it eventually decays to zero at $q << \mu$ due to IR regulator.

The next integral which we investigate is the integration by including the cosine part to above equation

$$q^2 F(q) \cos\left[m\beta(p\xi_p + q\xi_q)\right] \int_{-1}^{1} \frac{d\gamma}{\sqrt{1-\gamma^2}} \sum_{\pm} u(q, \pm\xi_q, \gamma_q; p, \xi_p). \tag{3.56}$$

As it can be observed in figure 3.4, the integrand oscillates wildly, in particular for large indices $m >> 1$. In order to deal with this integral numerically, one generally requires many sampling points and this is hence the most expensive part of the calculation. Thus, we employ the standard Fourier integrals form [129] or alternatively a double exponential algorithm [130]. The remaining ξ_q integral in equation (3.50) has its main support for small ξ_q (see the left panel in figure 3.5). To obtain a more uniform integrand which can be better sampled by Gauss-Legendre integration, we employ the change of variables

$$\int_0^1 d\xi_q f(\xi_q) = \int_0^1 dt\ nt^{n-1} f(t^n) \equiv \int_0^a dt \bar{f}(t). \tag{3.57}$$

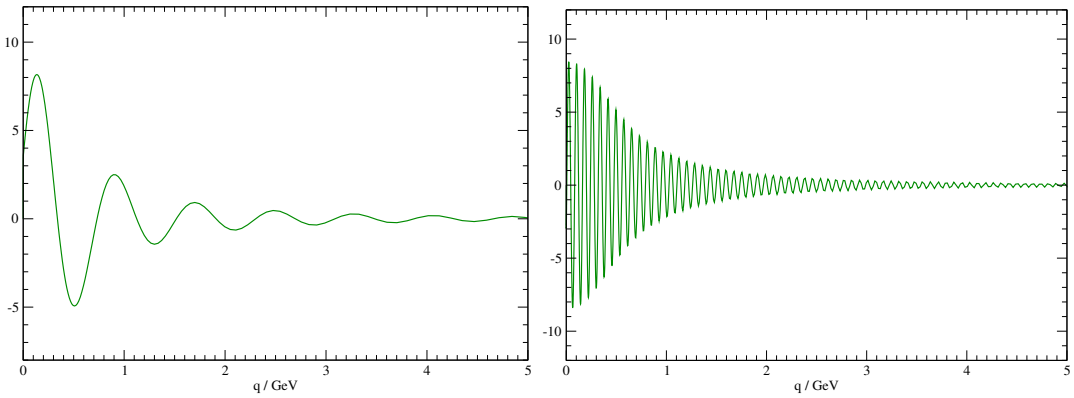

Figure 3.4.: The behavior of the full momentum integrand in the gap equation (3.50) for the temperature $T = 50$ MeV for Poisson indices $m = 1$ (left) and $m = 10$ (right).

Typically, this transformation reduces the number of sampling points for a decent accuracy from 1200 down to around 30.

As the last issue for solving the integrals in equation (3.50), one can also include the Poisson summations, which are even in m. This means that the sums can be evaluated in the form

$$\sum_{m=-\infty}^{\infty} a_m = \sum_{m=0}^{\infty} (2 - \delta_{m0}) a_m \equiv \sum_{m=0}^{\infty} b_m.$$

The partial summations in the gap equation (3.50) are shown in figure 3.6. As it can be seen, the Poisson sums converge slowly, with oscillations in the partial sums that become more pronounced at higher temperatures. This is expected, as the Poisson sum converges slower at higher temperatures, though the $m = 0$ term dominates even at larger T. An accurate evaluation of the Poisson sum requires several hundreds of terms included in the sum; this can, however, be accelerated fairly well by using the ϵ-algorithm [131] due to the oscillating behavior of the sum. In most cases, we find that including about 40 terms in the Poisson sum is sufficient to predict the limit with good precession (see figure 3.6).

The left panel in figure 3.7 shows the mass function for $M(p, \xi_p)$ for different directions of $\boldsymbol{p}$ relative to the heat bath (i.e. different values of ξ_p). The fact that the different functions $M(p, \xi_p)$ differ for different directions ξ_p shows that the $O(3)$ symmetry is broken at $T > 0$.

Let us check that this $O(3)$ symmetry is restored as $T \to 0$. Analytically, it is easy to see that equation (3.50) agrees with the $T = 0$ gap equation if (i) we only include the $m = 0$ term in the Poisson sum such all other terms oscillate to zero at $\beta \to 0$ and (ii) $\xi_p = 1$, i.e. we put the external momentum in the direction of the heat bath. In the right panel of figure 3.7, we have also studied the limit $T \to 0$ numerically. As it can be seen, we have to go to the fairly low temperatures $T < 1$ MeV to reproduce the mass function numerically. At the low temperature, all mass functions for different directions of ξ_p actually fall on top of each other and we have only plotted the one for $\xi_p = 1$. The fact that $M(p, \xi_p)$ becomes substantially smaller than the $T = 0$ limit even for small temperatures does not mean that the same happens for the condensate. As it can be seen in equation (3.38), the integrand for the condensate becomes essentially independent of M for small p (i.e. the behavior of $M(p, \xi_p)$ for small p is more or less irrelevant for the condensate). This means that ρ stays constant at its $T = 0$ value up to fairly large temperatures, even though the mass function is already suppressed constantly at this point. For this reason, $M(0)$ is not a good order parameter for the chiral phase transition in addition to the fact that it is

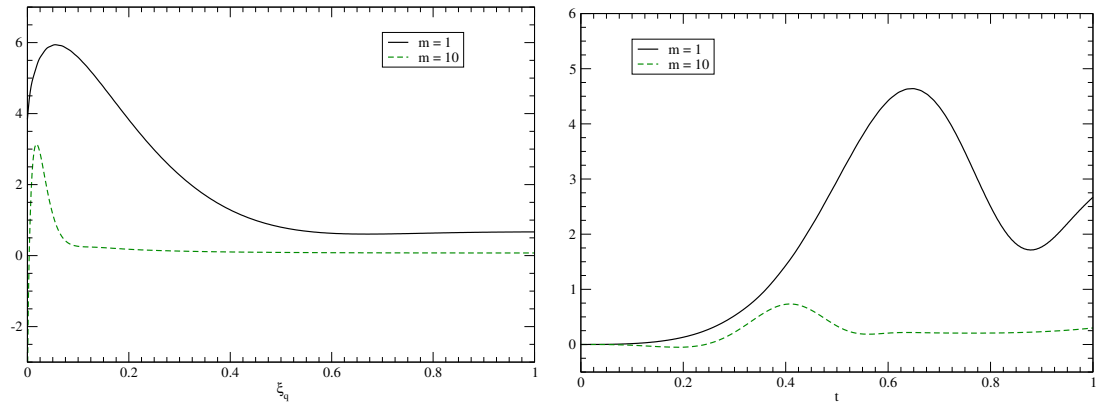

Figure 3.5.: Left: The behavior of ξ_q dependent integrand in the gap equation (3.50) at temperature $T = 50$ MeV for two Poisson indices $m = 1$ and $m = 10$. Right: the same function after substitution of the low ξ_q-behavior with $\xi_q = t^4$.

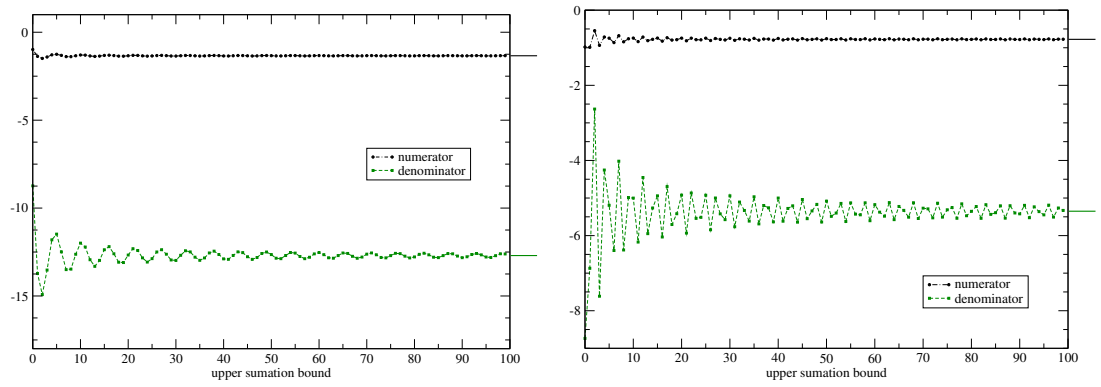

Figure 3.6.: Partial sums in the numerator and denominator of the gap equation (3.50) as the function of upper summation bound for the temperatures $T = 50$ MeV (left) and $T = 150$ MeV (right), plotted for $p = 200$ MeV and $\xi_p = 0.5$. The straight lines at the right limit are the predictions of ϵ-algorithm.

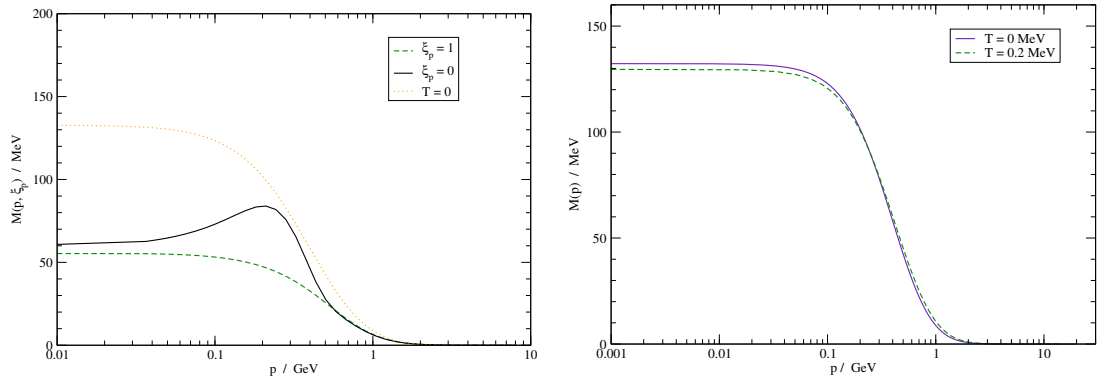

Figure 3.7.: Left: The mass function plotted for two values of ξ_p at $T = 80$ MeV compared to the one at $T = 0$. Right: Mass function $M(p, \xi_p = 1)$ for small temperatures compared to $T = 0$ one.

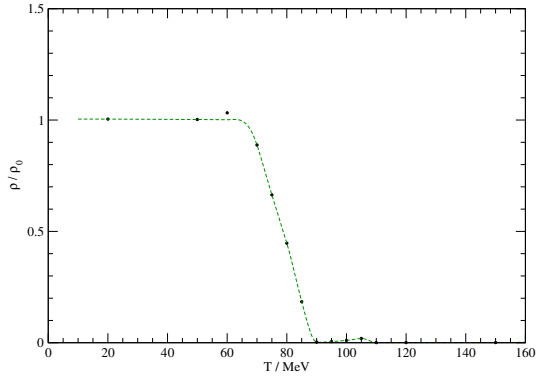

Figure 3.8.: The chiral quark-condensate at finite temperature ρ divided to its value at zero temperature as function of temperature.

gauge dependent in the first place.

The calculated values of quark condensate for different temperatures are shown in figure 3.8. Here, one of the important points for us is finding the zero-temperature value (i.e. $\rho = (-185\text{MeV})^3$) for the condensate at small temperatures, which is recovered in our calculations. Furthermore, our data for different temperatures indicates a second order phase transition at around $T^* \approx 90$ MeV. This result is somehow in the middle between the calculations of reference [132] (in the canonical approach using a quasi-particle ansatz for the density matrix) which gave $T^* \approx 64$ MeV, and lattice calculations using 2+1 flavors of staggered fermions[2] which predict $T^* \approx 155$ MeV [133]. The mismatch of our simple model with lattice calculations can be cured in several ways. First, we have neglected the coupling between quarks and gluons in our variational kernel, which is expected to increase the strength of the chiral symmetry breaking (see chapter 2). As a consequence, the $T = 0$ value for the chiral condensate $\rho = (-185\text{MeV})^3$ was already much smaller than the value obtained in lattice calculations. If we want to adjust the overall scale in our calculations such as to reproduce the phenomenological value of the quark condensate $\rho = (-236\text{MeV})^3$, we must increase the Coulomb string tension to $\sigma_C/\sigma \approx 4.2$ which is at the border of the range supported by lattice. In this case, the critical temperature also increases to $T^* \approx 115$ MeV which is still somewhat smaller than the full lattice result. It will be interesting for future investigations to see if improvements in the variational kernel along the lines of chapter 2 will be sufficient to overcome the discrepancy. However, calculation of the uncoupled equation (3.50) for each temperature already required more than 100 CPU hours and including the coupling between quarks and gluons increases this effort considerably.

[2] In the approximations made in our model, the critical temperature T^* does not depend on the number of quark flavors.

4. Graphene

In this section I will apply the variational Hamiltonian approach to a central topic in the current solid state physics, namely the electronic properties of graphene. This demonstrates the great versatility of variational Hamiltonian approach in a context where other methods were traditionally favored. Since the solid state background of graphene is not covered by particle physics introduced in chapter 1, I give a brief introduction into the physics of graphene in general before applying the variational Hamiltonian approach, where for the physics introduction I mainly follow the references [134, 135].

Introduction

Graphene is an atomic monolayer of carbon atoms condensed in a hexagonal (honeycomb) lattice. Even though its basic properties were known theoretically for a long time [136], general wisdom indicated that no 2D crystal could be stable at non-zero temperature. The experimental isolation and characterization of the material by K. Novoselov and A. Geim thus came as a big surprise which together with the extraordinary properties of the crystal and its potential technical applications led to the Nobel prize on 2010 for the "*groundbreaking experiments regarding the two dimensional material graphene*".

As a crystal, graphene has fascinating properties. For example, it features an enormous electron mobility where the electrons move ballistically all around the hexagonal lattice of carbon independent of the temperature. Also graphene is a very light material despite of being 200 times more sustainable than steel before breaking [137–139]. Moreover, it is the thinnest material possible to exist [140–142]. Electronically it is a zero-gap semiconductor or a semimetal in which one can observe the anomalous *quantum Hall effect* even at room temperature [143].

Despite all the unique properties of this material, the strongest motivation to study graphene theoretically comes from the fact that the charge carriers in graphene behave like massless Dirac fermions in the limit of small excitations, where the *Fermi velocity* v_F is around 1/300 of the speed of light. This implies that the effective description of electrons in graphene is in terms of QED_{2+1} with a fine structure constant of the order 1, which makes one able to observe some relativistic properties of QED such as *Zitterbewegung* or *chiral tunneling* and *Klein paradox* in graphene [144, 145]. Thus, graphene can play the role of experimental testing ground for QED in 2+1 dimensions in a semi relativistic manner.

In the following, I will first give a quick review over the basic theoretical and experimental aspects of graphene. I review the lattice structure of graphene and introduce the *Dirac points* on the honeycomb lattice. After introducing the *tight-binding* approach on graphene lattice, where we observe how the existence of the next nearest neighbors effects the symmetry on graphene lattice, the Dirac fermions are studied on the honeycomb lattice in a first quantized manner and the definition of *pseudo-spin* and chirality are introduced. The electron-electron interaction in graphene is reviewed where we end up with the expression of the chiral symmetry breaking.

Finally, by considering a 2+1 dimensional model in which only electrons interact with each other, I apply the variational Hamiltonian approach and find the solution for the gap

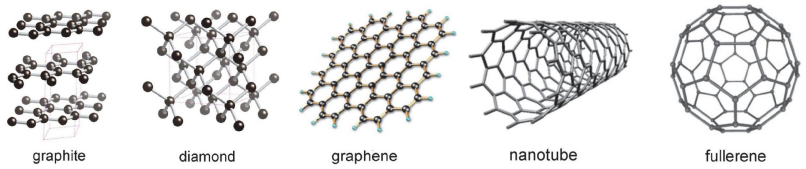

Figure 4.1.: The allotropes of carbon from left to right: 3D graphite and diamond, 2D graphene, 1D nanotubes, 0D fullerenes. The figure is adopted and reproduced with permission from [148].

equation as a result of broken chiral symmetry in graphene. The physical consequences of this result and future improvements of the approach are discussed in a summary.

4.1. Overview

Lattice Structure of Graphene

Graphene is a flat monolayer of carbon atoms tightly packed into a 2D honeycomb lattice [139]. It is the basic block for building other graphitic materials of other dimensions. It can be wrapped up into 0D *fullerenes* [146], rolled into 1D *nanotubes* [147] or stacked into 3D as graphite [139]. The carbon atoms on the graphene lattice have a σ bond formation which is due to the sp^2 hybridization. The robust structure of graphene that can be seen in different forms of allotropes is because of this σ band. However, the p_z orbital which is perpendicular to the 2D structure of the lattice can have covalent binding with other carbon atoms and form a half filled π band [134].

The interesting point about graphene is that until 70 years ago its existence was under question. Actually, it was first Landau and Peierls who argued that thermodynamically 2D lattices are unstable so they can not exist at non-zero temperature [149, 150]. Nonetheless, graphene was described theoretically by Wallace in 1947 as a starting point for understanding the electronic properties of 3D graphite [136].

The structure of graphene lattice can be understood as a triangular lattice with basis of two atoms per unit cell (see figure 4.2). The lattice vectors for the single layer graphene have the definition [134]

$$\boldsymbol{a}_1 = \frac{a}{2}(3, \sqrt{3}) \ , \ \boldsymbol{a}_2 = \frac{a}{2}(3, -\sqrt{3}) \tag{4.1}$$

where $a \approx 1.42$Å is the distance between carbon atoms. Furthermore, the *reciprocal* lattice vectors are

$$\boldsymbol{b}_1 = \frac{2\pi}{3a}(1, \sqrt{3}) \ , \ \boldsymbol{b}_2 = \frac{2\pi}{3a}(1, -\sqrt{3}). \tag{4.2}$$

Here, one can define the Dirac points $\boldsymbol{K}$ and $\boldsymbol{K'}$ at the corners of the Brillouin zone as (see figure 4.2)

$$\boldsymbol{K} = \Big(\frac{2\pi}{3a} \ , \ \frac{2\pi}{3\sqrt{3}a}\Big) \ , \ \boldsymbol{K}^{'} = \Big(\frac{2\pi}{3a}, -\frac{2\pi}{3\sqrt{3}a}\Big). \tag{4.3}$$

The Dirac points are important because they are the points where the valence and conducting bands in graphene meet each other. Here, basically each Dirac point plays the role

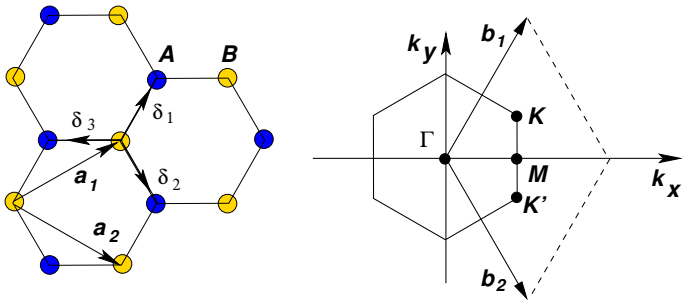

Figure 4.2.: Left: Overlap of two sublattices A and B. The triangular lattice is defined on the hexagonal graphene lattice, where $\boldsymbol{a}_1$ and $\boldsymbol{a}_2$ are the lattice unit vectors, and $\boldsymbol{\delta}_i$, $i = 1, 2, 3$ are the nearest neighbor vectors: $\boldsymbol{\delta}_1 = \frac{a}{2}(1, \sqrt{3})$, $\boldsymbol{\delta}_2 = \frac{a}{2}(1, -\sqrt{3})$, $\boldsymbol{\delta}_3 = -a(1, 0)$. Right: Top view of the Brillouin zone for graphene, where the Dirac cones are located at the $\boldsymbol{K}$ and $\boldsymbol{K'}$ points and Γ is the zero momentum point. The figures are adopted and reprinted with permission from [134].

of a Fermi surface in the solids, which separates two Dirac cones including electrons and holes. This is the feature which makes one to define graphene as zero-gap semiconductor at half filling limit.

Tight-Binding Model in Graphene

Carbon atom has 6 electrons, the first 2 electrons in the inner shell are strongly bond to the carbon nucleus in a $1s$ orbital. The remaining 4 electrons can either form sp^3 hybridization, as in diamond, or they can form sp^2 hybridization as in graphene case. This means that in graphene we have the planar triangular structure between carbon atoms, created by the σ bond between electrons. The strongness of the honeycomb lattice in graphene is because of the σ bond between electrons. Moreover, the remaining electron in $2p$ orbital which is perpendicular to the planar structure can overlap with the neighbor electrons and form a π bond. This bond is a loosely bond and it is responsible for the electronic conductivity of graphene. Its band structure is described by tight-binding Hamiltonian including only the first and second nearest neighbors on honeycomb lattice [134]

$$H = -t \sum_{\langle i,j \rangle \sigma} (a^\dagger_{\sigma,i} b_{\sigma,j} + H.c.) - t' \sum_{\langle\langle i,j \rangle\rangle \sigma} (a^\dagger_{\sigma,i} a_{\sigma,j} + b^\dagger_{\sigma,i} b_{\sigma,j} + H.c.). \tag{4.4}$$

Here, $a_{\sigma,i}$ and $a^\dagger_{\sigma,i}$ are the annihilation and creation operators for an electron with the spin index $\sigma \equiv (u, d)$ on the site $\mathbf{R}_i$ on the sublattice A. In the same manner $b_{\sigma,i}$ and $b^\dagger_{\sigma,i}$ are the annihilation and creation operators on the sublattice B. Furthermore, $t \approx$ 2.8 eV is the nearest neighbor hopping energy between different sublattices, and t' is the hopping energy[1] for the next nearest neighbors on the same sublattice.

One can derive the energy bands from Hamiltonian (4.4) for the quasi-free π electron in the form [136]

$$E_\pm(\boldsymbol{k}) = \pm t \sqrt{3 + f(\boldsymbol{k})} - t' f(\boldsymbol{k}) \tag{4.5}$$

[1]The value of the t' is between 0.02 t and 0.2 t depending on the tight-binding parametrization in which the third nearest neighbors hopping energy also play a role [151].

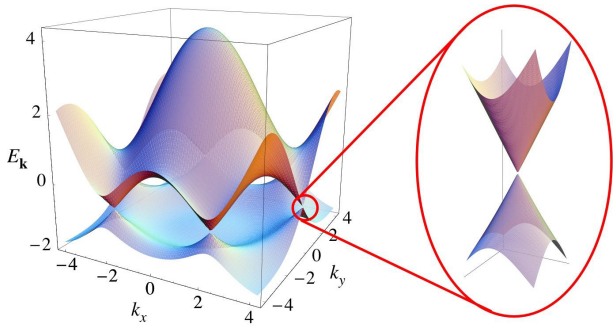

Figure 4.3.: Left: Energy spectrum, in the units of t for the values $t \approx 2.7$ eV and $t' = 0.2t$ and the Dirac point separating the upper and lower cones. The figure is adopted and reprinted with permission from [134].

where

$$f(\boldsymbol{k}) = 2\cos\left(\sqrt{3}k_y a\right) + 4\cos\left(\frac{\sqrt{3}}{2}k_y a\right)\cos\left(\frac{3}{2}k_x\right) \tag{4.6}$$

and the plus and minus signs refer to the upper and lower π bands. Here, including or not including the second nearest neighbors hopping energy (i.e. t') effects the symmetry of the spectrum. That means for $t' = 0$ the spectrum is symmetric. However, in case of $t' \neq 0$ the electron-hole symmetry gets broken and the π bands become asymmetric.

The Dirac points $\boldsymbol{K}$ and $\boldsymbol{K}'$ are the points at the Brillouin zone where the lower and upper π band touch each other. At zero temperature, the lower band is filled (valence band) and the upper π band is empty (conducting band), so that the Dirac points take the role of the Fermi level in conventional crystals. For small excitation energies, only the region close to the Dirac points is of interest. One can obtain the dispersion relation near the Dirac points ($\boldsymbol{K}$ or $\boldsymbol{K}'$) by the expansion of the full band structure (4.6). Replacing $\boldsymbol{k} = \boldsymbol{K} + \boldsymbol{q}$ with $|\boldsymbol{q}| \ll |\boldsymbol{K}|$ one gets [136]

$$E_{\pm}(\boldsymbol{q}) \approx \pm\nu_F|\boldsymbol{q}| + O(q^2) \tag{4.7}$$

where $\boldsymbol{q}$ is the momentum which is measured relatively to the Dirac points ($\boldsymbol{K}$,$\boldsymbol{K}'$) and $\nu_F = 3at/2 \simeq 10^6$ m/s is the Fermi velocity. Expanding the spectrum around the Dirac point $\boldsymbol{K}$ including t' up to the second order of q/K leads to

$$E_{\pm}(\boldsymbol{q}) \approx 3t' \pm \nu_F|\boldsymbol{q}| - \left(\frac{9t'a^2}{4} \pm \frac{3ta^2}{8}\sin(3\theta_{\boldsymbol{q}})\right)|\boldsymbol{q}|^2 \tag{4.8}$$

where

$$\theta_{\boldsymbol{q}} = \arctan\left(\frac{q_x}{q_y}\right) \tag{4.9}$$

is the angle in the momentum space. It can be concluded from (4.8) that the presence of t' leads to a shift of the Dirac points at the corners of the Brillouin zone results in a breaking of the electron-hole symmetry [134].

Dirac Fermions in Graphene and Helicity

Considering the Hamiltonian (4.4) with $t' = 0$, one can expand the electron fields a_n in the Fourier space around the Dirac points $\boldsymbol{K}$ and $\boldsymbol{K'}$ as the following

$$a_n \simeq e^{-i\boldsymbol{K}\cdot\boldsymbol{R}_n} a_{1,n} + e^{-i\boldsymbol{K'}\cdot\boldsymbol{R}_n} a_{2,n} \tag{4.10}$$

$$b_n \simeq e^{-i\boldsymbol{K}\cdot\boldsymbol{R}_n} b_{1,n} + e^{-i\boldsymbol{K'}\cdot\boldsymbol{R}_n} b_{2,n} \tag{4.11}$$

where the index $(1, 2)$ refers to the $(\boldsymbol{K}, \boldsymbol{K'})$ points and the fields $a_{i,n}, b_{i,n}$ on the right hand-side are considered to have a slow variation over a unit cell. For deriving a valid theory around Dirac points, one can consider this representation in the tight binding Hamiltonian (4.4) and expand the operators a_n and b_n up to linear order for the nearest neighbor vector (see figure 4.2), which means [134]

$$\sum_{\boldsymbol{\delta}} e^{\pm i\boldsymbol{K}\cdot\boldsymbol{\delta}} = \sum_{\boldsymbol{\delta}} e^{\pm i\boldsymbol{K'}\cdot\boldsymbol{\delta}} = 0. \tag{4.12}$$

The latter yields for the Hamiltonian (4.4) the expression [152]

$$H = -i\nu_F \int d(x, y)(\hat{\psi_1}^\dagger(\boldsymbol{r})\boldsymbol{\sigma}\cdot\nabla\hat{\psi}_1(\boldsymbol{r}) + \hat{\psi_2}^\dagger(\boldsymbol{r})\boldsymbol{\sigma^*}\cdot\nabla\hat{\psi}_2(\boldsymbol{r})) \tag{4.13}$$

where we have the Pauli matrices $\boldsymbol{\sigma} = (\sigma_x, \sigma_y)$, $\boldsymbol{\sigma}^* = (\sigma_x, -\sigma_y)$ and $\hat{\psi_i}^\dagger = (a_i^\dagger, b_i^\dagger)$, $(i = 1, 2)$. The two component spinor $\psi = \begin{pmatrix}\psi_A \\ \psi_B\end{pmatrix}$ thus combines the tight-binding wave functions for sublattices A and B. The corresponding quantum number is hence called *pseudo-spin*, and it is this pseudo-spin on which the σ matrices in (4.13) act. By contrast, the original Hamiltonian (4.4) and its effective description (4.13) are both diagonal in the real electron spin, which merely acts as a non-interacting "flavor" index in the effective model. In addition, there is also the "valley index" $i \in \{1, 2\}$ which indicates whether the spinor describes an electronic excitation at the Dirac point $\boldsymbol{K}$ $(i = 1)$ or $\boldsymbol{K'}$ $(i = 2)$.

The two component electron wave function close to the first Dirac point follows the 2D Dirac equation [134]

$$-i\nu_F\boldsymbol{\sigma}\cdot\nabla\psi(r) = E\psi(r) \tag{4.14}$$

which leads to the wave function in the momentum space for the momentum around the first Dirac point $\boldsymbol{K}$ as

$$\psi_{\pm,\boldsymbol{K}}(\boldsymbol{k}) = \frac{1}{\sqrt{2}}\begin{pmatrix} e^{-i\theta_{\boldsymbol{k}}/2} \\ \pm e^{i\theta_{\boldsymbol{k}}/2}\end{pmatrix}. \tag{4.15}$$

Here, the "$\pm$" signs refers to the eigenenergies $E = \pm\nu_F k$, which are related the upper and lower π bands associated with Dirac cones and $\theta_{\boldsymbol{k}}$ is the angle in momentum space given by (4.9). The above wave function is an eigenstate of the effective Hamiltonian $H_K = \nu_F\boldsymbol{\sigma}\cdot\boldsymbol{k}$. However, around the second Dirac point $\boldsymbol{K'}$ one can introduce the wave function as

$$\psi_{\pm,\boldsymbol{K'}}(\boldsymbol{k}) = \frac{1}{\sqrt{2}}\begin{pmatrix} e^{i\theta_{\boldsymbol{k}}/2} \\ \pm e^{-i\theta_{\boldsymbol{k}}/2}\end{pmatrix} \tag{4.16}$$

which is an eigenstate of the Hamiltonian $H_{K'} = \nu_F\boldsymbol{\sigma}^*\cdot\boldsymbol{k}$ (see (4.13)). One should pay attention that here $\boldsymbol{K}$ and $\boldsymbol{K'}$ are related to each other by time reversal symmetry, which is the same as reflection at the k_x axis: $(k_x, k_y) \to (k_x, -k_y)$. Moreover, if the phase $\theta_{\boldsymbol{k}}$ is rotated by 2π the wave function changes its sign as if it has π phase, which indicates that the wave function has two components of spinors [134].

Helicity or Chirality in Graphene

A very important quantity in our studies of graphene is the projection of the momentum operator along the pseudo-spin direction called *helicity*

$$\hat{h} = \frac{1}{2}\boldsymbol{\sigma} \cdot \frac{\boldsymbol{p}}{|\boldsymbol{p}|}. \tag{4.17}$$

Since $\hat{h}$ commutes with the effective Hamiltonian (4.13), we can take the energy eigenstates $\psi_{\pm}$ as the eigenstates of $\hat{h}$. In fact, near the Dirac point $\boldsymbol{K}$, we have

$$\hat{h}\psi_{\pm,\boldsymbol{K}}(r) = \pm\frac{1}{2}\psi_{\pm,\boldsymbol{K}}(r) \tag{4.18}$$

while near $\boldsymbol{K'}$ we have a similar relation but with the inverted sign

$$\hat{h}\psi_{\pm,\boldsymbol{K'}}(r) = \mp\frac{1}{2}\psi_{\pm,\boldsymbol{K'}}(r). \tag{4.19}$$

Equations (4.18) and (4.19) follow from $(\boldsymbol{\sigma} \cdot \hat{\boldsymbol{p}})^2 = \mathbb{1}$, which implies that $\hat{h}$ has the eigenvalues $\pm 1/2$. Moreover, for the particles with zero mass, helicity equals chirality.

For the Dirac point $\boldsymbol{K}$, one can consider the eigenfunctions for the upper cone (particles) as the one with chirality R and the lower one (holes) with the chirality L. However, this definition gets reversed on the Dirac point $\boldsymbol{K'}$, meaning that for the latter the particles gets labeled as the one with chirality L and the holes with the R chirality. The hexagonal form of the unit cells in graphene results in an even number of the Dirac cones, which makes graphene not to display chirality [153]. However, one should pay attention that in case of lattice deformations, where there might be a pentagonal unit cell on the honeycomb lattice, the situation is different.

Electron-Electron Interaction in Graphene

Considering the electron-electron interaction, one can write the Dirac Hamiltonian as [134, 154]

$$\begin{aligned}\mathcal{H}_G \equiv & -i\nu_F \int d^2x\, \psi^\dagger(x)\boldsymbol{\sigma} \cdot \boldsymbol{\nabla}\psi(x) \\ & + \frac{e^2}{2\epsilon_0}\int d^2(x,y)\, \frac{1}{|x-y|}\rho(x)\rho(y)\end{aligned} \tag{4.20}$$

where

$$\rho(x) = \psi^\dagger(x)\psi(x) \tag{4.21}$$

is the electron density. Here, the interesting point is that in graphene the photons interact in 3D space but the electrons are limited to the 2D graphene lattice. Thus, the Coulomb interaction breaks the Lorentz invariance of the problem and makes the problem different QED case [154, 155]. Furthermore, the Hamiltonian (4.20) only depends on two parameters ν_F and e^2/ϵ_0, where under the dimensional scaling, both parameters remain invariant. Moreover, ν_F is chosen to be dimensionless then the e^2/ϵ_0 can be also adjusted to be dimensionless, which means that the theory is renormalizable.

If a is the lattice spacing and m mass of electrons, dimensional analysis entails that the kinetic energy per site is $E_{Kin} \sim (ma^2)^{-1}$, while the electrostatic energy is $E_{Stat} \sim e^2/\epsilon_0 a$. Since $v_F \sim \frac{1}{ma}$ in graphene, we have a fine structure constant

$$\alpha = \frac{e^2}{v_F\epsilon_0} = \frac{e^2 ma}{\epsilon_0} = \frac{e^2/v_F\epsilon_0}{(ma^2)^{-1}} = \frac{E_{Kin}}{E_{Stat}} \sim 1. \tag{4.22}$$

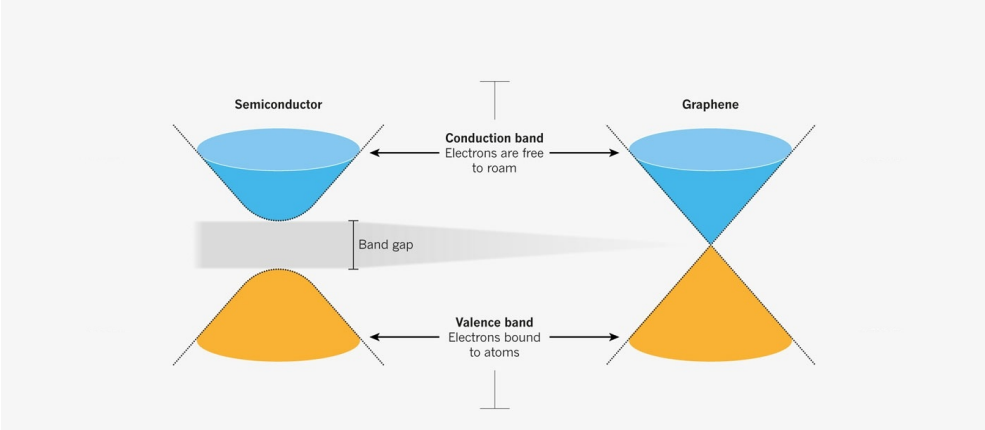

Figure 4.4.: Comparison between Dirac cones in a semiconductor and graphene. The semiconductor form is what one expects after chiral symmetry breaking in graphene as a semimetal. As it can be seen, the existence of a band gap makes the Dirac cones to have a different shape. The figure is adopted and reproduced with permission from [156].

This is consistent with $v_F \sim c/300$ and means that the effective Hamiltonian of graphene is strongly coupled.

Chiral Symmetry Breaking in Graphene

Introducing the Coulomb interaction in graphene, one of the important phenomena which we are interested in is the investigation of chiral symmetry breaking. The "brane-world" model of the low-energy excitations in graphene incorporates the Coulomb interaction by adding a 3D gauge field to the 2D fermions Hamiltonian (4.13). The corresponding action is

$$S = \int dx_0 \int d(x_1, x_2)\bar{\psi}^a \{i\not{D} - m\}\psi^a - \frac{1}{4}\int dx_0 \int d(x_1, x_2, x_3) F_{\mu\nu}F^{\mu\nu} \tag{4.23}$$

where $a = 1, 2, ..N$ is the pseudo-flavor index (original spin, $N = 2$ in graphene) and Dirac operator is

$$\not{D} = \gamma^0(\partial_0 + igA_0) + v_F \sum_{k=1}^{2} \gamma^k(\partial_k + igA_k), \quad g^2 = \frac{e^2}{\epsilon_0}. \tag{4.24}$$

Note the factor v_F is because the electrons propagate with speed $v_F \sim 1/300$ in the graphene plane ($k = 1, 2$), while photons propagate at the speed of light ($c = 1$) outside the plane. More importantly, the electron spinors are ψ component complex (Dirac) spinors built from the pseudo-spin and valley index

$$\psi = \begin{pmatrix} \psi_{k,A} \\ \psi_{k,B} \\ \psi_{k',A} \\ \psi_{k',B} \end{pmatrix}. \tag{4.25}$$

As a consequence the γ matrices obey the usual 4×4 Clifford algebra, and the chiral symmetry would be flavor rotations generated by

$$\{\mathbb{1}, \boldsymbol{\sigma}\} \otimes \{\mathbb{1}, \gamma_5\} \tag{4.26}$$

Figure 4.5.: The rainbow approximation for the fermion propagator used in DSE equations.

which gives the usual $U_A(N) \times U_V(N)$ symmetry. In graphene, however, the situation is slightly different: since (4.24) contains no $\gamma^3 D_3$ term (because the electrons are confined to xy-plane), we have a larger flavor symmetry generated by the $4N^2$ matrices

$$\{\mathbb{1}, \boldsymbol{\sigma}\} \otimes \{\mathbb{1}, \gamma_5, \gamma_3, \gamma_5\gamma_3\}. \tag{4.27}$$

This symmetry group is $U(2N)$ or $U(4)$ in case of graphene.

The mass term in (4.23) breaks chiral symmetry explicitly and should be absent in case of graphene, though generation of such a term by the experimental setup is possible [157]. The chiral $U(4)$ symmetry of graphene can break in several ways, which must at last maintain the $U(1)$ symmetry of phase transformations on the complex spinor ψ, which is related to the conservation of the current coupling to the gauge field. The currently discussed choices are: $U(4) \to U(2) \times U(2)$ for which the order parameter is the excitonic condensate $\langle\bar{\psi}\psi\rangle$ and $U(4) \to U(1)$ whose order parameter is $\langle\bar{\psi}\sigma_3\psi\rangle$ or anti-ferromagnetic condensate. The phenomenology of these breaking patterns is slightly different but they both lead to a gap in the electron dispersion, i.e. the π_+ and π_- band no longer touch each other and graphene turns into a semiconductor or even an insulator (see figure 4.4).

If we set $m = 0$ in (4.23), go to Coulomb gauge and assume that vacuum polarization effects through the vector gauge field $\boldsymbol{A}$ can be neglected as compared to the Coulomb interaction mediated by A_0, the elimination of A_0 with $\boldsymbol{A} \approx 0$ in (4.23) leads to (4.20), which is our starting point to study chiral symmetry breaking in graphene due to electron-electron interactions.

For the calculation of the gap equation we use the variational method in which we calculate the gap equation by minimizing the energy. The approach to the calculation of the gap equation, includes different steps, where in our case we start to find the propagators using DSEs as in section 2.3. However, in the general case for solving the DSEs, one must assume a particular form for the propagators for which we consider the *Rainbow approximation* [158].

4.2. Variational Hamiltonian Approach to Graphene

In this part we introduce the calculation of the gap equation in the brane-world QED for graphene. The procedure of the Hamiltonian approach in graphene case can be followed in [159]. However, we use the DSE approach for the calculation of the propagators as in QCD and for the fermion propagator we stick to the Rainbow approximation. The Rainbow approximation is the simplest way to deal with the DSE in a sense that it reduces the DSE up to the linear order [160, 161].

The ansatz for the vacuum wave-functional and the kernel is the same as what we used for the QCD case (2.134) but with 2D vectors x and y [159]

$$|\psi\rangle = \mathcal{N} \exp\left\{ -\int d(x,y)\, \psi_+^\dagger(x) K(x,y) \psi_-(y) \right\} |0\rangle\,. \tag{4.28}$$

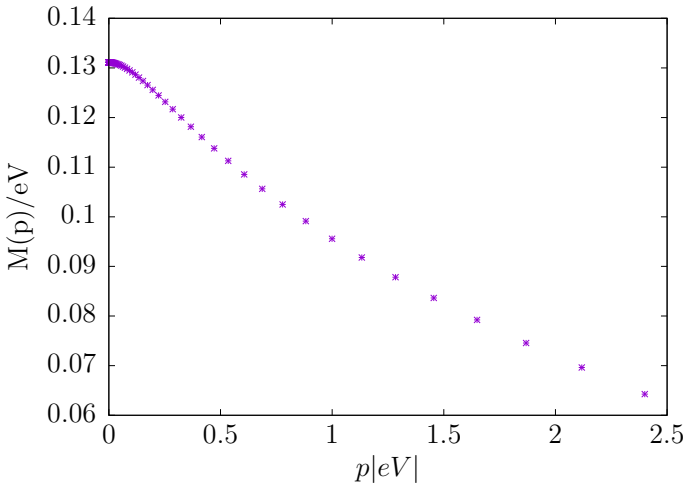

Figure 4.6.: The solution for mass function versus momentum for the fixed value of $\alpha = 5$ in the numerical calculations.

Here, $\mathcal{N}$ is the normalization factor and the ansatz for the kernel has the form

$$K(x,y) = \beta S(x,y) + e\int dz\, \boldsymbol{\alpha}\cdot\boldsymbol{V}(x,y;z)A(z) \tag{4.29}$$

where e is the coupling constant and $\boldsymbol{\alpha}$ and β are Dirac matrices. Moreover, the ansatz for the kernel is the same as what we considered in chapter 2, which means S is the scalar part of the kernel and $\boldsymbol{V}$ is the vector part.

Here, for the calculation of the energy we consider the Hamiltonian (4.20) which corresponds to the single particle and Coulomb part of (2.77) without color indices in 2+1 dimensions, but extra $N = 2$ flavor indices. That means that the Hamiltonian for graphene should have the form

$$\mathcal{H}_G = -\int d^2x\, \psi^\dagger(x)(i\boldsymbol{\alpha}\cdot\boldsymbol{\partial})\psi(x) + \frac{\bar{e}^2}{2}\int d^2(x,y)\,\rho(x)\mathcal{F}(x,y)\rho(y) \tag{4.30}$$

where ρ is given by (4.21). Here, we have worked out the flavor trace (so that ψ describes only a single flavor), rescaled $\mathcal{H}_G \to \mathcal{H}_G/Nv_F$ and defined

$$\bar{e}^2 = e^2N/(\epsilon_0 v_F) = 2e^2/\epsilon_0 v_F \tag{4.31}$$

which is dimensionless if $\hbar = c = 1$. Therefore, the expectation value of the Hamiltonian in our calculations has the form

$$\langle\mathcal{H}_G\rangle = \langle\mathcal{H}_D\rangle + \langle\mathcal{H}_C\rangle\,. \tag{4.32}$$

In order to calculate the propagators in 2+1 dimensions we recall equation (2.70) for the 2D momentum in the new form of

$$\mathcal{Q}_G = \frac{A(\boldsymbol{p})\boldsymbol{\alpha}\cdot\hat{\boldsymbol{p}} + \beta B(\boldsymbol{p})}{\Delta_{\boldsymbol{p}}} \tag{4.33}$$

where $\Delta_{\boldsymbol{p}} = A(\boldsymbol{p})^2 + B(\boldsymbol{p})^2$ and $A(\boldsymbol{p})$, $B(\boldsymbol{p})$ are the dressing functions as in equation (2.74). Recalling the related energy terms from (2.127) and working out the traces, we

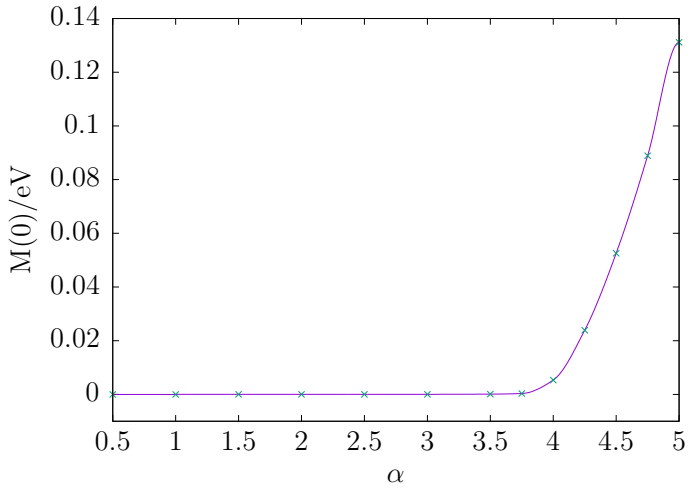

Figure 4.7.: The changes of the mass function for the different values of the α. As it can be seen, the phase transition starts from the value around $\alpha^* \approx 3.8$.

have for the Dirac part of the Hamiltonian

$$E_D = -4\int \frac{d^2q}{(2\pi)^2}\frac{qA(\boldsymbol{q})}{\Delta_q} + 2\bar{e}^2\int \frac{d^2(q,p)\,\mathcal{G}(\boldsymbol{q},\boldsymbol{p})V^2(\boldsymbol{p},\boldsymbol{q})}{(2\pi)^4}\frac{A(\boldsymbol{p})A(\boldsymbol{q})+B(\boldsymbol{p})B(\boldsymbol{q})}{\Delta_{\boldsymbol{p}}\Delta_{\boldsymbol{q}}} \tag{4.34}$$

and for the Coulomb part

$$\begin{aligned} E_C = -\frac{\bar{e}^2}{2}\int \frac{d^2(q,p)}{(2\pi)^4}\frac{\mathcal{F}(\boldsymbol{p},\boldsymbol{q})}{\Delta_{\boldsymbol{p}}\Delta_{\boldsymbol{q}}}\Big\{ & 4B(\boldsymbol{p})B(\boldsymbol{q}) \\ & + \hat{\boldsymbol{q}}\cdot\hat{\boldsymbol{p}}\Big[A(\boldsymbol{q})(2-A(\boldsymbol{q})) - B^2(\boldsymbol{q})\Big]\Big[A(\boldsymbol{p})(2-A(\boldsymbol{p})) - B^2(\boldsymbol{p})\Big]\Big\}. \end{aligned} \tag{4.35}$$

Furthermore, for the dimensionally reduced Coulomb kernel, we consider the form [159]

$$\mathcal{F}(\boldsymbol{p},\boldsymbol{q}) = \frac{1}{4\pi|\boldsymbol{q}-\boldsymbol{p}|}. \tag{4.36}$$

Discarding the coupling to the transverse photons and the associated polarization effect (i.e. $V(\boldsymbol{p},\boldsymbol{q}) = 0$, $A = 1$ and $B = S$), the energy terms get the simpler form

$$E_D = -4\int \frac{d^2q}{(2\pi)^2}\frac{|\boldsymbol{q}|}{1+S(\boldsymbol{q})^2} \tag{4.37}$$

and

$$E_C = -\frac{\bar{e}^2}{2}\int \frac{d^2(q,p)\,\mathcal{F}(\boldsymbol{p},\boldsymbol{q})}{(2\pi)^4}\left\{\frac{4S(\boldsymbol{p})S(\boldsymbol{q}) + \hat{\boldsymbol{p}}\cdot\hat{\boldsymbol{q}}\big[(1-S(\boldsymbol{q})^2)(1-S(\boldsymbol{p})^2)\big]}{(1+S(\boldsymbol{q})^2)(1+S(\boldsymbol{p})^2)}\right\}. \tag{4.38}$$

Doing variation for the energy terms (4.37) and (4.38) with respect to S, we have the gap equation

$$|\boldsymbol{p}|S(\boldsymbol{p}) = \frac{\bar{e}^2}{2}\int \frac{d^2q\,\mathcal{F}(\boldsymbol{p},\boldsymbol{q})}{(2\pi)^2}\frac{S(\boldsymbol{q})(1-S^2(\boldsymbol{p})) - S(\boldsymbol{p})(1-S(\boldsymbol{q})^2)\hat{\boldsymbol{q}}\cdot\hat{\boldsymbol{p}}}{(1+S(\boldsymbol{q})^2)} \tag{4.39}$$

which is the same as the BCS type gap equation (2.124) that we treated in chapter 2, but now in 2D with a 3D Coulomb kernel.

One of the points that one should consider is that equation (4.39) could have been derived in a procedure the same as what was done in section 2.5.2. There we derived the gap equation for a system of the coupled gluons and quarks and then discarded the explicit coupling in the kernel. That means if we do variation for the equations (4.34) and (4.35), we can derive the same equation (4.39) by setting the vector part of the kernel zero at the end. In order to show that, by considering the ratio of dressing functions as in (2.113) the equation after variation with respect to B has the form

$$\begin{aligned}|p|b_p =&\frac{\bar{e}^2}{2}\int \frac{d^2q\mathcal{G}(\boldsymbol{q},\boldsymbol{p})V^2(\boldsymbol{p},\boldsymbol{q})}{(2\pi)^2}\frac{b_q(1+b_p^2)-2b_p(1+b_pb_q)}{A(\boldsymbol{q})(1+b_q^2)}\\ &+\frac{\bar{e}^2}{2}\int\frac{d^2q}{(2\pi)^2}\,\mathcal{F}(\boldsymbol{q},\boldsymbol{p})\frac{b_q(1-b_p^2)-b_p\Big(2-A(\boldsymbol{q})(1+b_q^2)\Big)\hat{\boldsymbol{p}}\cdot\hat{\boldsymbol{q}}}{A(\boldsymbol{q})(1+b_q^2)}\end{aligned} \tag{4.40}$$

where again by discarding the vector kernel $V(\boldsymbol{p},\boldsymbol{q})$ we obtain equation (4.39). In this work, we only solve the BCS-type equation (4.39) and leave the inclusion of a vector kernel to future investigations, cf. the discussion below.

For the mass function, we use the same definition as for the QCD_{3+1} case (2.125) but for QED_{2+1}

$$M(\boldsymbol{p}) = 2|\boldsymbol{p}|\frac{S(\boldsymbol{p})}{1-S^2(\boldsymbol{p})}. \tag{4.41}$$

Thus the gap equation (4.39), is transformed to

$$M(\boldsymbol{p}) = \frac{\bar{e}^2}{2}\int\frac{d^2q\,\mathcal{F}(\boldsymbol{p},\boldsymbol{q})}{(2\pi)^2}\frac{1}{\sqrt{\boldsymbol{q}^2+M^2(\boldsymbol{q})}}\left[M(\boldsymbol{q})-\frac{|\boldsymbol{q}|z}{|\boldsymbol{p}|}M(\boldsymbol{p})\right]. \tag{4.42}$$

Preparing equation (4.42) for the numerical treatment, after replacing the Coulomb kernel with (4.36), in polar coordinates we have

$$M(\boldsymbol{p}) = G\int_\mu^\Lambda dq\int_{-1}^{+1}dz\mathcal{J}_2(\boldsymbol{q},z)\frac{1}{|\boldsymbol{q}-\boldsymbol{p}|}\frac{1}{\sqrt{\boldsymbol{q}^2+M^2(\boldsymbol{q})}}\left[M(\boldsymbol{q})-\frac{|\boldsymbol{q}|z}{|\boldsymbol{p}|}M(\boldsymbol{p})\right] \tag{4.43}$$

where $G=\alpha/(4\pi^2)$ and $\alpha = e^2/(4\pi\epsilon_0 v_F)$ is the graphene fine-structure constant. Moreover, for the upper limit of the integral one can introduce the natural cutoff of the lattice spacing for graphene which is $\Lambda = 2.4\mathrm{eV}$. As it can be seen in the equation (4.42), we have also the change of the variable z, which is the angular integration changed by the variable $z=\cos(\phi)$ in the polar coordinate and $\mathcal{J}_2(\boldsymbol{q},z)$ is the *Jacobian* with the general form of

$$\mathcal{J}_n(s,z) = \frac{2\pi^{\frac{n-1}{2}}}{\Gamma(\frac{n-1}{2})}\cdot s^{n-1}(1-z^2)^{\frac{n-3}{2}}. \tag{4.44}$$

Inserting the Jacobian (4.44) for $n=2$, equation (4.42) takes the form

$$\begin{aligned}M(\boldsymbol{p}) = G\int_\mu^\Lambda dq\int_{-1}^{+1}dz\,\frac{2|\boldsymbol{q}|}{\sqrt{1-z^2}}\frac{1}{\sqrt{\boldsymbol{p}^2+\boldsymbol{q}^2-2\boldsymbol{p}\boldsymbol{q}z}}\frac{1}{\sqrt{\boldsymbol{q}^2+M^2(\boldsymbol{q})}}\Bigg[M(\boldsymbol{q})\\ -\frac{|\boldsymbol{q}|z}{|\boldsymbol{p}|}M(\boldsymbol{p})\Bigg]\end{aligned} \tag{4.45}$$

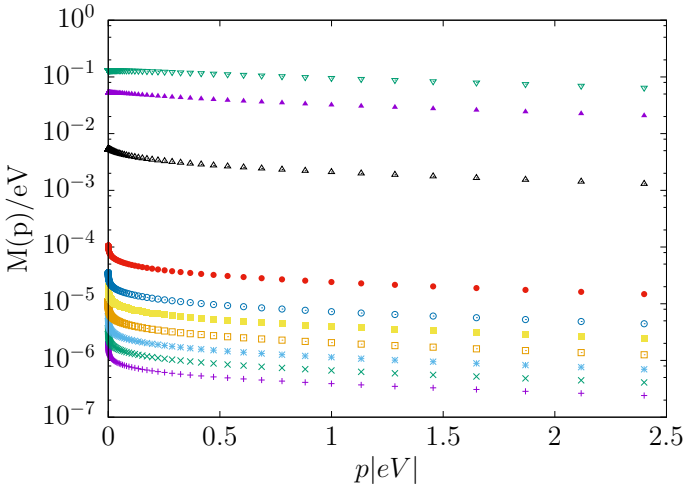

Figure 4.8.: The numerical solution for the mass function for the different values of α, where the obtained values for $M(0)$ increase as α changes from $\alpha = 1/2$ (bottom) to $\alpha = 5$ (top), for the lattice spacing cutoff $\Lambda = 2.4eV$.

as the final form of the gap equation for graphene, which we use for numerical calculations.

The procedure for solving equation (4.45) is the same as what has been done in chapter 2 for the BCS type gap equation in the QCD case. However, here the Coulomb kernel has a different form in comparison with the 3+1 dimensional case. The latter shows its characteristic in the form that in graphene case, we do not deal with the singularities which were arising for the IR regime in the case of QCD. That means for the Coulomb kernel in graphene case we do not face the divergence problems for which in the QCD case we needed to shift the momentum (i.e. $q \to q + p$) in order to avoid them. Moreover, in case of solving graphene gap equation (4.45), we considered the same structure for the mass function which we have in QCD and that implies the same way of the extrapolation and interpolation as it is defined in appendix B. The absence of the strong $1/q^4$ infrared singularity in the graphene case makes the gap equation (4.45) converge in less than 100 iterations, even without a series accelerator.

The result for the mass function in the equation (4.45) depends on the chosen values for α. As it can be seen in figure 4.7, the phase transition is around $\alpha^* \approx 3.8$ which is a large value in comparison to the experimental one in suspended graphene for the bare coupling (i.e. $\alpha_0 \approx 2.19$) [162]. Different approaches to graphene can lead to different values of critical α^*, which the reader can follow in [154, 163–166]. The results obtained for the different values of α in our calculations are shown in figure 4.8. Moreover, the mass function $M(\boldsymbol{p})$ behavior is shown in the figure 4.6, for a typical chosen value of α.

Our critical value of $\alpha^* \approx 3.8$ indicates that suspended graphene is still in the chirally symmetric phase without an energy gap, in agreement with its semimetal character. However, typical non-perturbative calculations in other approaches lead to smaller values for the critical α^*. In addition, the renormalization effects on v_F induced by polarization lead to reduce the effective α in graphene, as do dielectricity effects of the substrate so that the real α in graphene could be even smaller than 1. There are two ways in which our calculations can be improved, which would both lead to smaller critical α^*, i.e. to stronger chiral symmetry breaking:

1. Including vacuum polarization and substrate effects in the Coulomb kernel (4.36).

2. Extending the variational kernel to include explicit couplings to the transversal pho-

tons via structures $V(\boldsymbol{p}, \boldsymbol{q})$ and $W(\boldsymbol{p}, \boldsymbol{q})$, as was done in chapter 2 in QCD case.

Both improvements should be included simultaneously, as they both correct the approximation $\boldsymbol{A} \approx 0$ in the Hamiltonian (4.20). Our experience in chapter 2 indicates that the inclusion of these forms increases the excitation condensate $\langle \bar{\psi}\psi \rangle$ and hence the strength of chiral symmetry breaking. It is therefore expected that they lead to a smaller critical coupling α^* for the transition. This interesting investigation, as well as the inclusion of further operators in the Hamiltonian to describe non-linear effects in the electron dispersion, must be left for future investigations.

5. Summary and Outlook

In this thesis, we studied the variational Hamiltonian approach as an efficient approach for treating strongly coupled quantum fields theories. This is particularly important in theories like QCD, where studying the phase diagram by numerical lattice calculations is hampered due to the sign problem. In this thesis after reviewing the basics of quantum field theory, we introduced the variational Hamiltonian approach to QCD. First, we introduced the ansatz for the trial vacuum wave functional which we considered for solving the Schrödinger equation. Next, we calculated the vacuum energy by sandwiching the QCD Hamiltonian between the trial wave functional and its complex conjugate and then we minimized the energy in order to find the structure of the kernel which we considered in the vacuum wave functional. We extracted the mass function from the quark propagator and we solved the gap equation with the goal of finding a non-trivial answer as a probable sign for chiral symmetry breaking.

We solved the gap equation for a system of quarks coupled only through the Coulomb interaction numerically, for which we obtained the value $\langle\bar{q}q\rangle = (-185\text{MeV})^3$ for the chiral condensate as an order parameter of chiral symmetry breaking. Furthermore, by defining a proper ansatz for the vacuum wave functional we solved numerically the quark gap equation with exact cancellation of the UV divergences for a coupled system of quarks and transverse gluons. For such a system, we calculated the quark condensate and for a fixed value of the coupling constant we obtained the value $\langle\bar{q}q\rangle = (-235\text{MeV})^3$ which is in accordance with the one calculated by phenomenological methods.

As the first step to explore the QCD phase diagram, the $T = 0$ investigations of chapter 2 were extended to finite-temperature in chapter 3. We solved the uncoupled quark gap equation for the quark sector of QCD on a compactified manifold at finite temperature. The result is a second order phase transition from a chirally broken phase at $T < T^*$ to a chirally symmetric phase at $T \geq T^*$, where the critical temperature is $T^* \approx 90$ MeV for the usual value of the Coulomb string tension which we considered in the zero temperature calculations. This result is in accordance with other non-perturbative studies even if the transition temperature is somewhat smaller than the result obtained in lattice calculations. Moreover, if the scale is fixed to match the phenomenological value of the quark condensate at $T = 0$ the critical temperature increases to $T^* = 115$ MeV.

In the last chapter, we demonstrated the versatility of the variational Hamiltonian approach by applying it to the electrons in graphene, a unique material with extraordinary properties. We showed that the Coulomb interaction breaks the chiral symmetry in graphene and leads to the phase transition from a semimetal to a semiconductor or insulator at the critical coupling $\alpha^* \approx 3.8$. This result is in fair agreement with other non-perturbative approaches, in particular since a number of refinements, like vacuum polarization or renormalization, have been left for future investigations.

The methods and techniques which have been used in this thesis are very general and applicable to a variety of situations, of which QCD and graphene were just two examples. While studying these examples, the thesis has revealed a number of interesting questions which could not be solved immediately but can be tackled by variational Hamiltonian approach in the future. As the outlook of this work, one can mention the extension of the variational calculation to QCD at finite temperature and finite baryon density. Explaining

the latter more, in this thesis we solved the gap equation for a system of quarks in the absence of the gluons in the trial wave functional at finite temperature for zero chemical potential. Therefore, as the first step to extend our calculations one should investigate the possibility of solving the quark gap equation at finite temperature but in presence of the chemical potential, which leads us to the most interesting part of the QCD phase diagram where the present approach is superior to the lattice calculations. A second extension of our calculations would be the inclusion of the explicit quark-gluon coupling in finite-temperature calculations. Using the same techniques, it should be possible to investigate the thermodynamical properties of QCD by analyzing parameters such as pressure and free energy as another point of the outlook for QCD at finite temperature. Also, the *Polyakov loop* can be studied as an order parameter for confinement for which currently a project is persuaded.

For improvement of the results obtained by our approach to graphene, the inclusion of the vacuum polarization and additional operators in the effective field theory should be considered. Also, studying the behavior of graphene under strong magnetic fields could be mentioned. Moreover, the variational Hamiltonian approach might be useful to study topological insulators, or in general non-standard superconductivity.

Lastly, I believe that the variational Hamiltonian approach can be practical in all these studies. I hope the present thesis can provide a starting point for the application of the variational Hamiltonian method to a more widespread range. Furthermore, for the future improvements of this method, I hope this thesis will be useful.

Appendices

A. Dirac Matrices

The Dirac matrices obey the anti-commutation rule

$$\{\gamma^\mu, \gamma^\nu\} = 2g^{\mu\nu} \tag{A.1}$$

where the $g^{\mu\nu}$ is the metric tensor in Minkowski space (i.e. $g^{\mu\nu} = \text{diag}(1, -1, -1, -1)$).

The form of the γ matrices in Dirac basis is as

$$\gamma^\mu = \begin{pmatrix} 0 & \sigma^\mu \\ -\sigma^\mu & 0 \end{pmatrix}, \qquad \gamma^0 = \begin{pmatrix} \mathbb{1} & 0 \\ 0 & -\mathbb{1} \end{pmatrix}, \qquad \gamma^5 = \begin{pmatrix} 0 & \mathbb{1} \\ \mathbb{1} & 0 \end{pmatrix} \tag{A.2}$$

where

$$\sigma^x = \begin{pmatrix} 0 & 1 \\ 1 & 0 \end{pmatrix}, \qquad \sigma^y = \begin{pmatrix} 0 & -i \\ i & 0 \end{pmatrix}, \qquad \sigma^z = \begin{pmatrix} 1 & 0 \\ 0 & -1 \end{pmatrix}. \tag{A.3}$$

For $\gamma^0 \equiv \beta$ and $\gamma^i \equiv \beta\alpha^i$ we have the identities

$$\{\alpha^i, \beta\} = 0 \tag{A.4}$$

and

$$(\alpha^i)^2 = \beta^2 = \mathbb{1}. \tag{A.5}$$

Furthermore

$$Tr\{\alpha^i\} = Tr\{\beta\} = Tr\{\gamma^5\} = Tr\{\alpha^i\beta^2\} = 0 \tag{A.6}$$

$$Tr\{\alpha^i\alpha^j\} = 4\delta^{ij} \tag{A.7}$$

$$\frac{1}{4}Tr\{\alpha^i\alpha^j\alpha^k\alpha^l\} = \delta^{ij}\delta^{kl} - \delta^{ik}\delta^{jl} + \delta^{il}\delta^{jk}. \tag{A.8}$$

B. Numerical Methods

In this chapter, we review the numerical methods which are used for the treatment of the integral equations in this thesis. The main characteristic of the integral equations we deal with, is that they are non-linear in the unknown function. In order to solve such integral equations numerically we use the *iterative relaxation* method, in which we obtain the final solution after a sequence of iterative steps. In this method the numerical solution gets updated on each step until the point where this progression does not improve the solution anymore.

In order to solve the integral equations numerically in this work, we deal with some concepts like *coordinates*, *nodes*, *interpolation*, *extrapolation* etc. In this chapter, I introduce these concepts as the basic tools for treating the integral equations. Furthermore, the specific methods which have been used for solving the integral equations in the chapters before, are introduced as the conclusion of this chapter. The material in this chapter consists mainly of standard algorithms which have been combined in a special way for this thesis. In the presentation of the basic tools, we follow reference [167].

B.1. Defining the Function

As the first step, the numerical representation of an unknown analytical function $f(x)$ is through discretization, i.e. we represent it as a function depending on discrete values $f(x_i)$ where x_i represents the sampling points. More precisely, we define the independent coordinate x in a compact range $[\mu, \Lambda]$ with N equidistant mesh points

$$\begin{aligned} x_i &= \mu + i \times \Delta \qquad 0 \leq i < N \\ \Delta &\equiv \frac{\Lambda - \mu}{N-1}. \end{aligned} \tag{B.1}$$

Such equidistant meshes are usually appropriate for compact coordinates such as $z = \cos\theta \in [-1, 1]$. In the integral equations in this thesis, we will, however, often deal with non-compact coordinates such as the momentum norm $|\vec{p}| \in [0, \infty[$. In this case, we employ an infrared and ultraviolet cutoff μ and Λ respectively, but we distribute more mesh points in the IR region by means of logarithmic mesh

$$x_i = \mu \times \left(\frac{\Lambda}{\mu}\right)^{\frac{i}{N-1}}. \tag{B.2}$$

This is because the main dynamics of our integral equation will occur in the IR region.

B.2. Interpolation and Extrapolation

For understanding the necessity of the interpolation and extrapolation, first consider a function like $f(x)$ whose values are known just for a set of points like $x_0, x_1, x_2, ...x_{N-1}$. In order to know the values of the function $f(x)$ for the arbitrary values of x in an interval we need to use interpolation. Interpolation, is basically the method by means of which one

can make a set of data points inside the given interval. On the other hand, extrapolation can also be defined the same as interpolation but for a set of points outside interval.

The simplest interpolation method is the linear interpolation where we connect two nodes by a straight line. Using two known values of a function at two points like x_0 and x_1, we can define the value of the function in the chosen point x as

$$\tilde{f}(x) = f(x_0) + \frac{f(x_1) - f(x_0)}{x_1 - x_0}(x - x_0). \tag{B.3}$$

However, in the case of dealing with logarithmic coordinates, the interpolation has the form

$$\tilde{f}(x) = f(x_0) \times (\frac{x}{x_0})^{\alpha} \tag{B.4}$$

where the power α has the form

$$\alpha = \frac{\log(\frac{f(x_0)}{f(x_1)})}{\log(\frac{x_1}{x_0})}. \tag{B.5}$$

We name the above formula the *log-lin* or the *power-law* interpolation. Unlike the linear formula (B.3), we can use the power law (B.5) also to perform extrapolation.

B.2.1. Cubic Spline Interpolation

Not all the functions we are going to deal with can be treated by linear or power-law interpolation. We know that in our calculations we deal with curves for which we need a more flexible and accurate algorithm in order to find the connection between the nodes. Therefore, we get involved with the *cubic Spline* interpolation method by means of which we can use higher order of smoothness for connecting the nodes to each other.

For starting, let us consider a tabulated function $f_i = f(x_i)$, $i = 0, ..., N-1$. Considering just one of the intervals between x_j and x_{j+1}, the linear interpolation (B.3) gives us [167]

$$f = Af_j + Bf_{j+1} \tag{B.6}$$

where

$$\begin{aligned} A &\equiv \frac{x_{j+1} - x}{x_{j+1} - x_j} \\ B &\equiv \frac{x - x_j}{x_{j+1} - x_j} = 1 - A. \end{aligned} \tag{B.7}$$

Since we consider above equations for the tabulated function f_i we can also introduce tabulated values for the second derivative f_i'' then for each interval, we can add a cubic polynomial to the right-hand side of the equation (B.6) whose second derivative varies between f_j'' to f_{j+1}''. Thus, one can define a more expanded form for the equation (B.6) as

$$f = Af_j + Bf_{j+1} + Cf_j'' + Df_{j+1}'' \tag{B.8}$$

where by the definition for A and B in (B.7), for C and D we have [167]

$$C \equiv \frac{1}{6}(A^3 - A)(x_{j+1} - x_j)^2 \tag{B.9}$$

$$D \equiv \frac{1}{6}(B^3 - B)(x_{j+1} - x_j)^2. \tag{B.10}$$

The problem here is that f_i''s in (B.8) are unknown. Taking derivative of equation (B.8) and by using the definitions for A, B, C and D one can get

$$\frac{df}{dx} = \frac{f_{j+1} - f_j}{x_{j+1} - x_j} - \frac{3A^2 - 1}{6}(x_{j+1} - x_j)f_j'' + \frac{3B^2 - 1}{6}(x_{j+1} - x_j)f_{j+1}''. \tag{B.11}$$

By putting above equation, evaluated for $x = x_j$ in the interval (x_j, x_{j+1}) equal to the same equation for the interval (x_{j-1}, x_j), ($j = 1...N-2$), one can find [167]

$$\frac{x_j - x_{j-1}}{6}f_j'' + \frac{x_{j+1} - x_{j-1}}{3}f_j'' + \frac{x_{j+1} - x_j}{6}f_{j+1}'' = \frac{f_{j+1} - f_j}{x_{j+1} - x_j} - \frac{f_j - f_{j-1}}{x_j - x_{j-1}} \tag{B.12}$$

which are $N-2$ equations for the N unknown f_i'' $(i = 0, ..., N-1)$. The last step here for finding a unique solution for the equation (B.12) is to take boundary conditions for x_0 and x_{N-1}. The frequent ways of doing the latter are either considering one or both f_0'' and f_{N-1}'' zero, or setting both f_0'' and f_{N-1}'' to the values calculated from equation (B.11) in order to fix values of the first derivatives of the interpolated function on the boundaries [167].

One of the important characteristics of the spline routine, in the programming, is that it is just needed to be called once during calculation for each iteration, which means it is not an expensive routine despite of simulating smooth and continuous function over the desired interval.

B.2.2. Extrapolation

As it is already mentioned, for the determination of a function outside its definition range $[x_0, x_{N-1}]$ we should use extrapolation. The simplest method for the treatment of the function beyond the interval can be just considering the last two points of that and fitting a straight line through them. Such linear extrapolations are rarely useful as they can only be used in the immediate neighborhood of the definition range. Hence, one can use other methods for extrapolation by introducing a polynomial, where the procedure is the same as the polynomial interpolation, in which for a set of data points one should find a curve which passes through all the nodes by using a polynomial. In our case, typically the mass functions that we deal with are known (or at least expected) to have the form of the power-law for the UV part or when the coordinates value gets larger and a constant form for the IR part or when the coordinates are small enough. Therefore, in our case the extrapolation for the so called IR region is rather simple. That means for a point like $x < x_0$ which is out of the interval $[x_0, x_{N-1}]$ we simply read the function value as $f(x_0)$[1]. However, for the case of the UV extrapolation we extrapolate our function as in the form of

$$f(x) = \frac{c}{x^k} \tag{B.13}$$

by fitting the last two nodes on the interval in such a function and considering it as the UV behavior of our function out of interval. However, the nodes are usually defined on a logarithmic mesh, which gives a form as in equation (B.5) for the UV extrapolation and that is the form which has been used in the numerical calculations in this work.

[1]The extrapolated function thus obeys the boundary condition $f'(0) = 0$ which is actually a necessary consequence for a self-consistent solution of the Adler-Davis equation (2.126) and its generalization.

B.3. Numerical Integration

After defining a setting for coordinates and knowing how to deal with the nodes in and out of the interval, now we can define a strategy for integrating the integrands. Historically, dealing with numerical integration or *quadrature* goes back to the ancient times. The etymology of the term quadrature implicates: "to determine the area" which started from the time that ancient Greek mathematicians understood determination of an area by geometrically constructing the same area for a square. However, later the term quadrature cited calculation of the area by means of any method [168]. Although it is considered that the development of integral calculus started by the works of Cavalieri, it was Leibniz and Newton who invented the modern *differential and integral calculus* which, after decades, is still used by scientists [169]. Knowing all that, first we start with the moderate formula *extended trapezoidal rule* which is used for the approximation of the finite integrals.

Newton-Cotes Formulas

Recalling the tabulated function f_i for a set of sampling points labeled as $x_0, x_1, ..., x_n$ with uniform distance $h = |x_j - x_{j-1}|$, the trapezoidal rule has the form [167]

$$\int_{x_0}^{x_1} f(x)dx = \frac{h}{2}[f_0 + f_1] + O(h^3 f'') \tag{B.14}$$

where the error $O(s)$ implies the difference between the true and approximated answers. Furthermore, the equation above is a two-point formula which means that it is exact for polynomials up to first degree ($f(x) = x$). One can also consider the formula for the three-point case which is also exact up to the 3rd degree or $f(x) = x^3$ (i.e. the *Simpson's rule*)

$$\int_{x_0}^{x_2} f(x)dx = \frac{h}{3}[f_0 + 4f_1 + f_2] + O(h^5 f^{(4)}). \tag{B.15}$$

The formula above can be extended to higher orders (*Newton-Cotes*). For instance, at 5th order, we have

$$\int_{x_0}^{x_1} f(x)dx = \frac{h}{24}[55f_1 - 59f_2 + 37f_3 - 9f_4] + O(h^5 f^{(4)}). \tag{B.16}$$

Extension of above formula for higher orders leads to the general form of the trapezoidal rule

$$\int_{x_0}^{x_{N-1}} f(x)dx = h[1/2f_0 + f_1 + f_2 + ... + f_{N-2} + 1/2f_{N-1}] + O\Big(\frac{(b-a)^3 f''}{N^2}\Big) \tag{B.17}$$

where the error has been assumed in terms of the interval $a - b$ for N numbers of the points. Moreover, one can call the extended form of the Simpson's formula (B.15) which has the form

$$\int_{x_0}^{x_{N-1}} f(x)dx = \frac{h}{3}[f_0 + 4f_1 + 2f_2 + 4f_3 + ... + 2f_{N-3} + 4f_{N-2} + f_{N-1}] + O(\frac{1}{N^4}) \tag{B.18}$$

where we can see that the number of points is very effective in the reduction of the error.

B.3.1. Gaussian Quadrature

As we saw in the last section, the integral we deal with can be approximated by sum of integrand values over a set of equally spaced points multiplied by a certain weighting coefficients. Using the *Gaussian quadratures*, one has the freedom for not only choosing the weighting coefficients, but also the abscissas on which the function values are evaluated. Furthermore, another feature of the Gaussian quadrature is that one can arrange the choice of the weights and abscissas to make the integral exact for a class of integrands polynomial times some known function $W(x)$. This has the advantage that $W(x)$ can be chosen in a way to extract a known analytical approximation to the integrand, or even to remove the integrable singularities. Expressing what has been said in the mathematical language, one can find a set of weights in such a way to approximate an finite integral as

$$\int_a^b W(x)f(x)dx \approx \sum_{i=0}^{N-1} w_i f(x_i) \tag{B.19}$$

which is exact if $f(x)$ is a polynomial. As an example, for an angular integral like

$$\int_0^\pi d\theta f(\cos\theta) = \int_{-1}^1 \frac{dx}{\sqrt{1-x^2}} f(x) \tag{B.20}$$

one might choose the weight function as the *Gauss-Chebyshev* weight function which has the form

$$W(x) = \frac{1}{\sqrt{1-x^2}}. \tag{B.21}$$

Although there is always possible to use classical known weight functions as in the last example, there is sometimes a demand for defining the weight functions. It is possible to find a *monic*[2] set of polynomials like $p_j(x)$ which are *orthogonal*[3] over the weight function $W(x)$ given as [167]

$$p_{j+1}(x) = (x - a_j)p_j(x) - b_j p_{j-1}(x) \qquad j = 0, 1, 2, ... \tag{B.22}$$

where the coefficients are defined as

$$\begin{aligned} a_j &= \frac{\langle xp_j|p_j\rangle}{\langle p_j|p_j\rangle} \qquad j = 0, 1, ... \\ b_j &= \frac{\langle p_j|p_j\rangle}{\langle p_{j-1}|p_{j-1}\rangle} \qquad j = 1, 2, ... \ . \end{aligned} \tag{B.23}$$

Moreover, by dividing each polynomial to $[\langle p_j|p_j\rangle]^{1/2}$ one can define a set of orthonormal polynomials. Furthermore, by the means of root finding methods one can find exact roots of each polynomial. The reason for finding the roots of polynomials is that the abscissas of the N-point Gaussian quadrature are basically the roots of the orthogonal polynomials $p_N(x)$. Once the abscissas are known, one needs to find the weights w_j which can be obtained by solving a set of linear equations for the polynomials [167].

B.3.2. Gauss-Legendre Integration Method

Knowing how to find the abscissas and the weights for different intervals, one can make a set of weights each suitable for a different case. For our case, among all the methods

[2]The coefficient of their leading term is unity.
[3]Two functions are orthogonal, if their scalar product is zero.

which can be used for the calculation of the integrals, we would like to use *Gauss-Legendre* method as the one with the simplest weight function $W(x) = 1;\ -1 < x < 1$. However, for highly oscillating integrands like the case of trigonometric functions we can not use the simple Gauss-Legendre method. In case of treating highly oscillating integrands one can use the methods like the *double exponential* method [130] or *Filon's* method [170] which is a method based on modified Simpson's rule (B.15) [171].

Returning to the simple case $W(x) = 1$, the associated polynomials P_i for defining the weight function are Legendre polynomials for which we have [172–175]

$$(i+1)P_{i+1} = (2i+1)xP_i - iP_{i-1} \tag{B.24}$$

where the weights are defined as

$$w_i = \frac{2}{(1-x_i^2)[P_N(x_i)]^2}. \tag{B.25}$$

The routine we used in our programs scales the boundaries of the integral from (x_1, x_2) to $(-1, 1)$, which makes it possible to use the Gauss-Legendre method for any integration interval. Moreover, it arranges the abscissas x_i and weights w_i for the Gaussian formula

$$\int_{x_1}^{x_2} f(x)dx = \sum_{i=0}^{N-1} w_i f(x_i) \tag{B.26}$$

which we consider as the formula each non-oscillatory integral transforms to in our C++ program.

B.4. Solving the Integrals Numerically

The integral equations we deal with in this thesis, generally have the form

$$f(\vec{x}) = \int dy\ \mathcal{I}(\vec{x}, \vec{y}; f(\vec{x}), f(\vec{y})) + g(\vec{x}) \tag{B.27}$$

where f is an unknown function (e.g. the mass function (2.125)) that should be calculated numerically. After transformation of the coordinates either to spherical or cylindrical coordinates as the desired framework according to the problem we deal with, we obtain

$$f(x) = \int_{\mu}^{\Lambda} dy \int_{\gamma}^{\nu} \mathcal{I}(x, y, z; f(x), f(y)) + g(x) \tag{B.28}$$

where e.g. for spherical coordinates

$$x = |\vec{x}|, \quad y = |\vec{y}|, \quad z = \cos \sphericalangle(\vec{x}, \vec{y}). \tag{B.29}$$

Next, we apply the Gaussian formula (B.26) to each integrand. That generally means for the parts we integrate over, the right hand-side of equation (B.27) gets the form

$$\sum_{i=0}^{N-1} \sum_{j=0}^{M-1} w_{y_i} w_{z_j} \mathcal{I}(x, y_i, z_j, f(x), f(y_i)) + g(x). \tag{B.30}$$

Here, the reader should pay attention that although we do not define the nodes for the external coordinates at Gauss-Legendre points, the external coordinate will be still discrete as explained in section B.1. After discrete definition of the integral (B.27), we are now ready to find its solution for which we use the relaxation method.

B.4.1. Relaxation Method

The method which has been used for solving the integral equations in this thesis is the iterative relaxation method. This method can be considered as the only method for the calculation of non-linear integral equations. In order to make the iteration procedure more clear, we label the f function on the right hand-side of the integral equation as f^n and the same function on the left hand-side as f^{n+1} where n is the number of iteration.

Writing the equation (B.27) in the *iterative notation*, we have

$$f^{n+1} = g + \int \mathcal{K}(f^n). \tag{B.31}$$

We explain the iteration procedure where we start the iteration by considering a starting function which is the initial value we consider for f^n in the above formula. The next step is the calculation of the above integral by means of any method, in our case Gauss-Legendre method, and finding the solution. The initial function f^0 can be largely arbitrary; common choices are a constant, or a known analytical approximation. The most important point here is that, the answer of the integral equation should not depend on the starting function.

The third step here is basically the same as the first step with the difference that in this step instead of initial starting function value we use the solution from one iteration before and we insert it in the integral and we continue the same loop until nth iteration. What is obvious here is that this loop can continue until forever if one does not stop the iteration, however, in our case we continue until a chosen error depending on when we want to cut the iteration. What is important for us is to continue this loop until a point that we do not see any progressive change in the solution. Therefore, we define errors regarding which we can adjust the point where the iteration should stop.

The simplest condition that we can here introduce, can be to define *absolute error* which compares the difference between f^n and f^{n+1}

$$E_{Abs} = ||f^n - f^{n+1}|| = \max_{x_i} |f^n(x_i) - f^{n+1}(x_i)|. \tag{B.32}$$

Using above definition, we can measure that how far we are from a stable answer for f. For example if we define the limit ϵ we can set the iteration to stop for a value like $\epsilon = 10^{-6}$, which at the first glimpse should be a fair choice. However, this value depends on the chosen scale, which means that we cannot trust the value of error. Therefore, we define the *relative error* which is the scaled form of (B.32)

$$E_{Rel} = \frac{|f^n - f^{n+1}|}{|f^n|}. \tag{B.33}$$

However, by this definition here the value for ϵ should be smaller than in the calculation of the absolute error. The point that might be noticeable in (B.33) is that for small f^n values the error becomes large, although for large values of f^n it converges so fast. For the absolute error there is also an inaccuracy problem, meaning that considering this error in the calculations, depending on the situation, it might make the iteration to end before having a stable answer. Therefore, in order to check both cases, we have calculated both errors (B.32) and (B.33) simultaneously in our programs[4].

One of the important points in our numerical calculations is how to update the function f^{n+1} in the integrand from one iteration to the other. For that matter, we compute the

[4]We considered for the limit of the absolute error $\epsilon = 10^{-6}$ and for the relative error $\epsilon = 10^{-10}$.

candidate f^{n+1} from the right hand-side of the integral equation, but really choose the next iteration as

$$f^{n+1} \to (1-\delta) \times f^n + \delta \times f^{n+1} \tag{B.34}$$

which is basically the *Gauss-Seidel* algorithm as it has been used in [92, 176]. The value of δ we chose depends on different parameters for solving the equation. For instance, if we use iterative method for equation (B.27) in 2D instead of 3D we can chose a larger value for δ. Furthermore, if we treat equation (B.27) in spherical coordinates instead of cylindrical coordinates, that makes a difference in the value we can chose for δ. However, setting the value of the update to its minimum (i.e. $\delta = 0$) results in no change in the solution. In general, small values of δ reduce the speed of which the relaxation progresses, which reduces efficiency but increases stability. Closer to the convergence of the iteration, one can even choose values $1 < \delta < 2$ (*overrelaxation*) to increase the efficiency[5]. Some iterations such as the case of Adler-Davis equation (2.126) calculated in this thesis converge very slowly and must be severely underrelaxed ($\delta << 1$) for stability. In this case, the efficiency can be increased by using series accelerators. These are algorithms that replace a given iteration series (f^n) with a faster converging series with the same limit[6]. Such methods were also tested for solving the zero-temperature gap equation (2.132). For instance, using *Aitken's* Δ^2 method [177], the iteration number reduced by almost factor 20. Moreover, it is also possible to replace Aitken's Δ^2 method with other methods in the updating process[7]. For example, beside testing this method for the zero-temperature gap equation (2.132) we also tested *Anderson's acceleration* method [179] which gives us a more promising result. In this method, we should solve a $k \times k$ matrix for each iteration, where $k \geq 1$ refers to the number of the dimensions of the sub-space in which a univariate secant method is applied. Using this method for values up to $k = 18$ reduces the number of iterations for equation (2.132) by almost a factor of 100 [122].

B.5. Interpolation and Extrapolation in 2D

For the finite-temperature calculations, our solutions will generally depend on two arguments, $f(x, y)$. We must then employ a method to inter/extrapolate $f(x_i, y_j)$ from its defining mesh (x_i, y_j). The procedure for the two dimensional interpolation can be considered as the same for the one dimensional case. However, in the 2D case we treat each of the axes as a independent 1D axis. Although treating the problem as a 2D problem does not make that much change for the interpolation region, it changes a lot for the extrapolation. As we can see in figure B.1, in the 2D case we deal with 9 interpolation and extrapolation regions where for each region there is a need for a prescription. Noticing that for the region at the center we should use interpolation, we first consider 2D interpolation methods. For instance, the linear interpolation in 1D can be extended to 2D *bilinear* interpolation.

B.5.1. Bilinear Interpolation

We want to find the values of an unknown 2D function $f(x, y)$ for which we assume that we know the values of the function at the points $f(x_1, y_1), f(x_1, y_2), f(x_2, y_1), f(x_2, y_2)$.

[5] It can be shown analytically that the iteration no longer convergence if $\delta > 2$ [167].

[6] In order to prevent discontinuities in the solution, we must apply the acceleration uniformly at each position $f^n(r_i)$, $0 \leq i \leq N-1$. This is called a *vector sequence acceleration*.

[7] Aitken's Δ^2 process is a sequence accelerator method. This method is useful for finding solution for oscillating functions. In this method the answer gets updated using 3 terms of a sequence and that is why it converges rapidly. In order to converge a sequence using more than 3 terms, there are other methods for which one can use *Wynn's epsilon method* [131, 178].

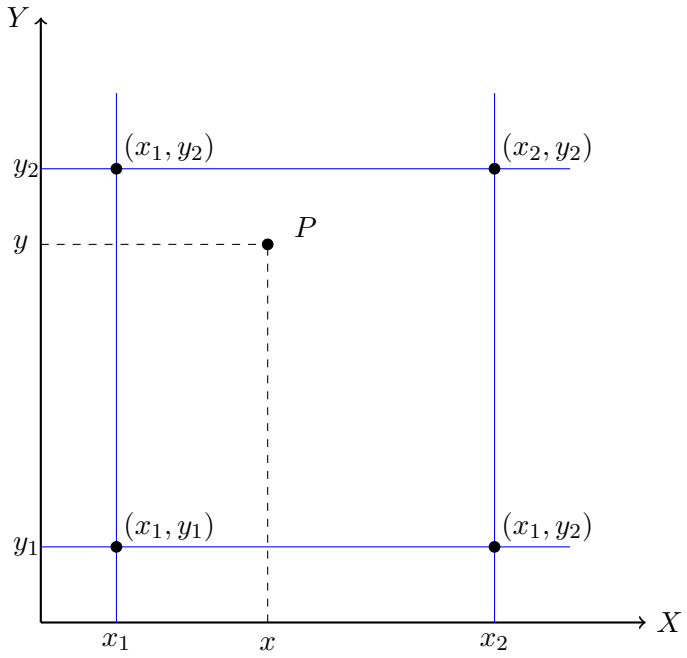

Figure B.1.: The data points (x_n, y_n) and P, the point for which we want to interpolate.

Therefore, we can first write the formula for the linear interpolation in the x direction

$$f(x, y_1) \approx \frac{x_2 - x}{x_2 - x_1} f(x_1, y_1) + \frac{x - x_1}{x_2 - x_1} f(x_2, y_1) \tag{B.35}$$

$$f(x, y_2) \approx \frac{x_2 - x}{x_2 - x_1} f(x_1, y_2) + \frac{x - x_1}{x_2 - x_1} f(x_2, y_2). \tag{B.36}$$

Interpolating in the y direction leads to

$$f(x, y) \approx \frac{y_2 - y}{y_2 - y_1} f(x, y_1) + \frac{y - y_1}{y_2 - y_1} f(x, y_2). \tag{B.37}$$

Putting the values of $f(x, y_1)$ and $f(x, y_2)$ from (B.35) and (B.36) in the equation above gives us

$$\begin{aligned} f(x, y) \approx & \frac{1}{(x_2 - x_1)(y_2 - y_1)} (f(x_1, y_1)(x_2 - x)(y_2 - y) - f(x_2, y_1)(x_1 - x)(y_2 - y) \\ & - f(x_1, y_2)(x_2 - x)(y_1 - y) + f(x_2, y_2)(x_1 - x)(y_1 - y)). \end{aligned} \tag{B.38}$$

We can express the above equation in a more compact form

$$f(x, y) = \frac{1}{(x_2 - x_1)(y_2 - y_1)} V^T(x) M(f) V(y) \tag{B.39}$$

where

$$V(x) = \begin{bmatrix} x_2 - x \\ x - x_1 \end{bmatrix} \tag{B.40}$$

and

$$M(f) = \begin{bmatrix} f(x_1, y_1) & f(x_1, y_2) \\ f(x_2, y_1) & f(x_2, y_2) \end{bmatrix}. \tag{B.41}$$

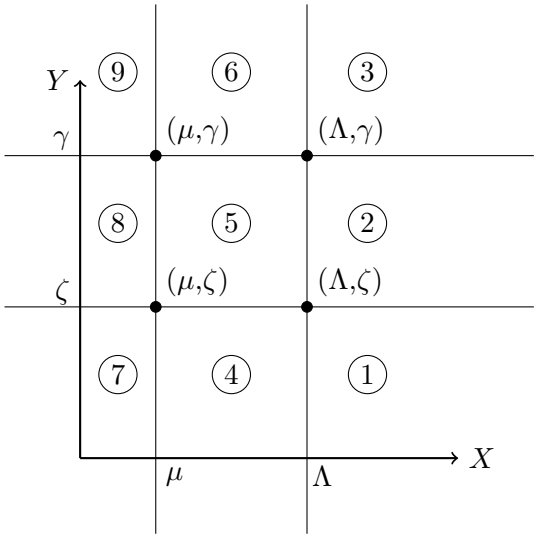

Figure B.2.: Regions defined by the cutoffs on a 2D grid.

Bilinear interpolation is continuous, but not smooth across mesh boundaries. There are improved formulas such as *bicubic* interpolation, which ensure a smooth derivative of the interpolant. These methods are, however, at least an order of magnitude slower than the bilinear case, so that we mainly stick to the latter method.

B.5.2. Application of the Interpolation and Extrapolation in 2D

After defining 2D interpolation methods in the last section, now we can introduce their application in our approach. We should pay attention that here the 2D interpolation is defined on a 2D grid. As it is mentioned before, in this case we deal with 9 regions for which we need interpolation only for the internal region where x and y are on the range. However, for the remaining 8 regions we should consider extrapolation. As it can be seen in the figure B.2, we define the regions according to the cutoffs μ, Λ for the X axis and ζ, γ for the axis in the Y direction. Therefore, for a given coordinate like (x, y), in an algorithm we should first just find out in which region the coordinates define the function value. In order to make the problem simpler we labeled the regions by numbers, where as it can be seen in figure B.2 only for the 5th region we do interpolation and the rest are the regions in which the function must be extrapolated.

For 8 extrapolation regions we start from the IR region where we had only the simple constant extrapolation in the 1D grid case. In the 2D case for a region like region 7 we also expect the function to be a constant, thus for the IR extrapolation in this region we consider $f(\mu, \zeta)$. Moreover, for the region 4 we can consider the interpolated value $f(\mu, y)$. In the same manner, for region 8 which is symmetric to region 4 we consider $f(x, \zeta)$ where $f(x, y)$ denotes the interpolated function. The remaining regions (1, 2, 3, 6, 9) all require extrapolations. In these cases, we fit the nodes out of the interpolation region in a 2D power-law function where we basically use equation (B.4) but for a 2D grid. This means that depending on if the extrapolation region is out of the grid vertically or horizontally, we recall equation (B.5) in which the points x_1 and x_0 give their places to the distances from the origin of the coordinates or the lines r_1 and r_0 on the 2D mesh and functions $f(x_0)$ and $f(x_1)$ were exchanged by $f(x_0, x_0')$ and $f(x_1, x_1')$.

B.5.3. Integral Equations in Ratio Form

One of the points which is mentioned in chapter 2 is to consider the integral equation (B.28) in ratio form by factorizing the function which depends only on the external momentum or

$$f(x) = \frac{\int_{\mu}^{\Lambda}\int_{\gamma}^{\nu} d(y,z)\mathcal{I}(x,y,z,f(x),f(y))}{1+\int_{\mu}^{\Lambda}\int_{\gamma}^{\nu} d(y,z)\mathcal{Q}(x,y,z,f(x),f(y))} \tag{B.42}$$

as it has been done in [100]. Although rewriting equation (B.28) as in the above form has an advantage of greater stability so that we can employ larger values for the relaxation parameter δ, writing the equation in this form can only be used for the uncoupled equations (i.e. Adler-Davis equation) where we can solve the equation in ratio form. However, in the case of solving equation (2.156) we cannot use the ratio form for the obvious reason which is explained in chapter 2.

C. Coherent Fermion States

For a second quantized fermionic system described by the annihilation and creation operators $a_n^\dagger$, a_n we have the relations

$$\{a_n, a_m\} = \{a_n^\dagger, a_m^\dagger\} = 0 \tag{C.1}$$

and

$$\{a_n, a_m^\dagger\} = \delta_{mn} \tag{C.2}$$

where the indices m, n refer to the single particle state $|\phi_m\rangle$ or $|\phi_n\rangle$. Likewise, by considering $|0\rangle$ as Fock vacuum, we have

$$a_m |0\rangle = 0. \tag{C.3}$$

The coherent fermionic states $|\xi\rangle$ are defined as the eigenstates of the annihilation operators

$$a_m |\xi\rangle = \xi_m |\xi\rangle \tag{C.4}$$

where ξ is a *Grassmann* variable. Furthermore, we have

$$\langle\xi| a_m^\dagger = \langle\xi| \xi_m^*. \tag{C.5}$$

Expanding the coherent states in the equations (C.4) and (C.5), in Fock space we have

$$|\xi\rangle = \exp\Big\{ \sum\!\!\!\!\!\!\int_m \xi_m a_m^\dagger \Big\} |0\rangle \quad , \quad \langle\xi| = \exp\Big\{ \sum\!\!\!\!\!\!\int_m \xi_m^* a_m \Big\} \langle 0| \tag{C.6}$$

where we can see the scalar product of two coherent states has the form

$$\langle\phi|\psi\rangle = \exp\Big\{ \sum\!\!\!\!\!\!\int_m \phi_m^* \psi_m \Big\}. \tag{C.7}$$

Furthermore for the unit operator, we have

$$\int \prod_m d\xi_m^* d\xi_m \exp\Big\{ \sum\!\!\!\!\!\!\int_m \phi_m^* \psi_m \Big\} |\xi\rangle \langle\xi| = \mathbb{1}. \tag{C.8}$$

Let us consider an arbitrary state like $|\eta\rangle$ in Fock space which we can express the state in the basis of coherent fermion states $|\xi\rangle$ by taking the scalar product

$$\eta(\xi^*) = \langle\xi|\eta\rangle \tag{C.9}$$

from (C.6) we can Taylor expand our functionals as

$$\eta(\xi^*) = \sum_n \sum_{k_n} \eta_{k_1,..,k_n} \xi_{k_1}^* ... \xi_{k_n}^* \tag{C.10}$$

where $\eta_{k_1,..,k_n}$ are complex numbers. Moreover, for the bra vectors we simply use the involution formula

$$(\xi_i \xi_j)^* = \xi_j^* \xi_i^* = -\xi_i^* \xi_j^* \tag{C.11}$$

resulting

$$\langle \eta | \xi \rangle = \left(\eta(\xi^*) \right)^* \tag{C.12}$$

therefore we have

$$\left(\eta(\xi^*) \right)^* = \eta^*(\xi) = \sum_n \sum_{k_n} \eta^*_{k_1,..,k_n} \xi_{k_1} ... \xi_{k_n}. \tag{C.13}$$

Defining the Fock space states by the action of the function of the creation operator $f(a^\dagger)$ on the vacuum state, we have in the coherent state representation the form, $\eta(\xi^*) = f(\xi^*)$. Furthermore, the scalar product between two Fock states can be demonstrated by means of the completeness relation (C.8)

$$\langle \eta | \chi \rangle = \int d\xi^* d\xi e^{-\xi^* \xi} \eta^* \xi \chi(\xi^*). \tag{C.14}$$

Additionally, using equation (C.5) we can define the action of the operator on a Fock state in the coherent state basis as

$$\langle \xi | \hat{O}(a, a^\dagger) | \eta \rangle = \hat{O}(\frac{\partial}{\partial \xi^*}, \xi^*) \eta(\xi^*) \tag{C.15}$$

from which the matrix elements in the Fock space take the form

$$\langle \eta | \hat{O}(a, a^\dagger) | \chi \rangle = \int d\xi^* d\xi e^{-\xi^* \xi} \eta^*(\xi) \hat{O}(\frac{\partial}{\partial \xi^*}, \xi^*) \chi(\xi^*). \tag{C.16}$$

D. Bibliography

[1] Serguei Chatrchyan et al. Observation of a new boson at a mass of 125 GeV with the CMS experiment at the LHC. *Phys. Lett.*, B716:30–61, 2012.

[2] Georges Aad et al. Observation of a new particle in the search for the Standard Model Higgs boson with the ATLAS detector at the LHC. *Phys. Lett.*, B716:1–29, 2012.

[3] Peter W. Higgs. Broken Symmetries and the Masses of Gauge Bosons. *Phys. Rev. Lett.*, 13:508–509, 1964.

[4] F. Englert and R. Brout. Broken Symmetry and the Mass of Gauge Vector Mesons. *Phys. Rev. Lett.*, 13:321–323, 1964.

[5] Makoto Kobayashi and Toshihide Maskawa. CP Violation in the Renormalizable Theory of Weak Interaction. *Prog. Theor. Phys.*, 49:652–657, 1973.

[6] Y. Fukuda et al. Evidence for oscillation of atmospheric neutrinos. *Phys. Rev. Lett.*, 81:1562–1567, 1998.

[7] Q. R. Ahmad et al. Measurement of the rate of $\nu_e + d \rightarrow p + p + e^-$ interactions produced by ^8B solar neutrinos at the Sudbury Neutrino Observatory. *Phys. Rev. Lett.*, 87:071301, 2001.

[8] P. J. E. Peebles and Bharat Ratra. The Cosmological constant and dark energy. *Rev. Mod. Phys.*, 75:559–606, 2003.

[9] S. Adam, E. H. Hwang, V. M. Galitski, and S. Das Sarma. A self-consistent theory for graphene transport. *Proceedings of the National Academy of Sciences*, 104(47):18392–18397, Nov 2007.

[10] John R. Ellis. Beyond the standard model with the LHC. *Nature*, 448:297–301, 2007.

[11] Dmitri Kazakov. *Particle Physics Beyond the Standard Model: Lecture Notes of the Les Houches Summer School 2005*. Elsevier Science, 2006.

[12] Simon Peter Rosen (ed.) (Purdue U.) D.B. Lichtenberg (ed.) (Indiana U.). *Developments In The Quark Theory Of Hadrons. Vol. 1. 1964 - 1978*. Notantum:Hadronic Press, 1980.

[13] Murray Gell-Mann. A Schematic Model of Baryons and Mesons. *Phys. Lett.*, 8:214–215, 1964.

[14] G. Zweig. An SU(3) model for strong interaction symmetry and its breaking. Version 2. In D.B. Lichtenberg and Simon Peter Rosen, editors, *Developments In The Quark Theory Of Hadrons. Vol. 1. 1964 - 1978*, pages 22–101. 1964.

[15] David Griffiths. *Introduction to Elementary Particles*. Wiley VCH Verlag GmbH, 2008.

[16] M. Jacob and P. V. Landshoff. Large Transverse Momentum and Jet Studies. *Phys. Rept.*, 48:285, 1978.

[17] Martin Breidenbach, Jerome I. Friedman, Henry W. Kendall, Elliott D. Bloom, D. H. Coward, H. C. DeStaebler, J. Drees, Luke W. Mo, and Richard E. Taylor. Observed Behavior of Highly Inelastic electron-Proton Scattering. *Phys. Rev. Lett.*, 23:935–939, 1969.

[18] Elliott D. Bloom et al. High-Energy Inelastic e p Scattering at 6-Degrees and 10-Degrees. *Phys. Rev. Lett.*, 23:930–934, 1969.

[19] E. Rutherford . The scattering of alpha and beta rays by matter and the structure of the atom. *Phil. Mag.*, 6:21, 1911.

[20] Guido Altarelli and James Wells. Gauge theories and the standard model. In *Collider Physics within the Standard Model*. Springer, Jan 2017.

[21] Michio Kaku. *Quantum Field Theory: A Modern Introduction*. Oxford University Press; 1 edition., (March 11, 1993).

[22] Glashow, S. The renormalizability of vector meson interactions. *Nucl. Phys.*, 10:107, (1959).

[23] Salam, A.; Ward, J. C. (1959). "Weak and electromagnetic interactions". Nuovo Cimento. 11 (4): 568–577.

[24] Weinberg, S. A model of leptons. *Phys. Rev. Lett.*, 19:1264, 1967.

[25] Chen-Ning Yang and Robert L. Mills. Conservation of Isotopic Spin and Isotopic Gauge Invariance. *Phys. Rev.*, 96:191–195, 1954.

[26] David J. Gross and Frank Wilczek. Ultraviolet behavior of non-abelian gauge theories. *Physical Review Letters*, 30(26):1343–1346, Jun 1973.

[27] H. David Politzer. Reliable perturbative results for strong interactions? *Physical Review Letters*, 30(26):1346–1349, Jun 1973.

[28] Stefan Olejník Jeff Paul Greensite. *Confinement, Topology, and Other Non-Perturbative Aspects of QCD*. Springer, 2002.

[29] Julia Danzer, Christof Gattringer, Ludovit Liptak, and Marina Marinkovic. A Study of the sign problem for lattice QCD with chemical potential. *Phys. Lett.*, B682:240–245, 2009.

[30] Nicolas Garron and Kurt Langfeld. Anatomy of the sign-problem in heavy-dense qcd. *The European Physical Journal*, C76(10):1, Oct 2016.

[31] T. D. Kieu and C. J. Griffin. Monte Carlo simulations with indefinite and complex valued measures. *Phys. Rev.*, E49:3855–3859, 1994.

[32] Davide R. Campagnari, Ehsan Ebadati, Hugo Reinhardt, and Peter Vastag. Revised variational approach to QCD in Coulomb gauge. *Phys. Rev.*, D94(7):074027, 2016.

[33] C. Feuchter and H. Reinhardt. Variational solution of the Yang-Mills Schrodinger equation in Coulomb gauge. *Phys. Rev.*, D70:105021, 2004.

[34] Philippe de Forcrand and Massimo D'Elia. On the relevance of center vortices to QCD. *Phys. Rev. Lett.*, 82:4582–4585, 1999.

[35] Peter Watson and Hugo Reinhardt. Propagator Dyson-Schwinger Equations of Coulomb Gauge Yang-Mills Theory Within the First Order Formalism. *Phys. Rev.*, D75:045021, 2007.

[36] Peter Watson and Hugo Reinhardt. Two-point functions of Coulomb gauge Yang-Mills theory. *Phys. Rev.*, D77:025030, 2008.

[37] C. Popovici, P. Watson, and H. Reinhardt. Quarks in Coulomb gauge perturbation theory. *Phys. Rev.*, D79:045006, 2009.

[38] Hugo Reinhardt and Peter Watson. Resolving temporal Gribov copies in Coulomb gauge Yang-Mills theory. *Phys. Rev.*, D79:045013, 2009.

[39] Peter Watson and Hugo Reinhardt. The Coulomb gauge ghost Dyson-Schwinger equation. *Phys. Rev.*, D82:125010, 2010.

[40] Davide R. Campagnari and Hugo Reinhardt. Non-Gaussian wave functionals in Coulomb gauge Yang–Mills theory. *Phys. Rev.*, D82:105021, 2010.

[41] Craig D. Roberts and Anthony G. Williams. Dyson-Schwinger equations and their application to hadronic physics. *Prog. Part. Nucl. Phys.*, 33:477–575, 1994.

[42] Christian S. Fischer. Infrared properties of QCD from Dyson-Schwinger equations. *J. Phys.*, G32:R253–R291, 2006.

[43] Reinhard Alkofer, Steven Ahlig, and Lorenz von Smekal. The Infrared behavior of propagators in Landau gauge QCD. pages 196–201, 1999.

[44] Davide R. Campagnari, Hugo Reinhardt, Markus Q. Huber, Peter Vastag, and Ehsan Ebadati. Dyson–Schwinger Approach to Hamiltonian QCD. *EPJ Web Conf.*, 137:03004, 2017.

[45] Davide R. Campagnari and Hugo Reinhardt. Dyson–Schwinger approach to Hamiltonian Quantum Chromodynamics. *Phys. Rev.*, D92(6):065021, 2015.

[46] H. Reinhardt, G. Burgio, D. Campagnari, E. Ebadati, J. Heffner, M. Quandt, P. Vastag, and H. Vogt. Hamiltonian approach to QCD in Coulomb gauge at zero and finite temperature. *EPJ Web Conf.*, 137:03019, 2017.

[47] Hugo Reinhardt. Unpublished lectures.

[48] O. Klein, in New Theories in Physics, Conference organised in collaboration with the International Union of Physics and the Polish Intellectual Cooperation Committee, Warsaw, May 30th - June 3rd, 1938.

[49] G. 't Hooft. Gauge theory and renormalization (Erice, August 1994). 2008.

[50] Hugo Reinhardt. Notes on the Yang–Mills vacuum wave functioal.

[51] L. D. Faddeev and V. N. Popov. Feynman Diagrams for the Yang-Mills Field. *Phys. Lett.*, 25B:29–30, 1967.

[52] J. Rgen Fuchs Jurgen Fuchs, Christoph Schweigert. *Symmetries, Lie Algebras and Representations*. Cambridge University Press, 2003.

[53] Feynman R.P. The quantum theory of gravitation. *Acta Physica Polonica*, 24, 1963.

[54] N. H. Christ and T. D. Lee. Operator Ordering and Feynman Rules in Gauge Theories. *Phys. Rev.*, D22:939, 1980. [Phys. Scripta23,970(1981)].

[55] D. Epple, H. Reinhardt, and W. Schleifenbaum. Confining Solution of the Dyson-Schwinger Equations in Coulomb Gauge. *Phys. Rev.*, D75:045011, 2007.

[56] H. Reinhardt, G. Burgio, D. Campagnari, E. Ebadati, J. Heffner, M. Quandt, P. Vastag, and H. Vogt. Hamiltonian approach to qcd in coulomb gauge - a survey of recent results. *Advances in High Energy Physics*, 2018(2312498), Jun 2018.

[57] V. N. Gribov. Quantization of Nonabelian Gauge Theories. *Nucl. Phys.*, B139:1, 1978.

[58] H. Reinhardt. Dielectric function of the QCD vacuum. *Physical Review Letters*, 101(6), Aug 2008.

[59] D. Zwanziger. Renormalization in the Coulomb gauge and order parameter for confinement in QCD. *Nucl. Phys.*, B518:237–272, 1998.

[60] Jeff Greensite, Stefan Olejnik, and Daniel Zwanziger. Confinement and center vortices in Coulomb gauge: Analytic and numerical results. *Nucl. Phys. Proc. Suppl.*, 141:170–176, 2005. [,170(2004)].

[61] Daniel Zwanziger. No confinement without coulomb confinement. *Phys. Rev. Lett.*, 90:102001, Mar 2003.

[62] Kenneth G. Wilson. Confinement of Quarks. *Phys. Rev.*, D10:2445–2459, 1974. [,45(1974)].

[63] M. Pak and H. Reinhardt. The Wilson loop from a Dyson equation. *Phys. Rev.*, D80:125022, 2009.

[64] Jeff Greensite and Adam P. Szczepaniak. *Phys. Rev.*, D91:034503, Feb 2015.

[65] Giuseppe Burgio, Markus Quandt, Hugo Reinhardt, and Hannes Vogt. Coulomb versus physical string tension on the lattice. *Phys. Rev.*, D92:034518, Aug 2015.

[66] Giuseppe Burgio, Markus Quandt, Hugo Reinhardt, and Hannes Vogt. Gribov horizon and gribov copies effect in lattice coulomb gauge. *Phys. Rev.*, D95:014503, Jan 2017.

[67] Hugo Reinhardt, Markus Quandt, and Giuseppe Burgio. On the temporal Wilson loop in the Hamiltonian approach in Coulomb gauge. *Phys. Rev.*, D85:025001, 2012.

[68] Hugo Reinhardt. Hamiltonian finite-temperature quantum field theory from its vacuum on partially compactified space. *Phys. Rev.*, D94(4):045016, 2016.

[69] Hugo Reinhardt. On 't Hooft's loop operator. *Physics Letters*, B557(3-2):317–323, 2003.

[70] H. Reinhardt and D. Epple. The 't Hooft loop in the Hamiltonian approach to Yang-Mills theory in Coulomb gauge. *Phys. Rev.*, D76:065015, 2007.

[71] Jeffrey Goldstone, Abdus Salam, and Steven Weinberg. Broken Symmetries. *Phys. Rev.*, 127:965–970, 1962.

[72] J. Goldstone. Field theories with superconductor solutions. *Il Nuovo Cimento (1955-1965)*, 19(1):154, Jan 1961.

[73] Yoichiro Nambu. Quasiparticles and Gauge Invariance in the Theory of Superconductivity. *Phys. Rev.*, 117:648–663, 1960.

[74] H. Reinhardt and C. Feuchter. Yang-mills wave functional in coulomb gauge. *Phys. Rev.*, D71(105002), 2005.

[75] Davide R. Campagnari and Hugo Reinhardt. Hamiltonian Approach to QCD in Coulomb Gauge: Perturbative Treatment of the Quark Sector. *Int. J. Mod. Phys.*, A30(17):1550100, 2015.

[76] P. Vastag, H. Reinhardt, and D. Campagnari. Improved variational approach to QCD in Coulomb gauge. *Phys. Rev.*, D93(6):065003, 2016.

[77] Lawrence M. Krauss. *Quantum Man.* WW Norton & Co, 2012.

[78] Alfonso Sorrentino. *Action-minimizing Methods in Hamiltonian Dynamics (MN-50): An Introduction to Aubry-Mather Theory.* Princeton University Press, 2015.

[79] Walter Ritz . Über eine neue Methode zur Lösung gewisser Variationsprobleme der mathematischen Physik. *Journal für die Reine und Angewandte Mathematik*, 135:1–61, 1909.

[80] D. Schutte. Nonperturbative many-body techniques applied to a Yang-Mills field theory. *Phys. Rev.*, D31:810–821, 1985.

[81] Jonathan R. Finger and Jeffrey E. Mandula. Quark pair condensation and chiral symmetry breaking in QCD. *Nuclear Physics*, B199(1):168–188, May 1982.

[82] C. Feuchter and H. Reinhardt. Quark and gluon confinement in Coulomb gauge. 2004.

[83] Daniel Zwanziger. Fundamental modular region, Boltzmann factor and area law in lattice gauge theory. *Nucl. Phys.*, B412:657–730, 1994.

[84] Davide R. Campagnari, Hugo Reinhardt, and Axel Weber. Perturbation theory in the Hamiltonian approach to Yang-Mills theory in Coulomb gauge. *Phys. Rev.*, D80:025005, 2009.

[85] G. Burgio, M. Quandt, and H. Reinhardt. Coulomb gauge gluon propagator and the Gribov formula. *Phys. Rev. Lett.*, 102:032002, 2009.

[86] D. Zwanziger. Local and Renormalizable Action From the Gribov Horizon. *Nucl. Phys.*, B323:513–544, 1989.

[87] Daniel Zwanziger. Lattice Coulomb Hamiltonian and static color Coulomb field. *Nucl. Phys.*, B485:185–240, 1997.

[88] A.A.Abrikosov. The magnetic properties of superconducting alloys. *Journal of Physics and Chemistry of Solids*, 2(3):199–208, 1957.

[89] Leon N. Cooper. Bound electron pairs in a degenerate Fermi gas. *Phys. Rev.*, 104:1189–1190, 1956.

[90] Markus Pak. *The Quark Sector of the QCD Ground State in Coulomb Gauge*. PhD thesis, Physik/Uni Tuebingen, 2012.

[91] A. Le Yaouanc, L. Oliver, O. Pene, and J. C. Raynal. Spontaneous Breaking of Chiral Symmetry for Confining Potentials. *Phys. Rev.*, D29:1233–1257, 1984.

[92] Stephen L. Adler and A. C. Davis. Chiral Symmetry Breaking in Coulomb Gauge QCD. *Nucl. Phys.*, B244:469, 1984.

[93] J. C. Slater. The Theory of Complex Spectra. *Phys. Rev.*, 34:1293–1322, 1929.

[94] G. C. Wick. The Evaluation of the Collision Matrix. *Phys. Rev.*, 80:268–272, 1950. [,592(1950)].

[95] Personal talks with Dr. Davide Campagnari.

[96] Yorikiyo Nagashima. *Elementary Particle Physics 1.* Wiley VCH Verlag GmbH, 2010.

[97] P. Bozek. Dressed vertices. *Phys. Lett.*, B579:309–315, 2004.

[98] Francesco Iachello. *Lie Algebras and Applications*. Springer Berlin Heidelberg, 2007.

[99] R. Alkofer and P.A. Amundsen. Chiral symmetry breaking in an instantaneous approximation to coulomb gauge QCD. *Nuclear Physics*, B306(2):305–342, aug 1988.

[100] Peter Watson and Hugo Reinhardt. Leading order infrared quantum chromodynamics in Coulomb gauge. *Phys. Rev.*, D85:025014, 2012.

[101] Giuseppe Burgio, Markus Quandt, Hugo Reinhardt, and Hannes Vogt. Coulomb versus physical string tension on the lattice. *Phys. Rev.*, D92(3):034518, 2015.

[102] M. Pak and H. Reinhardt. Chiral Symmetry Breaking in Hamiltonian QCD in Coulomb Gauge. *Phys. Lett.*, B707:566–569, 2012.

[103] Reinhard Alkofer, M. Kloker, A. Krassnigg, and R. F. Wagenbrunn. Aspects of the confinement mechanism in Coulomb-gauge QCD. *Phys. Rev. Lett.*, 96:022001, 2006.

[104] Hugo Reinhardt. *Quantenmechanik 2: Pfadintegralformulierung und Operatorformalismus*. Oldenbourg Wissenschaftsverlag, 2013.

[105] M. Pak and H. Reinhardt. Quark Sector of the QCD Groundstate in Coulomb Gauge. *Phys. Rev.*, D88:125021, 2013.

[106] R. Williams, C. S. Fischer, and M. R. Pennington. Anti-q q condensate for light quarks beyond the chiral limit. *Phys. Lett.*, B645:167–172, 2007.

[107] D.A. Kirznits and A.D. Linde. *Phys. Lett.*, B42:471, 1972.

[108] D.A. Kirzhnits and A.D. Linde. *Ann. Phys.*, 101:195, 1976.

[109] C. W. Bernard. *Phys. Rev*, D9:3312, 1974.

[110] Steven Weinberg. Gauge and global symmetries at high temperature. *Phys. Rev.*, D9:3357–3378, Jun 1974.

[111] L. Dolan and R. Jackiw. Symmetry behavior at finite temperature. *Phys. Rev.*, D9:3320–3341, Jun 1974.

[112] J. Zinn-Justin. Quantum field theory at finite temperature: An introduction. 2007.

[113] Frithjof Karsch. Lattice qcd at high temperature and density. *Lect.Notes Phys.*, 583:209–249, 2002.

[114] Christof Gattringer, Thomas Kloiber, and Michael Müller-Preussker. Dual simulation of the two-dimensional lattice U(1) gauge-Higgs model with a topological term. *Phys. Rev.*, D92(11):114508, 2015.

[115] Michel Le Bellac. *Thermal Field Theory*. Cambridge University Press, 2000.

[116] Charles Gale Joseph I. Kapusta. *Finite-Temperature Field Theory: Principles and Applications*. Cambridge University Press, 2011.

[117] Jan M. Pawlowski. Equation of state and phase diagram of strongly interacting matter. *Nucl. Phys.*, A931:113–124, 2014.

[118] Jan Heffner, Hugo Reinhardt, and Davide R. Campagnari. The deconfinement phase transition in the Hamiltonian approach to Yang–Mills theory in Coulomb gauge. *Phys. Rev.*, D85:125029, 2012.

[119] Hugo Reinhardt and Jan Heffner. Effective potential of the confinement order parameter in the Hamiltonian approach. *Phys. Rev.*, D88:045024, 2013.

[120] J. Heffner and H. Reinhardt. Finite-temperature Yang-Mills theory in the Hamiltonian approach in Coulomb gauge from a compactified spatial dimension. *Phys. Rev.*, D91(8):085022, 2015.

[121] Takeo Matsubara. A New approach to quantum statistical mechanics. *Prog. Theor. Phys.*, 14:351–378, 1955.

[122] Markus Quandt, Ehsan Ebadati, Hugo Reinhardt and Peter Vastag. Chiral symmetry restoration at finite temperature within the Hamiltonian approach to QCD in Coulomb gauge. *Submitted to Physical Review*, D, April 2018.

[123] T. Ablyazimov et al. Challenges in QCD matter physics –The scientific programme of the Compressed Baryonic Matter experiment at FAIR. *Eur. Phys. J.*, A53(3):60, 2017.

[124] Ryogo Kubo. Statistical mechanical theory of irreversible processes. 1. General theory and simple applications in magnetic and conduction problems. *J. Phys. Soc. Jap.*, 12:570–586, 1957.

[125] Paul C. Martin and Julian Schwinger . Theory of many-particle systems.i. *Phys. Rev.*, 115:1342, 1959.

[126] Y.Yang. An Introduction to Thermal Field Theory. Master's thesis, Imperial College London , 2011.

[127] Andreas Wipf. www.tpi.uni-jena/qfphysics/homepage/wipf/lectures/pfad/pfad6.pdf.

[128] John Cardy . www-thphys.physics.ox.ac.uk/people/JohnCardy/qft/qftcomplete.pdf.

[129] Piessens, R., Doncker-Kapenga, E. de, Überhuber, C.W., Kahaner, D.K. . *Quadpack A Subroutine Package for Automatic Integration.* Springer, 1983.

[130] Takuya Ooura, Masatake Mori. A robust double exponential formula for Fourier-type integrals. *Journal of Computational and Applied Mathematic*, 112:229–241, 1999.

[131] P.R.Graves-Morris, D.E.Roberts, A.Salam. The epsilon algorithm and related topics. *Journal of Computational and Applied Mathematics* , 122:51–80, 2000.

[132] Pok Man Lo and Eric S. Swanson. Confinement Models at Finite Temperature and Density. *Phys. Rev.*, D81:034030, 2010.

[133] Szabolcs Borsanyi, Zoltan Fodor, Christian Hoelbling, Sandor D Katz, Stefan Krieg, Claudia Ratti, and Kalman K. Szabo. Is there still any tc mystery in lattice qcd? results with physical masses in the continuum limit iii. *JHEP*, 1009:073,2010, May 2010.

[134] A. H. Castro Neto, F. Guinea, N. M. R. Peres, K. S. Novoselov, and A. K. Geim. The electronic properties of graphene. *Rev. Mod. Phys.*, 81:109–162, 2009.

[135] Gordon W Semenoff. Chiral symmetry breaking in graphene. *Physica Scripta*, T146:014016, Jan 2012.

[136] P. R. Wallace. The Band Theory of Graphite . *Phys. Rev.*, 71, 1 May 1947.

[137] S. V. Morozov, K. S. Novoselov, M. I. Katsnelson, F. Schedin, D. C. Elias, J. A. Jaszczak, and A. K. Geim. Giant intrinsic carrier mobilities in graphene and its bilayer. *Phys. Rev. Lett.*, 100:016602, Jan 2008.

[138] Faugeras, Clement; Faugeras, Blaise; Orlita, Milan; Potemski, M.; Nair, Rahul R.; Geim, A. K. Thermal Conductivity of Graphene in Corbino Membrane Geometry. *ACS Nano.*, 4 (4):1889–1892, 2010.

[139] A. K. Geim and K. S. Novoselov. The rise of graphene. *Nature Materials*, 6(3):183–191, Mar 2007.

[140] A. B. Kuzmenko, E. van Heumen, F. Carbone, and D. van der Marel. Universal Optical Conductance of Graphite. *Phys. Rev. Lett.*, 100:117401, 20 March 2008.

[141] Shou-En Zhu, Shengjun Yuan and G. C. A. M. Janssen . Optical transmittance of multilayer graphene. *EPL (Europhysics Letters)* , 108(1), September 2014.

[142] R. R. Nair, P. Blake, A. N. Grigorenko, K. S. Novoselov, T. J. Booth, T. Stauber, N. M. R. Peres, A. K. Geim. Fine Structure Constant Defines Visual Transparency of Graphene. *Science*, 320(5881):1308, Jun 2008.

[143] K. S. Novoselov, Z. Jiang, Y. Zhang, S. V. Morozov, H. L. Stormer, U. Zeitler, J. C. Maan, G. S. Boebinger, P. Kim, and A. K. Geim. Room-temperature quantum hall effect in graphene. *Science*, 315(5817):1379–1379, Mar 2007.

[144] Tomasz M. Rusin and Wlodek Zawadzki. Zitterbewegung of electrons in graphene in a magnetic field. *Phys. Rev.*, B78:125419, Sep 2008.

[145] M. I. Katsnelson, K. S. Novoselov & A. K. Geim. Chiral tunnelling and the Klein paradox in graphene. *Nature Physics* , 2:620, 2006.

[146] H. W. Kroto, J. R. Heath, S. C. O'Brien, R. F. Curl & R. E. Smalley. C60: Buckminsterfullerene. *Nature* , 318:162–163, (14 November 1985).

[147] Sumio Iijima. Helical microtubules of graphitic carbon. *Nature* , 354:56–58, Nov 1991.

[148] Artem R. Oganov, Russell J. Hemley, Robert M. Hazen, Adrian P. Jones. Structure, Bonding, and Mineralogy of Carbon at Extreme Conditions. *Reviews in Mineralogy and Geochemistry*, 75 (1):47–77, 2013.

[149] Peierls, R. E. . Quelques proprietes typiques des corpses solides. *Ann. I. H. Poincare*, 5:177–222, 1935.

[150] Landau, L. D. Zur theorie der phasenumwandlungen ii. *Phys. Z. Sowjetunion*, 11:26, 1937.

[151] S. Reich, J. Maultzsch, C. Thomsen, and P. Ordejón. Tight-binding description of graphene. *Phys. Rev.*, B66:035412, Jul 2002.

[152] Gordon W. Semenoff. Condensed Matter Simulation of a Three-dimensional Anomaly. *Phys. Rev. Lett.*, 53:2449, 1984.

[153] Stephen J. Jenkins . *Chirality at Solid Surfaces* . Wiley, 2018.

[154] Valeri N. Kotov, Bruno Uchoa, Vitor M. Pereira, A. H. Castro Neto, and F. Guinea. Electron-Electron Interactions in Graphene: Current Status and Perspectives. *Rev. Mod. Phys.*, 84:1067, 2012.

[155] Gordon Baym and Siu A. Chin. Landau theory of relativistic fermi liquids. *Nuclear Physics*, A262(3):527–538, May 1976.

[156] Mark Peplow. Graphene: The quest for supercarbon. *Springer Nature*, 503:327–329, Nov 21, 2013.

[157] S. Y. Zhou, G.-H. Gweon, A. V. Fedorov, P. N. First, W. A. de Heer, D.-H. Lee, F. Guinea, A. H. Castro Neto & A. Lanzara. Substrate-induced bandgap opening in epitaxial graphene. *Nature Materials volume*, 6:770–775, 2007.

[158] S Hernández-Ortíz and A Raya. Dynamical masses and confinement in graphene. *Journal of Physics: Conference Series*, 468:012010, Nov 2013.

[159] Marco Herbst. Dynamische symmetriebrechung in graphen. Master's thesis, Institut für Theoretische Physik -Eberhard Karls Universität Tübingen, 2014.

[160] Lei Chang and Yu-Xin Liu. Remark on the consistency of the ladder approximation and the rainbow approximation of Dyson-Schwinger equations of QCD. *Int. J. Mod. Phys.*, A23:1711–1717, 2008.

[161] S. Hernández-Ortíz and A. Raya. Dynamical Masses and Confinement in Graphene. *J. Phys. Conf. Ser.*, 468:012010, 2013.

[162] Bostwick A, Speck F, Seyller T, Horn K, Polini M, Asgari R, MacDonald AH, Rotenberg E. Observation of plasmarons in quasi-freestanding doped graphene. *Science.*, 328(5981):999–1002, 2010.

[163] Oskar Vafek and Matthew J. Case. Renormalization group approach to two-dimensional Coulomb interacting Dirac fermions with random gauge potential. *Phys. Rev.*, B77:033410, Jan 2008.

[164] O. V. Gamayun, E. V. Gorbar, and V. P. Gusynin . Gap generation and semimetal-insulator phase transition in graphene. *Phys. Rev.*, B81:,075429, 2010.

[165] Khveshchenko, D. V. Massive Dirac fermions in single-layer graphene. *Journal of Physics: Condensed Matter*, 21(7), 2009.

[166] O. V. Pavlovsky M. I. Polikarpov P. V. Buividovich, E. V. Luschevskaya and M. V. Ulybyshev. Numerical study of the conductivity of graphene monolayer within the effective field theory approach. *Phys. Rev.*, B86:045107, 2012.

[167] William T. Vetterling Brian P. Flannery William H. Press, Saul A. Teukolsky. *Numerical Recipes in C++: The Art of Scientific Computing Second Edition.* Cambridge University Press, 2007.

[168] 2004. *A History of Mathematics, Brief Version.* Katz, Victor J.

[169] Erik Gregersen. *The Britannica Guide to Analysis and Calculus (Math Explained).* Rosen Education Service , 2010.

[170] L.N.G. Filon. On a quadrature formula for trigonometric integrals. *Proc. Roy Soc. Edinburgh* , 49:38–47, 1928.

[171] E. A. Flinn. A Modification of Filon's Method of Numerical Integration. *Journal of the ACM*, 7(2):181–184, April 1960.

[172] Gene H. Golub and John H. Welsch. Calculation of Gauss quadrature rules. *Math. Comp*, 23:221–230, 1969.

[173] Walter Gautschi. On the construction of Gaussian quadrature rules from modified moments. *Math. Comp.* , 24:245–260, 1970.

[174] Walter Gautschi. Construction of Gauss-Christoffel quadrature formulas. *Math. Comp.*, 22:251–270, 1968.

[175] R. A. Sack and A. F. Donovan. An algorithm for gaussian quadrature given modified moments. *Numerische Mathematik*, 18(5):465, Oct 1971.

[176] Stephen L. Adler and Tsvi Piran. Relaxation methods for gauge field equilibrium equations. *Reviews of Modern Physics*, 56(1):1–40, Jan 1984.

[177] Alexander Aitken. On Bernoulli's numerical solution of algebraic equations. *Proceedings of the Royal Society of Edinburgh* , 46:289–305, 1926.

[178] C.Brezinski. Convergence acceleration during the 20th century. *Journal of Computational and Applied Mathematics* , 122:1–21, October 2000.

[179] Donald G. Anderson. Iterative procedures for nonlinear integral equations. *J. ACM*, 12(4):547–560, October 1965.